UNIVERSITÀ DEGLI STUDI DI UDINE

Dipartimento di Ingegneria Elettrica, Gestionale e Meccanica

Corso di Dottorato in Ingegneria Industriale e dell'Informazione
Ciclo XXIX

Tesi di Dottorato di Ricerca

OPPORTUNISTIC ANGLE OF ARRIVAL ESTIMATION IN IMPAIRED SCENARIOS

Dottorando:
ANDREA PAPAIZ

Relatore:
Prof. ANDREA M. TONELLO

ANNO ACCADEMICO
2016/2017

To <insert your name>,
for your outstanding <insert your quality>.

Ringraziamenti

L'esperienza vissuta in questi tre anni di dottorato è stata molte cose: gratificante, stimolante, divertente ma anche molto difficile e non di rado frustrante. Indipendentemente dalla situazione sono stato sempre e comunque debitamente supportato, sopportato e all'occorrenza insultato dagli efficientissimi e professionalissimi membri del WiPLi Lab, a pochi noto sotto lo pseudonimo di Ledraside Lab. Il WiPLi Lab, gruppo di cui sono stato un orgoglioso *membro*, è un piccolo e ben assortito clan di ingegneri creativi, dotati di pirotecnici cervelli e menti acute e curiose. Di seguito, in ordine di anzianità, qualche parola per ringraziarvi uno per uno. Fabio, inarrivabile esempio di efficienza accademica e pessimo autista, grazie delle preziose riflessioni. Marco, orgoglioso "hardwarista anonimo" con i piedi per terra e la mente tra le giganti rosse, grazie per la *plètora* di fondamentali consulenze e la pazienza. Mauro, profondo conoscitore dei labirinti della notazione matematica e delle segrete tracce tra i *mughi*, grazie per le rigorose risposte alle mie poco rigorose domande. Alberto, appassionato ballerino cesellatore di passi e di articoli scientifici, il *bug-finder* per eccellenza, grazie per l'incessante e asfissiante opera di review.

Inutile dire che la cosa che più mi mancherà di questa esperienza saranno i tanto appassionati quanto improvvisi brainstorming sugli argomenti più disparati, dai famosi "g-con-i" alla meteorologia, dall'astrofisica al concetto di colore.

Grazie e tutti e lunga vita al nostro WiPLi Lab!

Andrea Papaiz

Sesto al Reghena, 14 Marzo 2017

Contents

List of Figures

List of Acronyms

1D	Mono-dimensional
2D	Bi-dimensional
3A-ULA	Three-Axial-ULA
3D-ULA	3D-ULA
3D	Three-dimensional
A-PSK	Amplitude PSK
AoA	Angle of Arrival
AT-CRLB	Average Trajectory CRLB
AT-RMSE	Average Trajectory RMSE
AWGN	Additive White Gaussian Noise
BCID	2D CSP-IDO
BM	Baseline Method
BND	Bivariate Normal Distribution
BS	Base Station
C-AWGN	Circular-Additive White Gaussian Noise (AWGN)
C-CP	Cartesian Complex - pdf
CARATE	Confined Area Random Aerial Trajectory Emulator
CIR	Channel Impulse Response
CRLB	Cramér-Rao Lower Bound

CSP-IDO	Constellation Statistical Pattern Identification and Overlap
D-PoA	Differential-PoA
D-ToA	Differential-ToA
DAC	Digital-to-Analog Converter
DCO	DC Offset
DC	Direct Current
DMM	Drift Motion Model
DoA	Direction of Arrival
DS	Doppler Shift
e.g.	exempli gratia (for the sake of an example)
FA-AoA	Fully Assisted AoA
FPA	Full Parallel Architecture
GL-S	Ground Localization Scenario
GNSS	Global Navigation Satellite System
GPS	Global Positioning System
GSM	Global System for Mobile Communications
i.e.	id est (that is)
IEEE	Institute of Electrical and Electronic Engineers
IQS	I-Q Skew
IQU	I-Q Unbalance
I	In-phase
LOS	Line of Sight
LPF	Low Pass Filter
LTE	Long Term Evolution
MP	Multi-path
MUSIC	MUltiple SIgnal Classification

O-AoA	Opportunistic AoA
OFDM	Orthogonal Frequency Division Multiplexing
P-CP	Polar Complex - pdf
PA-AoA	Partially Assisted AoA
PC-G	Particles Cloud Granularity
PC-W	Particles Cloud Width
pdf	probability density function
PF	Particle Filtering
PL	Path Loss
PN	Phase Noise
PoA	Phase of Arrival
PO	Phase Offset
PPA	Partially Parallel Architecture
PSAS	Particles Swarm Adaptive Scattering
PSK	Phase Shift Keying
QAM	Quadrature Amplitude Modulation
Q	In-quadrature
RFID	Radio Frequency (RF) Identification
RF	Radio Frequency
RMSE	RMS error
RMS	root-mean-square
root-MUSIC	root-MUSIC
RRC	Root Raised Cosine
RSSE	Received Signal Strength Estimation
RSU	Road Side Unit
SARS	Solid Angle RMSE

SDR	Software Defined Radio
SL-S	Self Localization Scenario
SMC	Sequential Monte Carlo
SNR	Signal to Noise Ratio
ToA	Time of Arrival
TSA	Time Switched Architecture
U-SGM	US-CIR based Scattering Geometric Model
UAV	Unmanned Aerial Vehicle
ULA	Uniform Linear Array
UMTS	Universal Mobile Telecommunications System
US-CIR	Uniformly Sampled CIR
USRP	Universal Software Radio Peripheral
UWB	Ultra Wide Band
V2I	Vehicle-to-Infrastructure
V2V	Vehicle-to-Vehicle
V2X	Vehicle-to-Vehicle (V2V) and Vehicle-to-Infrastructure (V2I)
w.r.t.	with respect to
WiPLi Lab	Wireless and Power Line Laboratory
WSN	Wireless Sensor Network
zero-IF	zero intermediate frequency

List of Symbols

Table 1: List of the most commonly used symbols.

Symbol	Unit	Definition
$\{\cdot\}^*$	-	Complex conjugate operator
$\measuredangle$	-	Phase operator
$E[\cdot]$	-	Expected value operator
$[\cdot] \pmod a$	-	Modulo operator with modulus a
$\overline{AB}$	-	Euclidean distance between point A and point B
$\delta(t)$	-	Dirac delta function in the continuous time domain
$\mathcal{U}(a,b)$	-	Uniform random variable between a and b
$\mathcal{N}(\mu,\sigma)$	-	Normal random variable with mean μ and standard deviation σ
$\mathcal{X} \times \mathcal{Y}$	-	Cartesian product between set $\mathcal{X}$ and set $\mathcal{Y}$
$\|\mathcal{Z}\|$	-	Cardinality of set $\mathcal{Z}$ (number of elements)
$\arctan(\alpha)$	-	Inverse function of $\tan a$
$\arcsin(\alpha)$	-	Inverse function of $\sin(a)$
$\mathcal{R}[\cdot]$	-	Real part operator
$\mathcal{I}[\cdot]$	-	Imaginary part operator

Abstract

This work if focused on the analysis and the development of Angle of Arrival (AoA) radio localization methods. The radio positioning system considered is constituted by a radio source and by a receiving array of antennas.

The positioning algorithms treated in this work are designed to have a passive and opportunistic approach. The opportunistic attribute implies that the radio localization algorithms are designed to provide the AoA estimation with nearly-zero information on the transmitted signals. No training sequences or waveforms custom designed for localization are taken into account. The localization is termed passive since there is no collaboration between the transmitter and the receiver during the localization process. Then, the algorithms treated in this work are designed to eavesdrop already existing communication signals and to locate their radio source with nearly-zero knowledge of the signal and without the collaboration of the transmitting node.

First of all, AoA radio localization algorithms can be classified in terms of involved signals (narrowband or broadband), antenna array pattern (L-shaped, circular, etc.), signal structure (sinusoidal, training sequences, etc.), Differential-Time of Arrival (ToA) (D-ToA)/Differential-Phase of Arrival (PoA) (D-PoA) and collaborative/non collaborative.

Than, the most detrimental effects for radio communications are treated: the Multipath (MP) channels and the impaired hardware. A geometric model for the MP is analysed and implemented to test the robustness of the proposed methods. The effects of MP on the received signals statistics from the AoA estimation point-of-view are discussed. The hardware impairments for the most common components are introduced and their effects in the AoA estimation process are analysed.

Two novel algorithms that exploits the AoA from signal snapshots acquired sequentially with a time division approach are presented. The acquired signals are Quadrature Amplitude Modulation (QAM) waveforms eavesdropped from a pre-existing communication. The proposed methods, namely Constellation Statistical Pattern Identification and Overlap (CSP-IDO) and Bi-dimensional (2D) CSP-IDO (BCID), exploit the probability density functions (pdfs) of the received signals to obtain the D-PoAs. Both CSP-IDO and

BCID use the statistical pattern of received signals exploiting the transmitter statistical signature. Since the presence of hardware impairments modify the statistical pattern of the received signals, CSP-IDO and BCID are able to exploit it to improve the performance with respect to (w.r.t.) the ideal case. Since the proposed methods can be used with a switched antenna architecture they are implementable with a reduced hardware contrariwise to synchronous methods like MUltiple SIgnal Classification (MUSIC) that are not applicable.

Then, two iterative AoA estimation algorithms for the dynamic tracking of moving radio sources are implemented. Statistical methods, namely Particle Filtering (PF), are used to implement the iterative tracking of the AoA from D-PoA measures in two different scenarios: automotive and Unmanned Aerial Vehicle (UAV). The AoA tracking of an electric car signalling with a Institute of Electrical and Electronic Engineers (IEEE)802.11p-like standard is implemented using a test-bed and real measures elaborated with a the proposed Particles Swarm Adaptive Scattering (PSAS) algorithm. The tracking of a UAV moving in the Three-dimensional (3D) space is investigated emulating the UAV trajectory using the proposed Confined Area Random Aerial Trajectory Emulator (CARATE) algorithm.

Introduction

1

Radio localization techniques such as Angle of Arrival (AoA) algorithms play an important role in the wider universe of positioning systems, exempli gratia (for the sake of an example) (e.g.), Global Navigation Satellite Systems (GNSSs) [1] applications. The advantage of terrestrial radio localization based methods [2] with respect to (w.r.t.) GNSS is its feasible deployment in environments where satellite visibility is not fully achievable, id est (that is) (i.e.) indoor and canyon like scenarios [3]. Radio localization techiques can be used to implement auto-positioning using known radio anchors or, dually, to remotely locate unknown radio sources [4]. Furthermore, terrestrial radio localization techniques such as AoA do not need the deployment of the extremely expansive and complex satellite constellation infrastructure of GNSS. However, despite the complexity, GNSS provide ad absolute auto-positioning where, in general, radio localization techniques provide a relative localization.

AoA algorithms are dependent on which type of signals the transmitter emits. Several techniques have been developed to locate radio sources emitting specific waveforms, i.e. narrow band signals [5, 6], broad band signals [7] and ad-hoc sequences [8]. Depending on the received signals characteristics different AoA methods are applicable. Furthermore, the algorithms can be designed ad-hoc to use certain waveforms and protocols, or they can work opportunistically by intercepting existing signals and requiring the minimum knowledge on the signal format itself. All local based methods [9], contrarily to distributed ones that rely on a sensor network [10–14], exploit the position of the radio source analysing the differences of its signal impinging on a receiving array of antennas. In case of wideband impulsive signals such as Ultra Wide Band (UWB) transmissions, the parameters that have to be estimated to obtain the AoA are the Time of Arrival (ToA) or the Differential-ToA (D-ToA) [7]. The ToA can be used for ranging measurements [15, 16] and for AoA estimations in a passive multiple receiver scenario with a single active source but its calculus needs synchronization between transmitter and receiver. Thus an ad-hoc synchronized system must be settled [17] or a synchronization routine for the receiver must be developed [18]. The D-ToAs estimations don't need synchronization between transmitter and receiver because their computation does not involve ToAs knowledge directly [19]. However, D-ToAs method do not provide directly a raging estimation. The accuracy achievable by ToA and D-ToA methods is extremely dependent on the time resolution of the received impulse, and then on its bandwidth, the wider the better. These methods that measure the timing of signals fronts are sensitive to the distance between sensors, the further the better, since received signals are more separated in time [20]. Hence, ToA and D-ToA methods for AoA estimation of impulsive broadband signals are better suited for a distributed sensor localization approach such as Wireless Sensor Networks (WSNs) [21] or a cellular Base Station (BS) perspective [22]. In case of narrowband signals, such as Radio Frequency (RF) carriers or numeric transmissions, the parameter that has to be estimated to obtain the AoA is the Phase of Arrival (PoA). The PoAs are the phases of the signals received by each antenna. The Differential-PoA (D-PoA) approach for AoA detection imposes the employment of confined arrays w.r.t. ToA methods because of the limited periodic domain of the phase, forcing a local computation of AoA w.r.t. distributed approaches. For the reasons exposed above, a local-based (not distributed) localization approach is achievable using small arrays and a D-PoA approach to exploit localization parameters from narrowband signalling. The aim of this work is to exploit the AoA estimating the D-PoA from narrowband signals such as sine waves and Quadrature Amplitude Modulation (QAM) waves received by an antenna array.

One of the most detrimental effects that affect the radio communication systems is the Multi-path (MP). The MP affect also AoA systems reducing the localization precision. For this reason in Ch. 4 a geometric scattering model for MP is considered to investigate the robustness of the proposed algorithms. A radio-localization system consisting in N_a receiving antennas, 1 transmitting antenna and N_p impairing scatterers is considered [4,9]. The receiving array pattern is arbitrary and can follow the most common L-shape [23] or others geometries, such as circular arrays [24], arbitrary shapes [25] of optimized ones [26, 27]. In Sec. 4.2 is described how to interpret a Uniformly Sampled Channel Impulse Response (CIR) (US-CIR) in terms of geometric position of the scatterers. The relations between the CIRs of different sensors of the same array w.r.t. the same radio source are investigated in Sec. 4.3. The emulation of a geometric based MP channel for a complete array relying on the position of its sensors and one main CIR is discussed in Sec. 4.4. The effects of MP on QAM transmissions and the connection between scatterers positions and the probability density function (pdf) of the received signals is investigated in Sec. 4.5.

Another detrimental cause that impairs the communication systems, comprising AoA systems, is the non ideality of hardware components. The communication systems are composed at the transmitter by a defined set of essential hardware components [28]. These hardware blocks in real scenarios do not have an ideal behaviour and are affected by specific impairments that decrease their performance [29, 30]. The reduction of hardware impairments effects on RF communications is achieved on one hand by improving hardware components quality and on the other hand by developing compensation algorithms [31,32]. In Ch. 3 the RF communication systems affected by hardware non idealities are modelled and analysed. The impairing effects on digital communications of a set of impaired hardware components is discussed. In particular the effects caused by the impaired transmitter components such as Direct Current (DC) Offset (DCO) (Sec. 3.3), I-Q Unbalance (IQU) (Sec. 3.4), I-Q Skew (IQS) (Sec. 3.5) and Phase Offset (PO) (Sec. 3.6) are investigated. The statistical patterns imposed on the pdfs of received signals by the impaired hardware are interpreted in Ch. 5 such as hardware fingerprints in AoA discovery.

In Ch. 5 two AoA estimation algorithms that are designed to work opportunistically, using random QAM signals, and passively, without the need of calibration or previously agreed protocols are presented. In Sec. 5.1 the Constellation Statistical Pattern Identification and Overlap (CSP-IDO) algorithm is presented [33]. The main features of the proposed technique, namely CSP-IDO, are its reduced hardware needs, its robustness to the hardware impairments of the transmitter, and its fully passive/opportunistic applicability. The CSP-IDO method, illustrated in Sec. 5.1.4, is based on the analysis of the pdfs of successive signal snapshots taken from the antennas (asynchronous approach). Contrariwise, other AoA methods, such as beamforming [34,35] and root-MUltiple SIgnal Classification (MUSIC) (root-MUSIC) [36], have been conceived to synchronously (in parallel) acquire signals from the antenna elements (synchronous approach). In Sec. 5.2 an extension of CSP-IDO is presented. The CSP-IDO method exploits the statistical phase pattern of the received signals to estimate the D-PoA. Instead, the proposed CSP-IDO extension, namely Bi-dimensional (2D) CSP-IDO (BCID), exploits the D-PoA, from the full bi-dimensional statistical pattern of received signals showing more robustness w.r.t. the impairments of the receiver. Furthermore, both CSP-IDO and BCID are able to improve their performance exploiting the transmitter impaired hardware signature introduced in Ch. 3. Since the use of the proposed methods exploits the received signals pdfs, their application is feasible with any type on numerically modulated signal, such as QAM. The performance has been evaluated also in scenarios where the estimation process is affected by MP and impaired by hardware at the receiver showing enough robustness. Proposed techniques thanks to their passive/opportunistic approach to AoA localization and thanks to the limited hardware usage are suited to be applied in a eavesdropping scenario with low-end hardware.

Differently to the static methods proposed in Ch. 5 in Ch. 6 are discussed, implemented and tested two possible applications for dynamic AoA tracking using Particle Filtering (PF) algorithms. Sec. 6.1 is focused on the application of AoA estimation in the automotive scenario. A vehicular communication network most likely based on Institute of Electrical and Electronic Engineers (IEEE) 802.11p [37] will become soon a reality. This will enable the establishment of ad-hoc car networks for the diffusion and gathering of sensor information and the implementation of a plethora of new services [38]. Among all possible new applications, the most important ones are probably those that exploit localization information, i.e., context aware services. In this respect, Global Positioning System (GPS) positioning plays an important role in the full development of this ecosystem of services. However, the usage of other localization technologies is relevant in situations where GPS does not fulfil the requirements, e.g., in terms of precision, response time, and coverage. The usage of Road Side Units (RSUs)) that detect position information from vehicles is interesting for instance to offer a traffic control monitoring service for safety [39] or vehicle flows analysis and management [40], or it can be an enabling service for consumer applications like driver assistance and in the emerging technology of self-driving cars. Therefore, a different type of localization method that exploits an existing vehicular communication network infrastructure (and in particular the IEEE 802.11p network) in an "opportunistic" way is discussed. The proposed method tries to obtain the vehicles position, in a certain area, by listening to Vehicle-to-Vehicle (V2V)-Vehicle-to-Infrastructure (V2I) communication signals using an RSU. Such an approach can avoid the use of GPS or complement it, provide more accuracy and reliability in certain scenarios. Essentially, this approach is host-based, i.e., it is made directly by the RSU node. This AoA estimation approach can be challenging because of hardware impairments (as phase noise) and multipath propagation [41]. AoA estimation can be done with subspace methods as the MUSIC algorithm [42] which detect multiple emitters and compensate, in part, multipath effects. A simple AoA phase differential approach is considered. Then, the AoA estimates are refined using a statistical method based on PF [43]. Particle filtering was proposed originally for iteratively estimate the hidden state of a dynamic system approximating its continuous pdf with a weighted set of M discrete samples [44]. The experimental test bed visible in Fig. 6.1 has been deployed to evaluate algorithm performance.

Sec. 6.2 is focused on the application the AoA estimation in a Unmanned Aerial Vehicle (UAV) localization scenario. UAVs are attracting considerable attention since they can be used for a number of consumer, industrial and military applications ranging, for instance, from sport video making to environmental monitoring and parcel delivery [45,46]. A key component is the technology that allows to locate and navigate the UAVs. Presently, GNSS and inertial sensors are used to provide information on position, speed and direction of movement. Reliable localization is very important also in view of new regulations that aim at better controlling the use and the status of the UAVs for higher safety and security [47]. Furthermore recently UAVs technology has started to be under the spotlight of police audits because of possible security threats [48].In Sec. 6.2, a radio localization approach is considered and it is based on azimuth and elevation positioning using a transmitting source as a reference. Azimuth and elevation are determined by processing with PF the signals that impinge on a Three-Axial-Uniform Linear Array (ULA) (3A-ULA). The

3A-ULA can be mounted either on a ground base station or on the UAVs. In the first case, namely Ground Localization Scenario (GL-S), the base station passively eavesdrops the signals emitted by the UAVs to determine their angular coordinates. In the latter case, namely Self Localization Scenario (SL-S), the ground node acts as a radio anchor allowing UAVs self localization. The system can be used in a standalone way or to complement existing GNSS or inertial sensors employing data fusion techniques [49].

2

AoA Estimation Techniques

Radio localization techniques such as Angle of Arrival (AoA) algorithms play an important role in the wider universe of positioning systems, exempli gratia (for the sake of an example) (e.g.), Global Navigation Satellite Systems (GNSSs) [1] applications. The advantage of terrestrial radio localization based methods [2] with respect to (w.r.t.) GNSS is its feasible deployment in environments where satellite visibility is not fully achievable, id est (that is) (i.e.) indoor and canyon like scenarios [3]. Radio localization techiques can be used to implement auto-positioning using known radio anchors or, dually, to remotely locate unknown radio sources [4]. Furthermore, terrestrial radio localization techniques such as AoA do not need the deployment of the extremely expansive and complex satellite constellation infrastructure of GNSS. However, despite the complexity, GNSS provide ad absolute auto-positioning where, in general, radio localization techniques provide a relative localization.

Introduction

The aim of AoA techniques (called also Direction of Arrival (DoA)) [2, 4, 9] is to estimate the angular position ϕ of a radio source w.r.t. a receiver Fig. 2.1. Angular localization of radio sources is used in a wide set of scenarios such as Unmanned Aerial Vehicle (UAV) navigation and positioning [50], Radio Frequency (RF) Identification (RFID) tags monitoring [51] and wildlife monitoring [52]. The AoA receiver is equipped with an antenna array. The AoA estimations are made elaborating the signals impinging on each sensor of the array. The AoA methods can be used jointly with data fusion techniques [49, 53] using ranging sensors [54] to provide the full localization of the emitter. Full Three-dimensional (3D) localization can also be reached using jointly AoA estimates of several receivers in different positions [55].

Changing the point of view to a self localization perspective, AoA estimation, if applied to a scenario with radio emitting anchors with known position or pattern, allows the

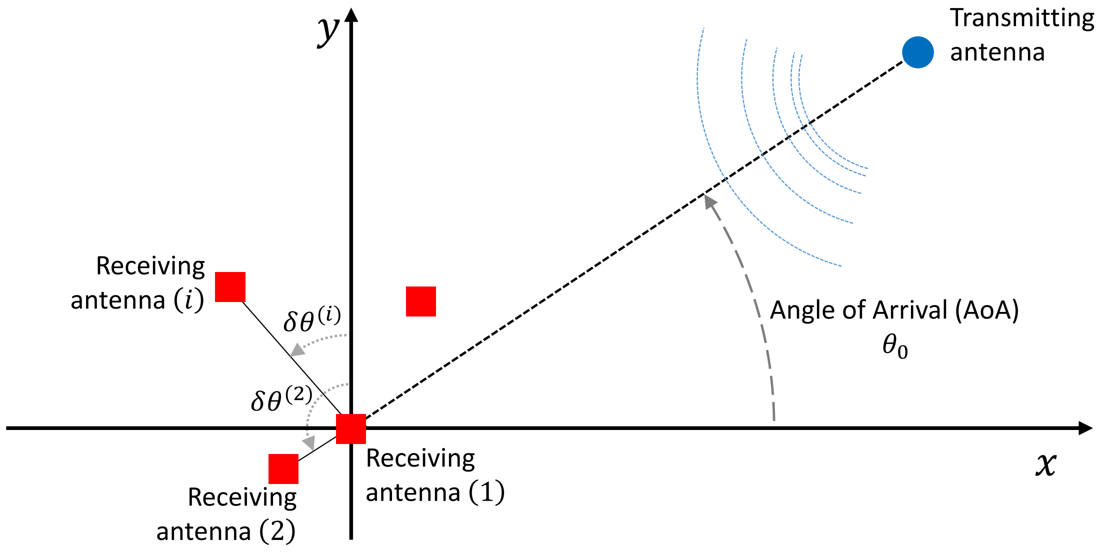

Figure 2.1: AoA estimation array system.

receiver Bi-dimensional (2D) or 3D self positioning [6].

AoA algorithms are dependent on which type of signals the transmitter emits. Several techniques have been developed to locate radio sources emitting specific waveforms, i.e. narrow band signals [5, 56], wide band signals [7, 22, 57, 58] and ad-hoc training sequences [8, 59]. Furthermore, the algorithm can be designed ad-hoc to use certain predetermined waveforms or protocols [60] or it can work opportunistically by intercepting existing signals and requiring minimum knowledge on the signal format itself Ch. 5.

In the following Sections features and techniques of AoA estimation methods applied to different scenarios are presented.

Opportunistic and Assisted Techniques

One important feature of AoA techniques is how much the localization is coordinated and concerted between the involved nodes.

In the most complete scenario, herein named Fully Assisted AoA (FA-AoA) scenario, the transmitter and the receiver are connected with an ad-hoc service channel to allow localization [10, 61–63]. Through this connection the receiver instructs the transmitter and sends signals specification and scheduling times, allowing a fully assisted localization approach. The evident quality of this technique is the flexibility on transmitted waveforms and its versatility for on-demand-like positioning applications. The drawback is the complexity caused by the control channel and the high level protocols management, that implies the creation of an ad-hoc communication protocol and more complex units.

Non assisted methods, namely Opportunistic AoA (O-AoA), have a totally passive approach to localization, without the collaboration or the knowledge of the transmitter. In the O-AoA the receiver exploits the position of the receiver from generalized RF signals.

The receiver has only a low level knowledge about the transmitter, for example the the modulation scheme, such as Quadrature Amplitude Modulation (QAM) [33], the central frequency or the existence on training sequences such as orthogonal signatures like in Long Term Evolution (LTE) [64,65],Universal Mobile Telecommunications System (UMTS) [66, 67] or channel estimation sequences [68] like in Global System for Mobile Communications (GSM) [69].

Partially Assisted AoA (PA-AoA) methods have hybrid proprieties w.r.t. FA-AoA and O-AoA techniques [70]. PA-AoA does not involve communication between transmitter and receiver but uses a pre-agreed algorithm or known signal. In PA-AoA methods the receivers can exploit the position of transmitter through previously agreed signals, sent for example in planned times or intervals.

The collaborative multi receiver schemes designed to provide 2D or 3D localization mentioned in Sec. 2.1 introduce the further complexity typical of Wireless Sensor Networks (WSNs) [21]. In fact, to apply data fusion or in general data aggregation in a WSN scenario several service channel must be deployed because of the intrinsic necessity to spread/aggregate the information across the distributed architecture of sensors.

The aim of this work is to exploit AoA from radio signals opportunistically i.e. without the need of coordination among nodes. Such techniques, implemented by non-collaborative nodes, in general achieve less precision that ad-hoc methods but can be applied in a broader set of scenarios and are more flexible. Then, the algorithms treated in this work are designed to eavesdrop already existing communication signals and to locate their radio source with nearly-zero knowledge of the signal and without the collaboration of the transmitting node.

Received Signals Types

A central characteristic that distinguish AoA methods is the type of signals involved in the localization techniques. Depending on the received signals different AoA methods are applicable. All local based methods, contrarily to distributed ones such as WSN, exploit the position of the radio source analysing the differences of its signals impinging on a receiving array of antennas.

In case of wideband impulsive signals with sharp patterns in time, the parameter that has to be estimated to obtain the AoA is the Time of Arrival (ToA) or secondary the Differential-ToA (D-ToA) [7, 71]. The ToA is the time that the sent signal takes to go from the transmitter antenna to the receiver antenna. The ToA can be used for ranging measurements and for AoA estimations in a multiple receiver scenario. The ToA estimation needs synchronization between transmitter and receiver to be correctly computed. Thus an ad-hoc synchronized system must be settled [17] or a synchronization routine for the receiver must be developed [18]. The D-ToAs are the difference of arrival times of the emitted impulse between the couples of antenna sensors at the receiver. The D-ToAs doesn't need synchronization between transmitter and receiver because their computation doesn't involve ToAs knowledge directly [19].

The accuracy achievable by ToA and D-ToA is extremely dependent on the time duration of the impulse and then to its bandwidth. Using a D-ToA approach with wideband signals for DoA estimation the precision increases with the distance between array elements, since received signals are more separated in time [14, 20]. Hence, ToA and D-ToA methods for AoA estimation of impulsive broadband signals are better suited for a distributed sensor localization approach such as WSNs [21] or a cellular Base Station (BS) perspective [22].

In case of narrowband signals, such as RF carriers or QAM transmissions, the parameter that has to be estimated to obtain the AoA is the Phase of Arrival (PoA). The PoAs are the phases of the signals received by each antenna sensor. In particular, it is exploited the Differential-PoAs (D-PoAs) that is the difference between the phases of the impinging waveforms detected by each antenna. As discussed in Sec. 2.4, because of the periodic support of the D-PoA, namely $[-\pi, pi[$, it is necessary to force an upper bound in the inter antenna distance of the array to uniquely detect the phase [20]. The D-PoA approach for AoA detection allows/imposes the employment of more confined arrays w.r.t. D-ToA methods, forcing a local computation of AoA w.r.t. the distributed approaches.

For the reasons exposed above, a local-based (not distributed) localization approach is achievable using small arrays and a D-PoA approach to exploit localization parameters from narrowband signalling. The aim of this work is to exploit the AoA from narrowband signals such as sine waves or QAM waves.

Phase of Arrival Methods

As discussed in Sec. 2.2 and Sec. 2.3 the purpose of this work is to opportunistically estimate the AoA of a transmitter exploiting its emitted narrowband signals. The standard localization scenario that will be considered in the following is visible in Fig. 2.1. It is constituted, at the receiver side, by an array of N_a antennas each one positioned in the 3D space at the coordinates $[x^{(i)}, y^{(i)}, z^{(i)}]$. The transmitter is positioned in $[x^{(TX)}, y^{(TX)}, z^{(TX)}]$. Signals emitted from transmitter are considered impinging receiver antenna array as plane waves [72], for this reason its distance from receiver array must be substantially greater than array size w.r.t. carrier wavelength λ_0. Considering a numerical narrowband RF transmission the demodulated signal sampled at rate $1/T_{symb}$, is

$$s_n^{(i)} = A_n e^{j\psi^{(i)}} + w_n^{(i)}, \tag{2.1}$$

where the index i identifies the antenna of the array and n represents the time instant nT_{symb}. The Additive White Gaussian Noise (AWGN) is represented by the term $w_n^{(i)}$. The numerical symbols transmitted by the numerical modulation such as Amplitude Phase Shift Keying (PSK) (A-PSK) or QAM are defined by the parameter $A_n = |a_n|e^{j\xi_n} \in \mathcal{A}$ that is considered a uniform random variable inside its limited set of values $\mathcal{A}$. T_{symb} is the symbol period. The parameter $\psi^{(i)}$ represents the PoA of the transmitted signal impinging to the i-th antenna, in particular

$$\psi^{(i)} = 2\pi f_0 \tau^{(i)} \tag{2.2}$$

where $\tau^{(i)} = D^{(i)}/c_0$ is the i-th ToA. The distance between the transmitting antenna and the i-th receiving sensor of the antenna array is $D^{(i)}$ and f_0 is the carrier frequency of the RF numerical transmission. The constant c_0 represents the speed of light an its value is 299792458m/s. Since the parameter used for the AoA estimation θ is the D-PoA $\delta\psi^{(i)} = \psi^{(i+1)} - \psi^{(i)}$, its calculus is related to the inter-antenna distance $d^{(i)}$:

$$\begin{aligned} \delta\psi^{(i)} &= \left[\psi^{(i+1)} - \psi^{(i)}\right] \pmod{2\pi} \\ &= \left[2\pi f_0(\tau^{(i+1)} - \tau^{(i)})\right] \pmod{2\pi} \\ &= \left[2\pi \frac{d^{(i)}}{\lambda_0} \sin\left(\theta + \delta\theta^{(i)}\right)\right] \pmod{2\pi} \end{aligned} \tag{2.3}$$

where $\delta\tau^{(i)}$ is the D-ToA for the antenna i and the operator $[\cdot] \pmod{2\pi}$ represents the modulo operator with interval 2π . The parameter $\delta\theta^{(i)}$ is a phase adjustment factor that expresses the physical inclination of the i-th and the $i+1$-th couple of antennas w.r.t. the y axis. The support of the phase is limited and periodic, for this reason to uniquely decode the D-PoA for every possible AoA θ between $-\pi$ and π it must be that

$$|2\pi \frac{d^{(i)}}{\lambda_0} \sin\left(\theta + \delta\theta^{(i)}\right)| \leq \pi \quad \forall(\theta + \delta\theta^{(i)}) \in [-\pi/2, \pi/2) \implies d^{(i)} \leq \lambda_0/2 \tag{2.4}$$

where $\lambda_0 = c_0/f_0$ is the carrier frequency wavelength. As discussed in [20] the constrain in (2.4) limits the use of D-PoA methods to small sized antenna arrays. Considering the scenario of (2.1) depicted in Fig. 2.1 the D-PoA $\delta\psi^{(i)}$ can be calculated as

$$\delta\tilde{\psi}^{(i)} = \underline{/s_n^{(i+1)}} - \underline{/s_n^{(i)}} \tag{2.5}$$

where

$$\begin{aligned} E\left[\delta\tilde{\psi}^{(i)}\right] &= E\left[\underline{/A_n e^{j\psi^{(i+1)}} + w_n^{(i+1)}} - \underline{/A_n e^{j\psi^{(i)}} + w_n^{(i)}}\right], \\ &= \underline{/A_n e^{j\psi^{(i+1)}}} - \underline{/A_n e^{j\psi^{(i)}}}, \\ &= \psi^{(i+1)} - \psi^{(i)} = \delta\psi^{(i)}. \end{aligned} \tag{2.6}$$

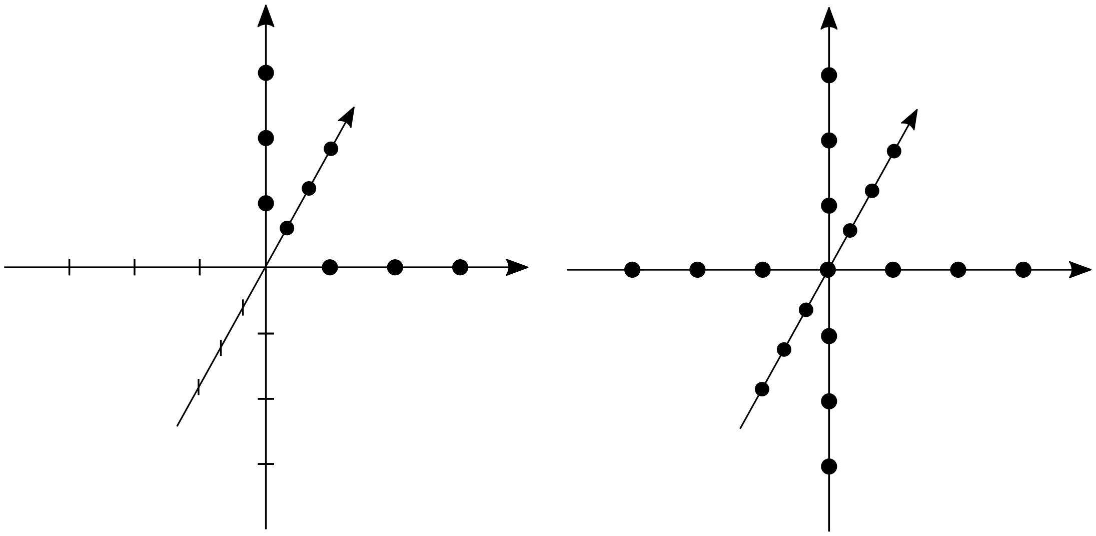

Figure 2.2: Arrays for AoA estimation. L array (left). X array (right).

and where $\delta\tilde{\psi}^{(i)}$ is the estimation of the real D-PoA $\delta\psi^{(i)}$ and the operator $E[\cdot]$ represents the expected value. The noise component in 2.1 does not affect 2.6 because of the expectation operation. The value of $\delta\tilde{\psi}^{(i)}$ is then used to estimate with $\tilde{\theta}^{(i)}$ the AoA θ:

$$\tilde{\theta}^{(i)} = \arcsin\left(-\frac{\delta\tilde{\psi}^{(i)}}{K^{(i)}}\right) - \delta\theta^{(i)} \tag{2.7}$$

where, as depicted in Fig. 2.1, $K^{(i)} = 2\pi d^{(i)}/\lambda_0$ expresses the inter element distance i normalized to the wavelength λ_0, in angles. Each antenna pair of the array produces an AoA estimation $\tilde{\theta}^{(i)}$, all estimations can be averaged in a single result. Otherwise, (2.7) can be applied to an average D-PoA between the N_{pairs} available antenna pairs of the array $\delta\tilde{\psi} = \sum_{i=1}^{N_{pairs}} \delta\tilde{\psi}^{(i)}/N_{pairs}$.

Antenna Array Patterns

The array of antennas used for AoA estimation is a fundamental part of receiver hardware since the received signals rely on the sensors position and geometry. The position of antennas in the array influences the received signals, in particular their time and phase shifts, as explained in (2.3). Different array geometries rely on different parameters for localization algorithms. The most common array configurations are Uniform Linear Array (ULA) and L-shaped arrays [23] for Mono-dimensional (1D) and 2D angular positioning, respectively (Fig. 2.2). Both systems described in Fig. 2.2 are composed of three branches each one composed by a ULA lying in a different axis. The ULAs are arrays composed by equispaced sensors lying on the same line, for this reason the schemes in Fig. 2.2 will be herein considered as 3D-ULAs (3D-ULAs). Usually contiguous antennas of the same branch have the same inter-element distance. As described in (2.4) inter-antenna distance is crucial for D-PoA estimators since it influences the estimation process. If a maximum range is fixed for the AoA estimation ($|\theta| < \theta_{max}$), the maximum value for the inter element distance d is

$$d \leq \frac{\lambda_0}{2} \frac{1}{\sin\left(\theta_{max}\right)} , \tag{2.8}$$

where for the sake of simplicity the array is considered parallel to the y axis: $\delta\theta$=0. On the other hand if the carrier wavelength λ_0 and the inter-element distance d are fixed, the range of the AoAs θ that can be correctly detected $|\theta| < \theta_{max}$ is limited by

$$\theta_{max} = \arcsin\left(\frac{\lambda_0}{2d}\right) , \tag{2.9}$$

where, again, for simplicity the array is considered parallel to the y axis: $\delta\theta$=0. Limitation expressed in (2.8) and (2.9) can be mitigated using complex arrays that lead to several AoA estimations $\tilde{\theta}^{(i)}$.

The arrays depicted in Fig. 2.2, exploit both azimuth and elevation coordinates of a RF source. In particular the L-shaped 3D-ULA in Fig. 2.2 is constituted, for each one of the 3 branches, by N_a antennas. Each branch is labelled with $a \in x, y, z$ to indicate along which one of the axes it is displaced. An antenna of the same branch a is indexed with $i \in [1, 2, \ldots, N_a]$ to indicate its position along the branch. Thus, the coordinates of the antennas can be written as

$$\begin{aligned} x^{(a,i)} &= (i-1)d\delta_{xa} , \\ y^{(a,i)} &= (i-1)d\delta_{ya} , \\ z^{(a,i)} &= (i-1)d\delta_{za} , \end{aligned} \tag{2.10}$$

where δ_{ij} is the Kronecker delta that is 1 for $i = j$ and 0 otherwise and d is the constant distance between antennas. The notation of received signal

$$s_n^{(a,i)} = A_n e^{j\psi_n^{(a,i)}} + w_n^{(a,i)}, \tag{2.11}$$

is compliant to (2.1) for all branches a. The D-PoAs for the branch a are defined as $\hat{\psi}_n^{(a)} = \psi_n^{(a,2i-1)} - \psi_n^{(a,2i)}$ $\forall i \in [1, 2, \ldots, N_a/2]$. In [73] a technique to estimate $\hat{\psi}_n^{(a)}$ is described. Applying this technique for the model considered allows to exploit the D-PoAs of the branches from the signal model introduced in (2.11). $\hat{\psi}_n^{(a)}$ are estimated as $\angle u_n^{(a)}$, where $\angle\cdot$ stands for the phase operator and where:

$$u_n^{(a)} = \frac{2}{N_a} \sum_{i=1}^{N_a/2} s_n^{(a,2i-1)} s_n^{(a,2i)^*} , \tag{2.12}$$

where an average over the $N_a/2$ distinct antenna pairs is performed to mitigate the AWGN effect. Using $u_n^{(a)}$, the angular spherical coordinates θ_n and ϕ_n are estimated respectively with $\tilde{\theta}_n$ and $\tilde{\phi}_n$ as following:

$$\begin{aligned}\tilde{\theta}_n &= \arctan\left(\sqrt{(\underline{\angle u_n^{(x)}})^2 + (\underline{\angle u_n^{(y)}})^2}, \underline{\angle u_n^{(z)}}\right), \\ \tilde{\phi}_n &= \arctan\left(\underline{\angle u_n^{(y)}}, \underline{\angle u_n^{(x)}}\right),\end{aligned} \tag{2.13}$$

where $\arctan(\cdot, \cdot)$ is the arctangent function extended to the $[0, 2\pi)$ domain.

In this work ULAs are used for AoA estimation however several array geometries are treated in literature, such as circular arrays [24] or more generic arrays [25]. Different techniques have been proposed to optimized arrays geometries in different scenarios, mainly minimizing the array Cramér-Rao Lower Bound (CRLB) w.r.t. AoA error [26, 27].

Hardware Architectures

The elaboration of radio signals impinging on antenna sensors of a pre-determined array for AoA exploitation can be performed using different receiving hardware schemes. Receiving architectures differ mainly on how much hardware is shared among each sensor branch.

Full Parallel Architecture (FPA)

The more complete solution is depicted for the sake of the example in Fig. 2.3. It provides N_a different receiving complex branches, each one comprising both In-phase (I) and In-quadrature (Q) channels, it is herein named FPA. FPA provides two completely independent complex receiving branches. Each antenna branch is provided by an independent oscillator as reference for the RF down-converting process. In case of impairing hardware, discussed in Ch. 3), each branch will provide completely independent received signals modifications. The most impairing effect is the asymmetric Phase Offset (PO), the phase misalignment between oscillators. For the sake of the example, this receiving scheme is used in [74] for AoA estimation and for the characterization of hardware impairments.

Partially Parallel Architecture (PPA)

The PPA architecture scheme partially shares hardware components, it depicted for the sake of the example in Fig. 2.4. This scheme provides N_a different receiving complex branches, each one comprising both I and Q channels, it is herein named PPA. The PPA provides two completely independent complex receiving branches except for the oscillator, that is in common between the branches. The common oscillator feeds all the mixers trough a splitter circuit. In case of impairing hardware, discussed in Ch. 3), each branch will provide different I-Q Unbalances (IQUs), Direct Current (DC) Offsets (DCOs) and I-Q Skews (IQSs). Branches will experience the same PO caused by the common oscillator.

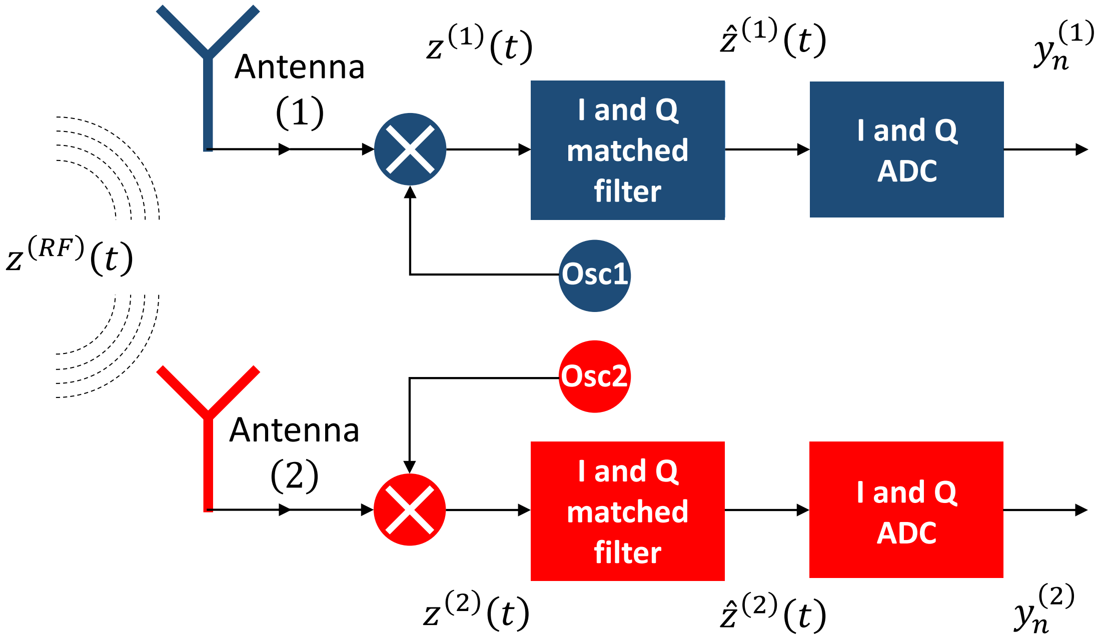

Figure 2.3: FPA receiving scheme, $N_a = 2$.

However, PO asymmetries can be verified if circuits that connect the oscillator splitter to the different mixers are affected by different delays. The difference between POs that affects the system is $2\pi f_0(l^{(2)} - l^{(1)})/c_0$, where $l^{(1)}$ and $l^{(2)}$ are the circuits lengths of the two connections that goes from the first mixer to the splitter and from the second mixer to the splitter, respectively.

Time Switched Architecture (TSA)

The Time Switched Architecture (TSA) architecture shares more components w.r.t. 2.6.1 and 2.6.2 and is treated in Ch. 5 and depicted for the sake of the example in Fig. 2.5. It provides 1 receiving branch, that is shared among all receiving antennas. Antennas are then time duplexed in the shared receiving architecture, namely TSA. Antenna branches share, in the case of hardware impairments, the same IQU, DCO, PO and IQS. The TSA provides also different PO because the oscillator is common for all antennas. However, PO asymmetries can be verified if connections that connect the antenna switch to the different antennas are affected by different delays. The difference between POs that affects the system is $2\pi f_0(L^{(2)} - L^{(1)})/c_0$, where $L^{(1)}$ and $L^{(2)}$ are the circuits lengths of the two connections that goes from the first antenna to the switch and from the second antenna to the switch, respectively. This type of architecture is used in Ch. 5 and [33] for AoA purposes exploiting its impaired hardware fingerprint.

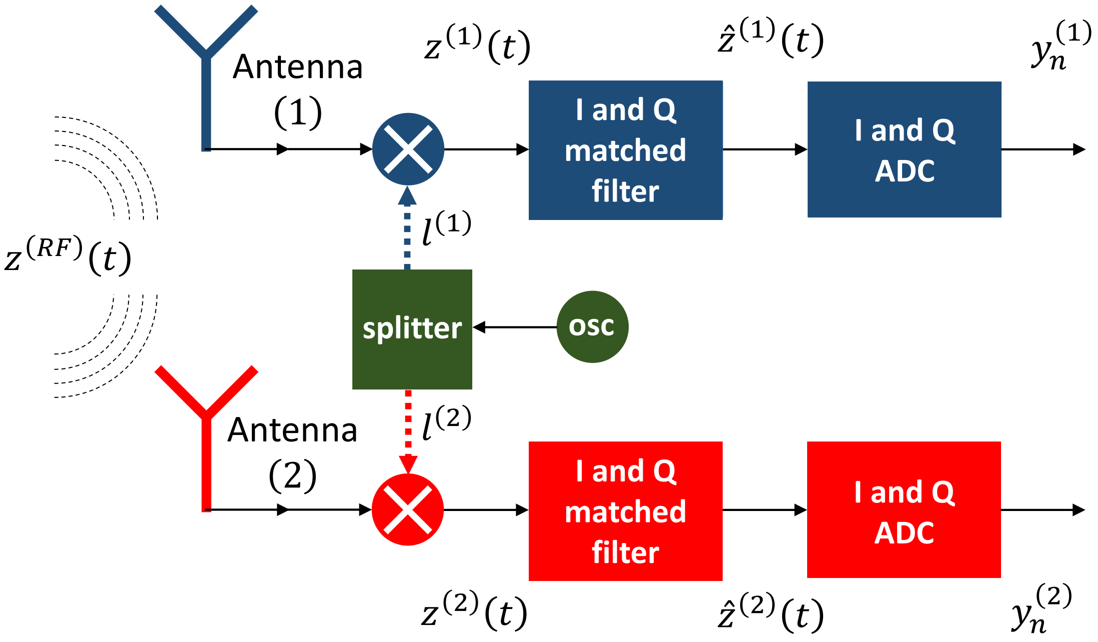

Figure 2.4: PPA receiving scheme, $N_a = 2$.

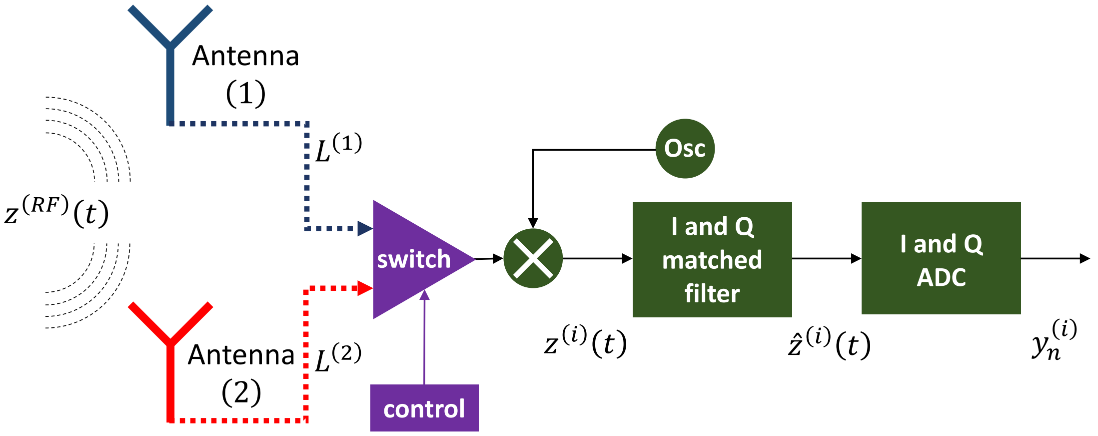

Figure 2.5: TSA receiving scheme, $N_a = 2$.

Error Evaluation

The AoA estimation algorithms performance are evaluated computing the root-mean-square (RMS) error (RMSE) parameter. This value is defined as

$$\theta_{\mathrm{RMSE}}(\theta) = \sqrt{\frac{\sum_{n=1}^{N} (\theta - \theta_{est})^2)}{N}} \tag{2.14}$$

where θ is the real AoA, θ_{est} is the estimated AoA and N is the number of estimations processed by the algorithm. The RMSE, assuming an unbiased estimation, is the standard deviation of the estimation error $\theta - \theta_{est}$. To fix the ideas in a 1D example, the value θ_{RMSE} can be used to generate an angular uncertainty interval around the real value θ: $B(\theta) = [\theta - \theta_{\mathrm{RMSE}}, \theta + \theta_{\mathrm{RMSE}}]$. From the Čebyšëv's inequality, about the 68% of estimations for θ fall inside the uncertainty interval $B(\theta)$ if the error id Gaussian. Such error interval $B(\theta)$ graphically shows how wide is the estimation error since it contains the 68% of the iterated estimations.

Considering a 2D scenario where both azimuthal AoA ϕ and elevation AoA θ are jointly estimated, an error evaluation parameter is herein proposed. A standard approach is to calculate both RMSEs for azimuthal and elevation coordinates: $\theta_{\mathrm{RMSE}}(\theta, \phi)$ and $\theta_{\mathrm{RMSE}}(\theta, \phi)$. Both RMSEs are dependent by ϕ and θ. However, in this 2D angular scenario $\theta_{\mathrm{RMSE}}(\theta, \phi)$ and $\phi_{\mathrm{RMSE}}(\theta, \phi)$ do not give a correct error perception like in the previous 1D scenario. In fact, if for the sake of the example we consider an estimation algorithm with $\phi_{\mathrm{RMSE}} = 5°$, the same RMSE value in $\theta = 10°$ will lead to a lower position knowledge w.r.t. the same RMSE in $\theta = 85°$, see Fig. 2.6. This phenomenon is due to the definition of the spherical coordinates system that lead to smaller circles of latitude near the poles w.r.t. the equator.

In order to have a better angular error estimation parameter, a new metric is proposed, the Solid Angle RMSE (SARS). The SARS $\Omega_{\mathrm{RMSE}}(\theta, \phi)$ is defined as the solid angle occupied by the uncertainty surface $\mathscr{B}(\theta, \phi)$, that is lying on a unitary sphere. $\mathscr{B}(\theta, \phi)$ is delimited along the elevation coordinate by the two circles of latitude located in $\theta - \theta_{\mathrm{RMSE}}(\theta, \phi)$ and $\theta + \theta_{\mathrm{RMSE}}(\theta, \phi)$. The surface $\mathscr{B}(\theta, \phi)$ is bounded along the azimuthal coordinate by the two meridians positioned in $\phi - \phi_{\mathrm{RMSE}}(\theta, \phi)$ and $\theta + \theta_{\mathrm{RMSE}}(\theta, \phi)$. The considered surface is a spherical rectangle [75] centred in $[\theta, \phi]$, its angular area can be calculated as

$$\Omega_{\mathrm{RMSE}}(\theta, \phi) = \frac{1}{\pi} \phi_{\mathrm{RMSE}}(\theta, \phi) \sin\left(\frac{\theta_{\mathrm{RMSE}}(\theta, \phi)}{2}\right) \sin(\theta) \, . \tag{2.15}$$

$\Omega_{\mathrm{RMSE}}(\theta, \phi)$ is an a-dimensional parameter that express the angular area of $\mathscr{B}(\theta, \phi)$ in steradians normalized by the angular area of the hemisphere, that is 2π [sr]. In Fig. 2.6 are depicted on a unit hemisphere 5 examples of spherical rectangles $\mathscr{B}(\theta, \phi)$ generated with the same RMSEs, namely $\theta_{\mathrm{RMSE}} = \phi_{\mathrm{RMSE}} = 20°$, but in different coordinates. In

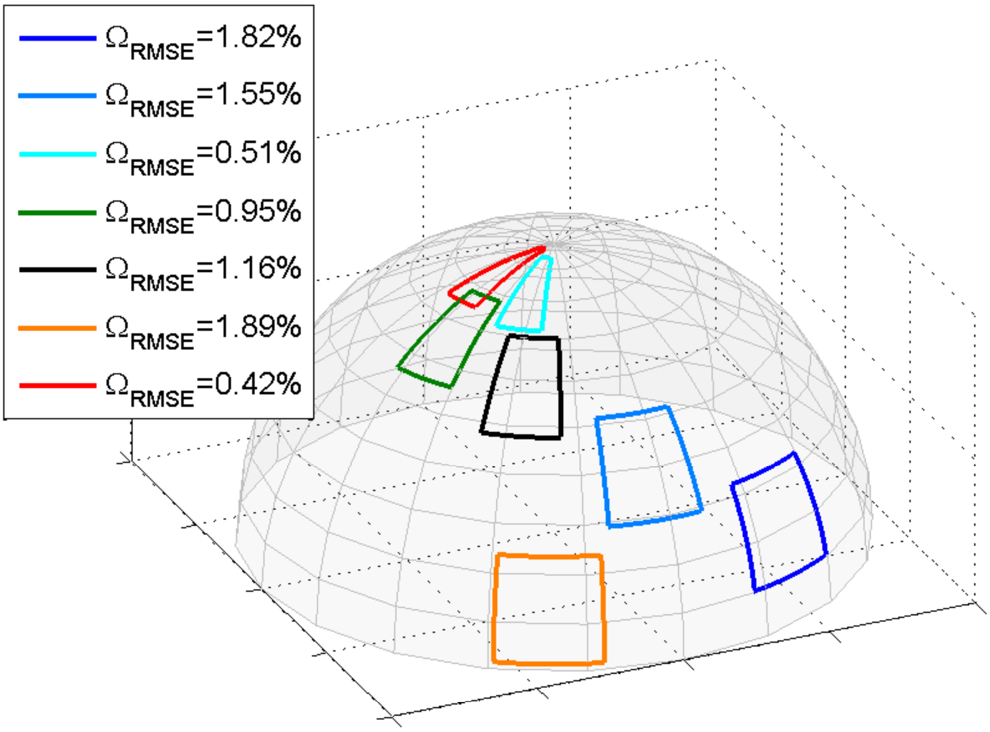

Figure 2.6: Example of 2D angular uncertainty surfaces $\mathscr{B}$ generated by the same 1D angular uncertainties $\delta\phi = \delta\theta = 20°$ and leading different Ω values.

Fig. 2.6 is evident how the same RMSEs generate different uncertainty surfaces at different coordinates

Conclusions

In this Sec. an overview of AoA techniques for radio sources localization has been carried out. In particular different scenarios have been introduced, such as AoA collaborative/opportunistic approaches (Sec. 2.2), received signals types (Sec. 2.3), estimation techniques (Sec. 2.4), receiving antenna arrays (Sec. 2.5) and hardware architectures (Sec. 2.6). Finally a novel parameter, namely SARS, is proposed to evaluate the performance of 2D AoA estimation algorithms. Then, the algorithms treated in the following (Sec. 6 and Sec. 5) will be designed to eavesdrop already existing communication signals and to locate their radio source with nearly-zero knowledge of the signal and without the collaboration of the transmitting node.

3

Hardware Impairments in AoA Estimation

In this Ch. the RF communication systems affected by hardware non idealities are modelled and analysed (Sec. 3.2). The impairing effects on digital communications of a set of impaired hardware components is discussed. In particular the transmitter components effects such as DCO (Sec. 3.3), IQU (Sec. 3.4), IQS (Sec. 3.5) and PO (Sec. 3.6) are investigated.

Introduction

Every communication system is, in general, composed at the transmitter by a defined set of essential hardware components [28]. These hardware blocks in real scenarios do not have an ideal behaviour and are affected by specific impairments that decrease their performance [29, 30]. The reduction of hardware impairments effects on RF communications is achieved on one hand by improving hardware components characteristics and receiving architectures and on the other hand by developing compensation algorithms [31, 32].

Hardware System Models

Considering, for the sake of the example, the zero intermediate frequency (zero-IF) [76,77] depicted in Fig. 3.1, the hardware modules that influence transmitted symbols are:

- the Digital-to-Analog Converter (DAC) for the digital-to-analogic signal conversion.
- the transmission filter that can be performed digitally before the DAC.
- the mixer for the frequency up-conversion,
- the oscillator that generates the sinusoidal signal for the frequency up-conversion,
- the 90° phase shifter for orthogonal bases generation needed in I and Q branches,

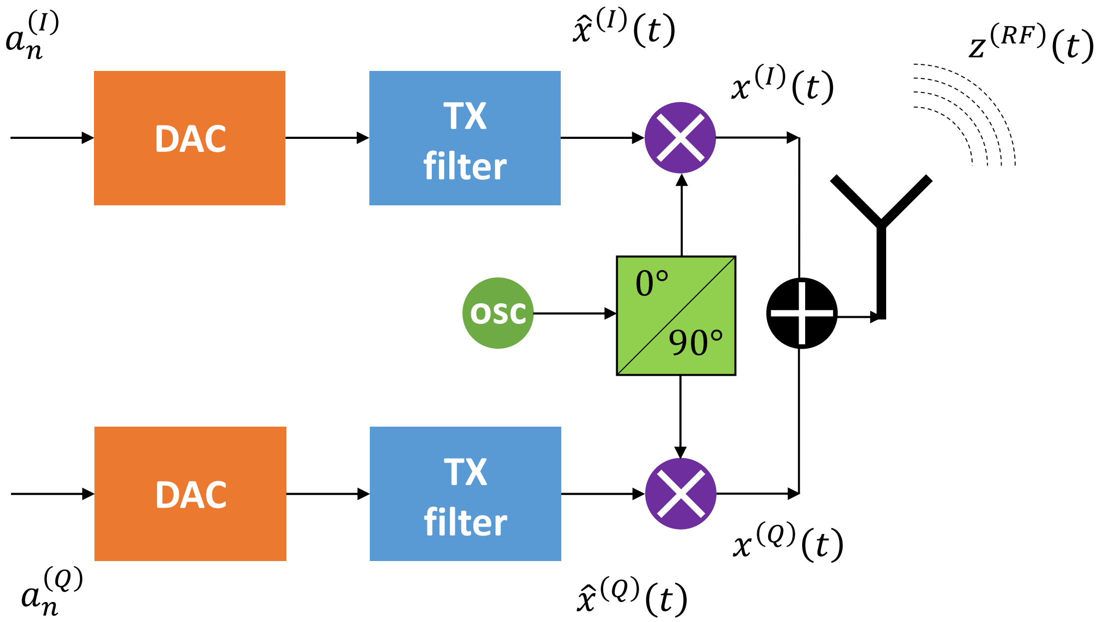

Figure 3.1: zero-IF transmitter.

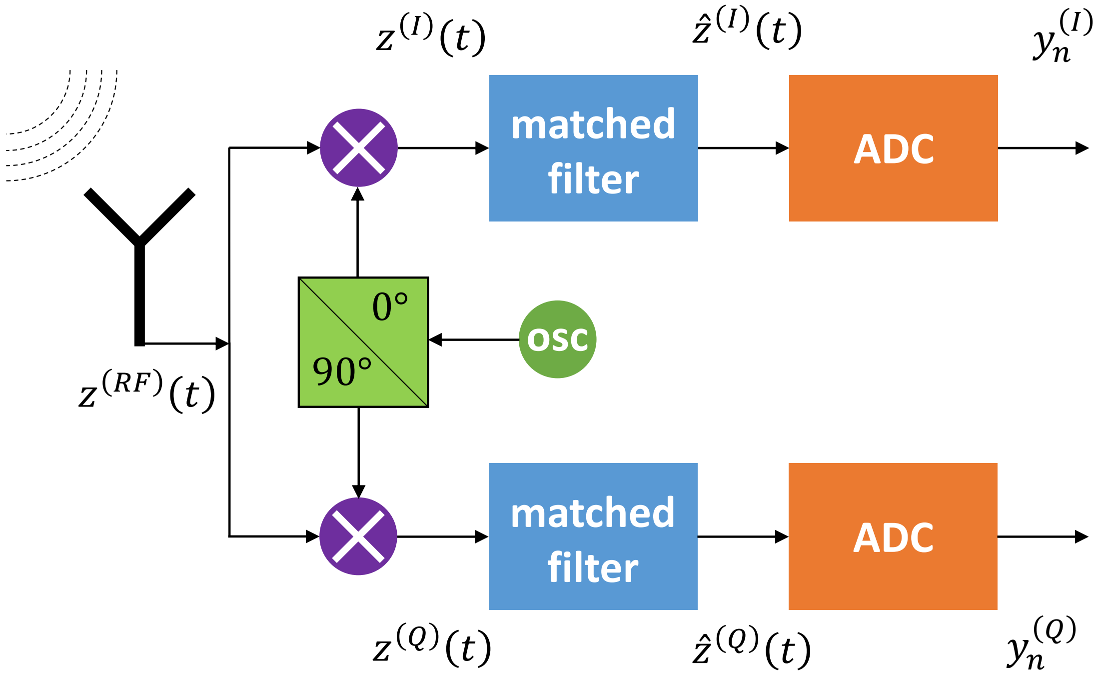

Figure 3.2: zero-IF receiver.

In the following of this Ch. the impaired hardware effects are treated and compared to the ideal case. The effects of hardware impairments on numerical modulations such as QAM and A-PSK [78,79] are treated. The transmitter architecture considered is depicted in Fig. 3.1 as a zero-IF. The receiver architecture considered is depicted in Fig. 3.2 as a zero-IF. The RF signal impinging at the receiver's antenna $z^{(RF)}(t)$ is generated modulating a numeric symbol a_n with a transmitting interpolation filter $g(t)$. Impinging signal $z^{(RF)}(t)$ is then down-converted by receiver branches generating

$$y_n = y_n^{(I)} + jy_n^{(Q)} \,, \tag{3.1}$$

where $y_n^{(I)}$ and $y_n^{(Q)}$ are the signals elaborated by the I and Q branches respectively. In the ideal case where impairments are not considered and where receiving filter is synchronized and matched with the transmitter's one

$$y_n = a_n + w_n \tag{3.2}$$

where symbols a_n are the elements of a unitary energy M-sized numerical constellation . The parameter $w_n \sim \mathcal{N}(0, \sigma_w)$ is the sampled additive white Circular-AWGN (C-AWGN) with zero mean and standard deviation σ_w. In Fig. 3.3 are depicted the ideal bi-dimensional probability density functions (pdfs) of the received complex signal y_n that express a QAM modulation, after all the receiving chain. The Fig. 3.3.(a) depicts the Cartesian Complex - pdf (C-CP) of y_n that jointly depicts the pdfs of of $\mathcal{R}[y_n]$ and $\mathcal{I}[y_n]$. The operators $\mathcal{R}[\cdot]$ and $\mathcal{I}[\cdot]$ represent the real part and the imaginary part operators, respectively. In the ideal case, considered in this Sec. , the joint pdf of the real and imaginary parts of y_n, namely $y_n^{(I)}$ and $y_n^{(Q)}$, is

$$f(y_n) = \sum_{m=1}^{M} P[a_n = a^{(m)}] \cdot f_{\mathcal{N}_2}\left(y_n, \begin{bmatrix} \mathcal{R}(a^{(m)}) \\ \mathcal{I}(a^{(m)}) \end{bmatrix}, \sigma_w^2 \mathbb{I}_2\right) \,, \tag{3.3}$$

where the matrix $\mathbb{I}_2$ is the 2×2 identity matrix. The symbol $a^{(m)}$ represents the m-th element of an M sized numerical constellation and its occurrence probability is $P[a_n = a^{(m)}]$. The function $f_{\mathcal{N}_2}$ in (3.3) represents the pdf of the Bivariate Normal Distribution (BND) that is defined as

$$\begin{aligned} f_{\mathcal{N}_2}(y, \bar{\mu}, \mathbf{\Sigma}) &= \frac{1}{2\pi|\mathbf{\Sigma}|^{1/2}} e^{\frac{1}{2}(\bar{y}-\bar{\mu})^T \mathbf{\Sigma}^{-1}(\bar{y}-\bar{\mu})} \,, \\ \bar{y} &= \begin{bmatrix} \mathcal{R}(y) & \mathcal{I}(y) \end{bmatrix}^T \,, \\ \bar{\mu} &= \begin{bmatrix} \mathcal{R}(\mu) & \mathcal{I}(\mu) \end{bmatrix}^T \,, \\ \mathbf{\Sigma} &= \begin{bmatrix} \sigma_{\mathcal{R}}^2 & \rho\sigma_{\mathcal{R}}\sigma_{\mathcal{I}} \\ \rho\sigma_{\mathcal{I}}\sigma_{\mathcal{R}} & \sigma_{\mathcal{I}}^2 \end{bmatrix} \,, \end{aligned} \tag{3.4}$$

where the vector $\bar{y}$ comprises the real and the imaginary parts of y, and $\bar{\mu}$ is the mean vector. The parameter $\mathbf{\Sigma}$ is the covariance matrix of the real and imaginary parts. The variables $\sigma_{\mathcal{R}}$ and $\sigma_{\mathcal{I}}$ are the standard deviations of $\mathcal{R}(y)$ and $\mathcal{I}(y)$, respectively. The parameter ρ is the correlation coefficient between $\mathcal{R}(y)$ and $\mathcal{I}(y)$.

The Fig. 3.3.(b) represents the Polar Complex - pdf (P-CP) of y_n that jointly depicts the pdfs (3.3) of $|y_n|$ and $\angle y_n$. The operators $|\cdot|$ and $\angle\cdot$ represent the absolute value and the phase operator, respectively. Equivalently the Fig. 3.4 shows respectively in (a) and (b) the P-CP and C-CP of y_n in (3.3) expressing an A-PSK modulation. The analytical

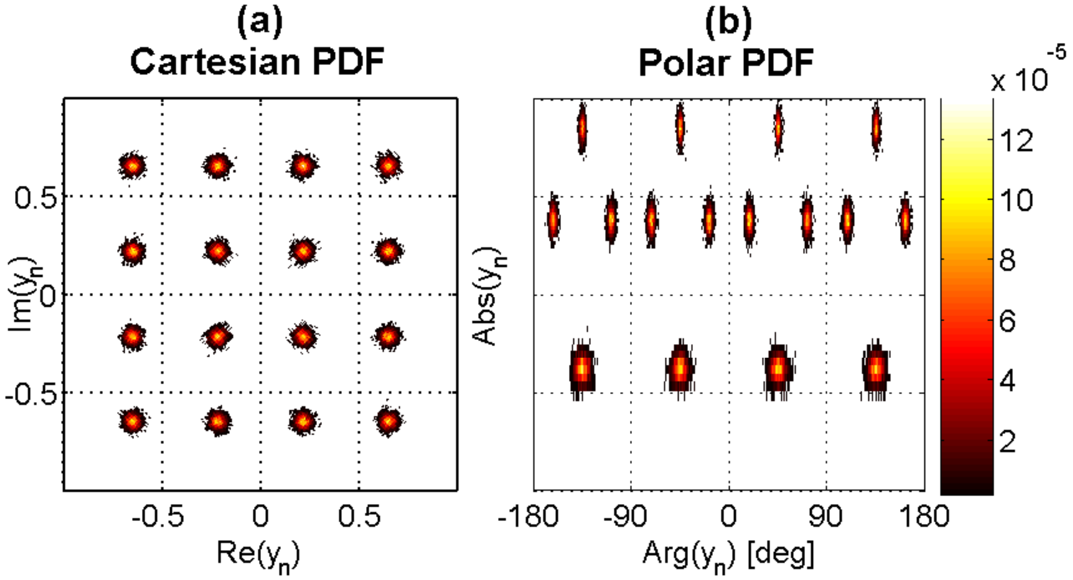

Figure 3.3: Received 16−QAM signal pdfs, ideal case. (a) C-CP. (b) P-CP.

expression in (3.3) supported by Fig. 3.3.(a) and Fig. 3.4.(b)show that the pdfs of the received signal are constituted by M BNDs translated into the complex coordinates of transmitted symbols, where M is the cardinality of the constellation. Both patterns of (3.3) generated by QAM and A-PSK show regular geometric behaviours, along x and y in the Cartesian representations,Fig. 3.3.(a) and Fig. 3.4.(a), and along the phase axis in the polar representations Fig. 3.3.(b) and Fig. 3.4.(b). In particular the depicted 16-QAM C-CP exhibits a $\sqrt{M}$ periods of symmetry for both x and y axis that are expressed in the P-CP with 4 periods of symmetry along the phase axis. The depicted 12-4-A-PSK pdfs exhibits in both a C-CP and P-CP 4 periods of symmetry along the phase axis. In the following of the Ch. the varying behaviour of this patterns will be analysed considering an impaired transmitter and an ideal receiver.

DC Offset (DCO)

The DC Offset (DCO) detrimental effect [31, 80] is caused by the non-ideal behaviour of the the DAC. The DAC [76] purpose as depicted in Fig. 3.1 is to change the transmitted

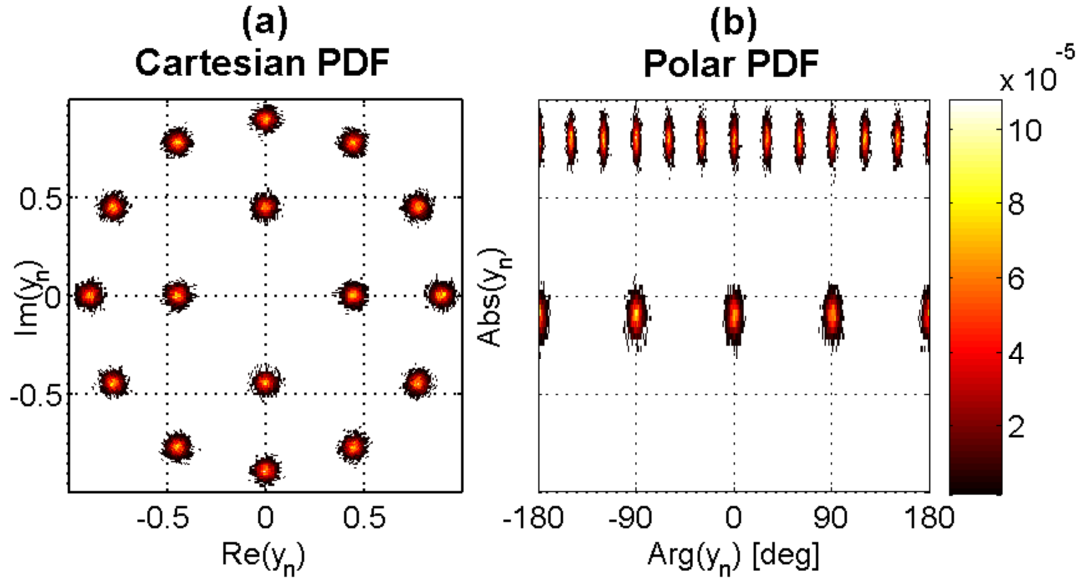

Figure 3.4: Received 8-4-A-PSK signal pdfs, ideal case. (a) C-CP. (b) P-CP.

symbols digital domain that is $\mathbb{Z}(T_{\text{symb}})$ to the analogic one $\mathbb{R}$. Typically inside a transmitter architecture are present two DACs, see Fig. 3.1, or a double input - double output DAC to convert both I and Q channels is present. The DAC is followed by a proper transmission filter g. The DACs I and Q input channels are respectively $a_n^{(I)}$ and $a_n^{(Q)}$, the real and imaginary parts of the transmitted symbols, respectively. Then, I and Q ideal output channels are respectively $\hat{x}_n^{(I)}$ and $\hat{x}_n^{(Q)}$, where:

$$\begin{aligned} \hat{x}^{(I)}_{(}t) &= x_n^{(I)} * g(t)\,, \\ \hat{x}^{(Q)}_{(}t) &= x_n^{(I)} * g(t)\,, \end{aligned} \tag{3.5}$$

where the transmitted symbols are shaped with the transmitting filter g.

DCO Hardware Causes

The input discrete signals of the DAC stage, namely $a_n^{(I)}$ and $a_n^{(Q)}$ don't have, in general, DC components:

$$\lim_{N\to\infty} \sum_{n=0}^{N} a_n^{(I)} = 0\,, \tag{3.6}$$

$$\lim_{N\to\infty} \sum_{n=0}^{N} a_n^{(Q)} = 0\,, \tag{3.7}$$

so that neither the continuous components $\hat{x}_(^{(I)}t)$ and $\hat{x}_(^{(Q)}t)$ have biases. The hardware realization of the DACs because of non ideal characteristics of electronic components [81] can generate a non zero bias for both real output channels $\hat{x}_{DCO}^{(I)}(t)$ and $\hat{x}_{DCO}^{(Q)}(t)$ w.r.t. ideal ones, $\hat{x}^{(I)}(t)$ and $\hat{x}^{(Q)}(t)$, respectively:

$$\begin{aligned} \hat{x}_{DCO}^{(I)}(t) &= \hat{x}^{(I)}(t) + \delta_{DCO}^{(I)}\,, \\ \hat{x}_{DCO}^{(Q)}(t) &= \hat{x}^{(Q)}(t) + \delta_{DCO}^{(Q)}\,, \end{aligned} \tag{3.8}$$

where respectively $\delta_{DCO}^{(I)}$ and $\delta_{DCO}^{(Q)}$ are the DC biases introduced by hardware imperfections by the DAC to I and Q channels, respectively.

DCO Effects on Constellations

The biases introduced by the impaired DCO [77] generate the following pdf at the receiver side for $y_{DCO,n} = y_{DCO,n}^{(I)} + jy_{DCO,n}^{(Q)}$

$$f_{\mathrm{DCO}}(y_{DCO,n}) = \frac{1}{M} \sum_{m=1}^{M} f_{\mathcal{N}_2}\left(y_{DCO,n}, \begin{bmatrix} \mathcal{R}(a^{(m)} + \delta_{DCO}) \\ \mathcal{I}(a^{(m)} + \delta_{DCO}) \end{bmatrix}, \sigma_w \mathbb{I}_2\right)\,, \tag{3.9}$$

where $\delta_{DCO} = \delta_{DCO}^{(I)} + j\delta_{DCO}^{(Q)}$ is the aggregated offset introduced to I and Q channels. The DCO affects the pdf translating its domain. The DCO impaired pdf expressed in (3.9) is depicted in Fig. 3.5 and Fig. 3.6 for a 16-QAM and a 12-4-A-PSK numerical constellation respectively. Both pdfs patterns for (3.9) generated by QAM and A-PSK show different geometric behaviours w.r.t. the ideal ones depicted in 3.3 and 3.4, respectively. In particular, because of the bi-dimensional translation of the pdf in the Cartesian space of $[\delta_{DCO}^{(I)}, \delta_{DCO}^{(Q)}]$ and in the polar space of $[|\delta_{DCO}|, \angle\delta_{DCO}]$ the symmetries of the ideal case do not longer holds.

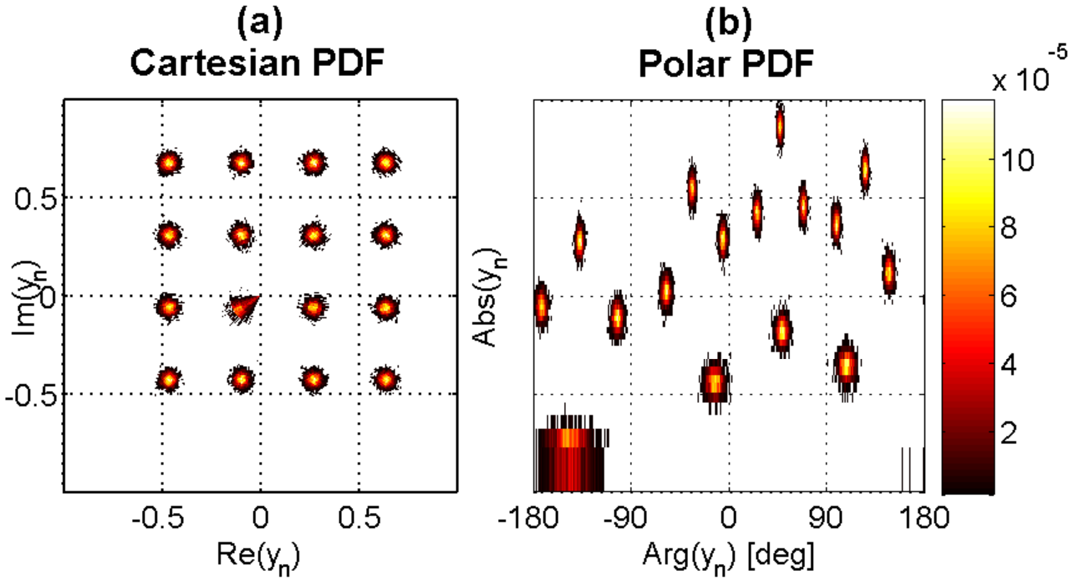

Figure 3.5: Received 16-QAM signal pdfs showing DCO effects. (a) C-CP. (b) P-CP.

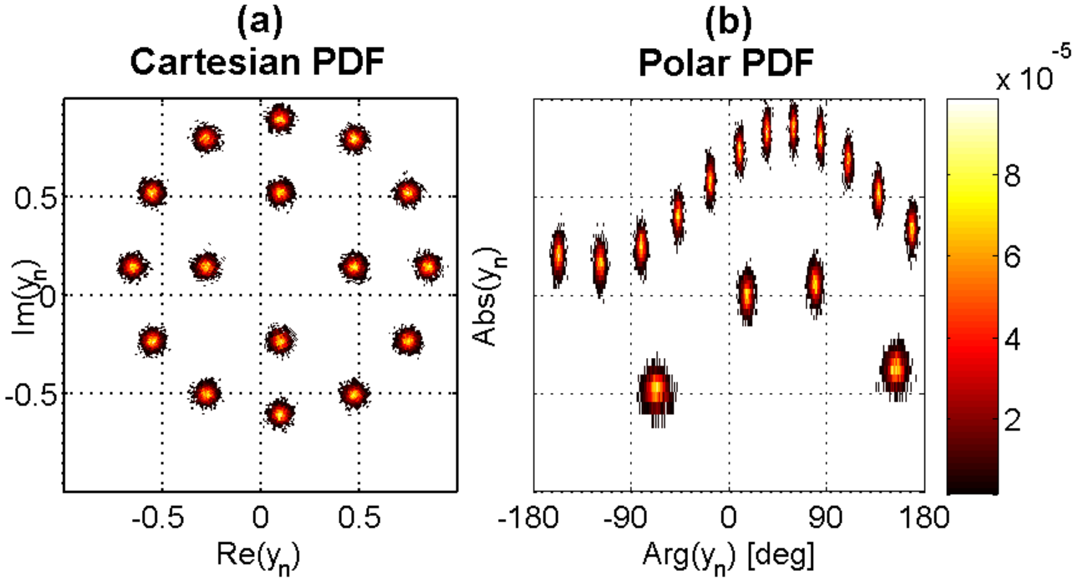

Figure 3.6: Received 12-4-A-PSK signal pdfs showing DCO effects. (a) C-CP. (b) P-CP.

I-Q Unbalance (IQU)

The detrimental effect of IQU is caused by the non symmetric behaviour of the mixers in the I and Q channels. The transmitted signals $\hat{x}^{(I)}(t)$ and $\hat{x}^{(Q)}(t)$ are up-converted in the respective RF components $x^(I)(t)$ and $x^(Q)(t)$ by the mixers. The mixers multiply the received signals with two orthogonal bases, namely $A\sin(2\pi f_0 t)$ and $-A\cos(2\pi f_0 t)$, in order to generate orthogonal I and Q RF components

$$\begin{aligned} x_n^{(I)} &= A\hat{x}^{(I)}(t)\sin(2\pi f_0 t)\,, \\ x_n^{(Q)} &= -A\hat{x}^{(Q)}(t)\cos(2\pi f_0 t)\,, \end{aligned} \tag{3.10}$$

where f_0 is the central frequency of the transmission and A is an multiplication factor.

IQU Hardware Causes

The impairing effect caused by mixers is generated by the asymmetric pre multiplication factors that affect its input signals causing imbalanced received samples, $y_{IQU,n}^{(I)}$ and $y_{IQU,n}^{(Q)}$ w.r.t. ideal ones $y_n^{(I)}$ and $y_n^{(Q)}$.

$$\begin{aligned} y_{IQU,n}^{(I)} &= A_{IQU}^{(I)} y_n^{(I)}\,, \\ y_{IQU,n}^{(Q)} &= A_{IQU}^{(Q)} y_n^{(Q)}\,, \end{aligned} \tag{3.11}$$

where $A_{IQU}^{(I)}$ and $A_{IQU}^{(Q)}$ are the mixer multiplication factors for I and Q channels, respectively.

IQU Effects on Constellations

The asymmetry introduced by IQU affects the pdf of the received signal $y_{IQU,n} = A_{IQU}^{(I)} y_n^{(I)} + jA_{IQU}^{(Q)} y_n^{(Q)}$

$$f_{IQU}(y_{IQU,n}) = \frac{1}{M}\sum_{m=1}^{M} f_{\mathcal{N}_2}\left(y_{\text{IQU},n}, \mathbf{A}\begin{bmatrix}\mathcal{R}(a^{(m)})\\ \mathcal{I}(a^{(m)})\end{bmatrix}, \sigma_w^2\mathbb{I}_2,\right)\,, \tag{3.12}$$

where,

$$\mathbf{A} = \begin{bmatrix} A_I & 0 \\ 0 & A_Q \end{bmatrix}\,. \tag{3.13}$$

where the matrix $\mathbf{A}$ affects the pdf un-uniformly stretching its dominion as depicted in Fig. 3.7 and Fig. 3.8.

The IQU impaired pdf expressed in (3.12) is depicted in Fig. 3.7 and Fig. 3.8 for a 16-QAM and a 12-4-A-PSK numerical constellation, respectively. Both pdfs patterns of (3.12) generated by QAM and A-PSK show different geometric behaviours w.r.t. the ideal ones and the DCO affected ones. In particular because of the un-uniform factor scaling of Cartesian axes the C-CP symmetries holds true but are not identical between

x and y axes. However, periodicities are different in the P-CP for both A-PSK and QAM transmitted constellations w.r.t. the ideal case.

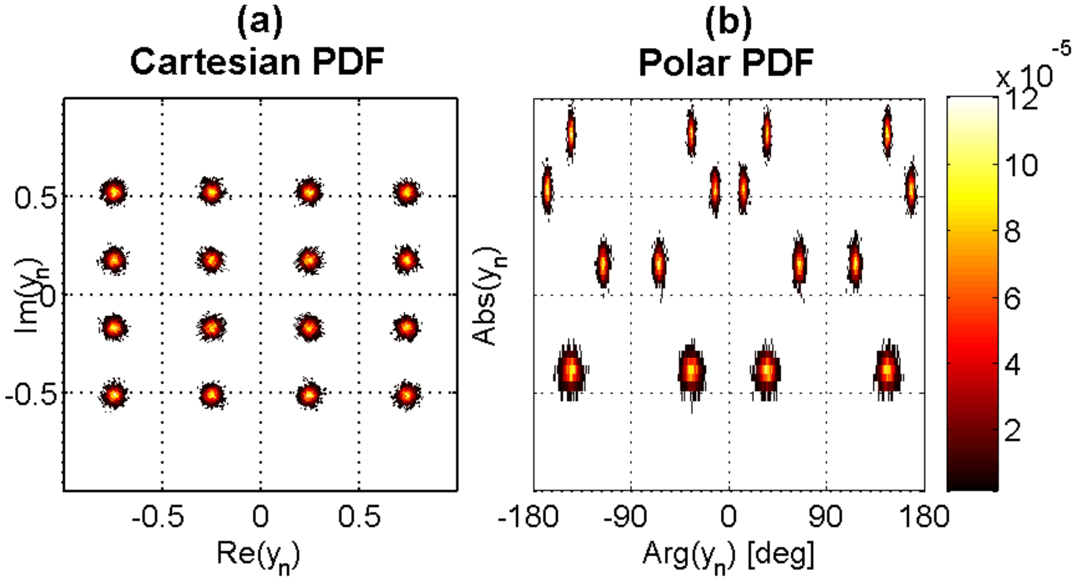

Figure 3.7: Received 16-QAM signal pdfs showing IQU effects. (a) C-CP. (b) P-CP.

I-Q Skew (IQS)

The IQS impairment is caused by the impaired hardware component that is used to feed both channel mixers with orthogonal signals. The mixers are fed by two orthogonal sinusoidal waves, as introduced in (3.14). The orthogonality of the signals that feed the mixers is crucial to generate correctly I and Q orthogonal components.

IQS Hardware Causes

The IQS causes a phase anomaly in the signals that feed the mixers, in particular their phase, that is ideally 0, is distorted causing the non orthogonality of the sinusoidal bases

$$\begin{aligned} x^{(I)}_{IQS}(t) &= A\hat{x}^{(I)}\sin(2\pi f_0 t + \alpha^{(I)}_{IQS})\,, \\ x^{(Q)}_{IQS}(t) &= -A\hat{x}^{(Q)}\cos(2\pi f_0 t + \alpha^{(Q)}_{IQS})\,, \end{aligned} \tag{3.14}$$

where $\alpha^{(I)}_{IQS}$ and $\alpha^{(Q)}_{IQS}$ are the impairing phases of the sinusoidal signals that feed I and Q channel mixers, respectively. That phase imbalance causes a intermodulation between I

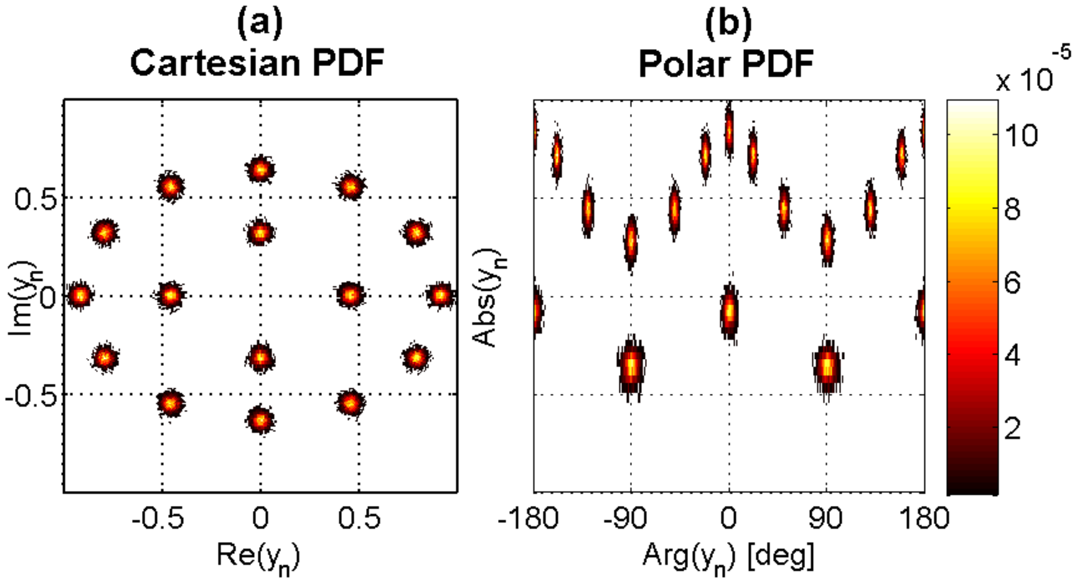

Figure 3.8: Received 8-4-A-PSK signal pdfs showing IQU effects. (a) C-CP. (b) P-CP.

and Q received channel symbols $y^{(I)}_{IQS,n}$ and $y^{(Q)}_{IQS,n}$ w.r.t. the ideal ones $y^{(I)}_{IQS,n}$ and $y^{(Q)}_{IQS,n}$, in particular

$$\begin{aligned} y^{(I)}_{IQS,n} &= y^{(I)}_n \cos(\alpha^{(I)}_{IQS}) - y^{(Q)}_n \sin(\alpha^{(Q)}_{IQS})\,, \\ y^{(Q)}_{IQS,n} &= y^{(I)}_n \sin(\alpha^{(I)}_{IQS}) - y^{(Q)}_n \cos(\alpha^{(Q)}_{IQS})\,, \end{aligned} \tag{3.15}$$

If $\alpha^{(I)}_{IQS} = \alpha^{(Q)}_{IQS} = 0$ the expressions in (3.15) becomes the ideal case in (3.10).

IQS Effects on Constellations

The phase asymmetry introduced by IQS affects the pdf of received samples $y_{IQS,n} = y^{(I)}_{IQS,n} + jy^{(Q)}_{IQS,n}$

$$f_{IQS}(y_{IQS,n}) = \frac{1}{M}\sum_{m=1}^{M} f_{\mathcal{N}_2}\left(y_{\mathrm{IQS},n}, \mathbf{S}\begin{bmatrix}\mathcal{R}(a^{(m)})\\ \mathcal{I}(a^{(m)})\end{bmatrix}, \sigma^2_w \mathbb{I}_2,\right)\,, \tag{3.16}$$

where,

$$\mathbf{S} = \begin{bmatrix}\cos(\alpha^{(I)}_{IQS}) & -\sin(\alpha^{(Q)}_{IQS})\\ \sin(\alpha^{(I)}_{IQS}) & -\cos(\alpha^{(Q)}_{IQS})\end{bmatrix}\,. \tag{3.17}$$

where the matrix **S** affects the pdf rotating un-uniformly its dominion as depicted in Fig. 3.9 and Fig. 3.10.

The IQS impaired pdf expressed in (3.16) is depicted in Fig. 3.9 and Fig. 3.10 for a

16-QAM and a 12-4-A-PSK numerical constellation, respectively. Both pdfs patterns of (3.16) generated by QAM and A-PSK show different geometric behaviours w.r.t. the ideal ones, similarly to IQU.

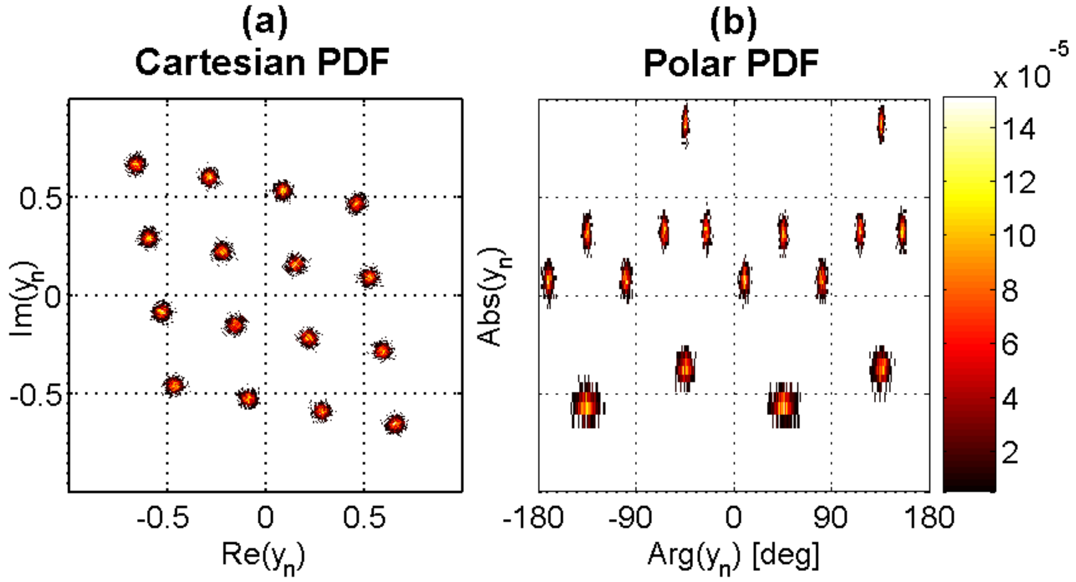

Figure 3.9: Received 16-QAM signal pdfs showing IQS effects. (a) C-CP. (b) P-CP.

Phase Offset (PO)

The PO impairment is caused by a phase misalignment between transmitter and receiver w.r.t. the ideal scenario where both sides of the communication model are synchronized. The PO can be considered a system impairment more than a hardware impairment.

PO Hardware Causes

The PO impairment can be generated by two different causes, the phase difference between the transmitting and the receiving mixers and the phase misalignment caused by the unknown distance Line of Sight (LOS) path between transmitter and receiver. Both cases can be modelled with a transmitting mixer with a non-zero phase. Impaired signals are

$$\begin{aligned} x_{PO}^{(I)}(t) &= A\hat{x}^{(I)}(t)\sin(2\pi f_0 t + \alpha_{PO}), \\ x_{PO}^{(Q)}(t) &= -A\hat{x}^{(Q)}(t)\cos(2\pi f_0 t + \alpha_{PO}), \end{aligned} \tag{3.18}$$

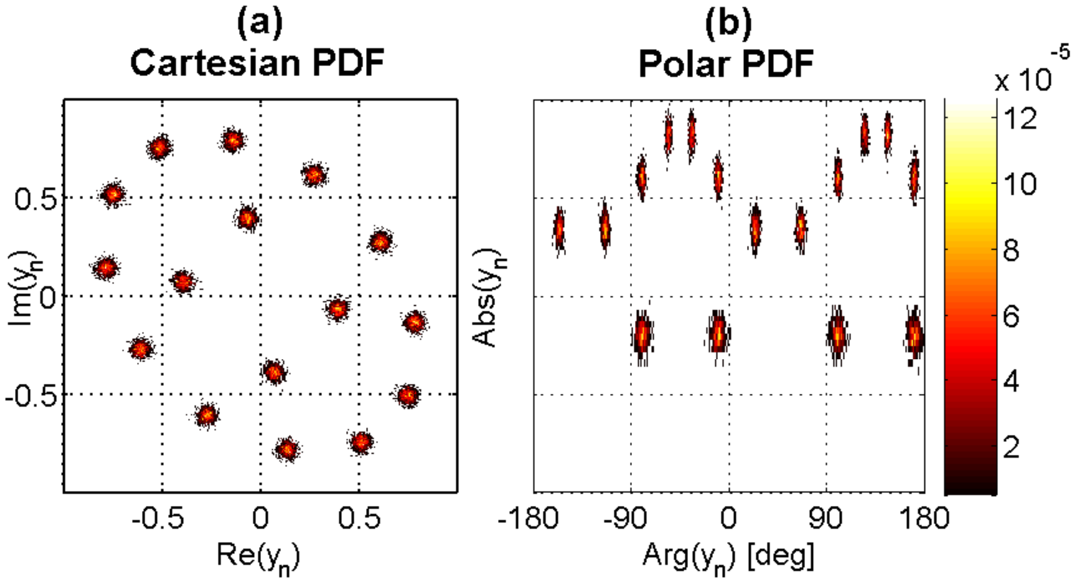

Figure 3.10: Received 8-4-A-PSK signal pdfs showing IQS effects. (a) C-CP. (b) P-CP.

where $\alpha_{PO})$ is the common impairing phase of the sinusoidal signals that feed booth I and Q channels. That constant phase causes an intermodulation between I and Q receiving channels, in particular

$$x_{PO}(t) = x(t)e^{j\alpha_{PO}} . \tag{3.19}$$

If $\alpha_{PO} = 0$, the expressions in (3.19) becomes the ideal case (3.10).

PO Effects on Constellations

The phase misalignment introduced by the PO affects the pdf of received samples, $y^{PO,n}$:

$$f_{PO}(y_{PO,n}) = \frac{1}{M}\sum_{m=1}^{M} f_{\mathcal{N}_2}\left(y_{\mathrm{PO},n}, \mathbf{R}\begin{bmatrix}\mathcal{R}(a^{(m)})\\ \mathcal{I}(a^{(m)})\end{bmatrix}, \sigma_w^2\mathbb{I}_2,\right) , \tag{3.20}$$

where,

$$\mathbf{R} = \begin{bmatrix}\cos(\alpha_{PO}) & -\sin(\alpha_{PO})\\ \sin(\alpha_{PO}) & -\cos(\alpha_{PO})\end{bmatrix} . \tag{3.21}$$

where the matrix $\mathbf{R}$ affects the pdf rotating its domain as depicted in Fig. 3.11 and Fig. 3.12.

The PO impaired pdf expressed in (3.20) is depicted in Fig. 3.11 and Fig. 3.12 for a 16-QAM and a 12-4-A-PSK numerical constellation, respectively. Both pdfs patterns of (3.20) generated by QAM and A-PSK show different geometric behaviours w.r.t. the ideal ones. In particular Cartesian symmetries are not present any more while the phase symmetries are still present but are shifted in the phase circular domain.

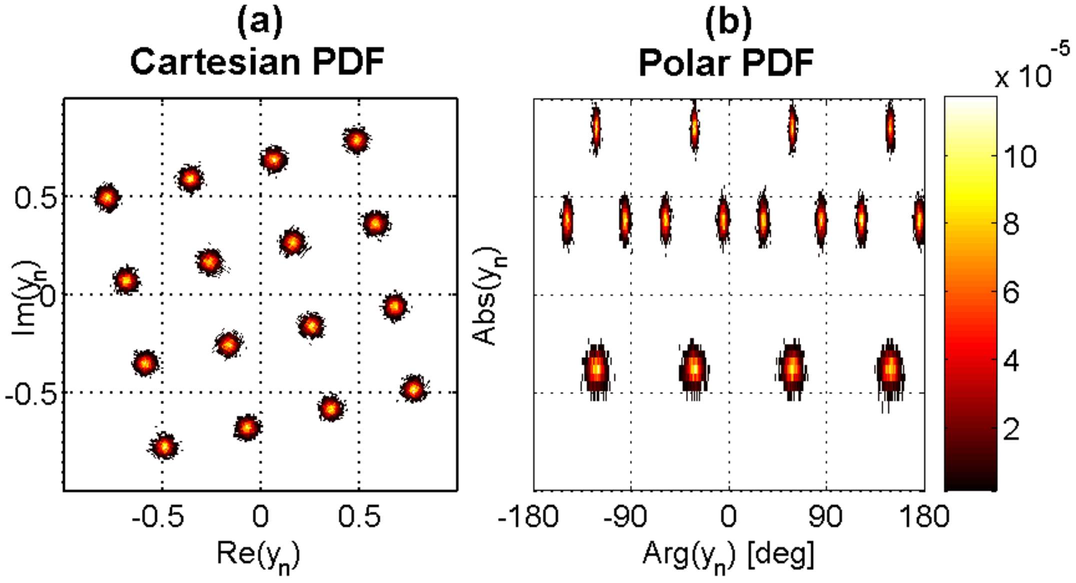

Figure 3.11: Received 16-QAM signal pdfs showing PO effects. (a) C-CP. (b) P-CP.

Conclusions

In this Ch. the effects on received signals samples statistics of transmitter hardware impairments such as DCO, PO, IQU and IQS have been discussed. The pdf received signals affected by hardware impairments have been analysed and compared to the ideal counterpart. The hardware impairments of the transmitter have been discovered to generate statistical effects on received signals that will be interpreted in Ch. 5 such as an hardware fingerprints in AoA discovery.

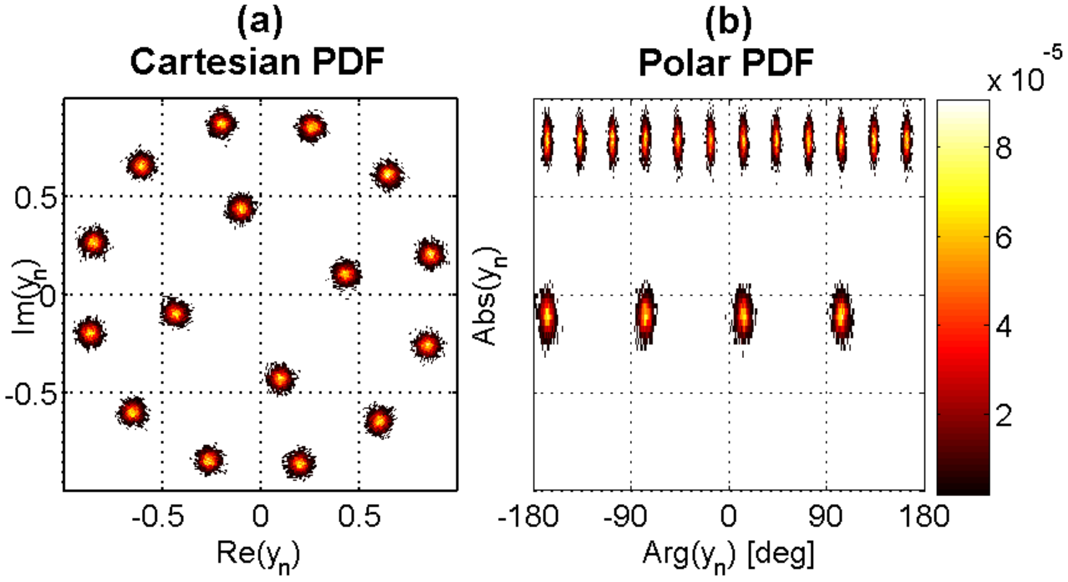

Figure 3.12: Received 8-4-A-PSK signal pdfs showing PO effects. (a) C-CP. (b) P-CP.

Multipath on AoA Estimation

4

In this Ch. the detrimental effects of Multi-path (MP) [82–84] on the AoA estimation process are analysed. Firstly, a specific geometric MP model for the antenna array system that enables the AoA estimation is assumed, it is introduced and discussed in Sec. 4.2, 4.3. Secondarily, an algorithm to emulate the considered MP model for all the receiving array with the purpose to evaluate the performance of AoA estimation algorithms is proposed in Sec. 4.4. Finally the effects of MP on the pdfs of received signals is treated in Sec. 4.5 and analysed in the AoA estimation point of view.

Introduction

A radio-localization system consisting in N_a receiving antennas, 1 transmitting antenna and N_p impairing scatterers that reflects the radio waves impairing the LOS component of the transmission is considered [4, 9]. A receiving array constituted by N_a sensors positioned in $[x_{n_a}^{RX}, y_{n_a}^{RX}]\, \forall n_a \in [1, 2, \ldots, N_a]$ is used to estimate the transmitter AoA w.r.t. the center of the array. All elements of the receiving array are located in the area limited by the sphere centred in $[0, 0]$ and with diameter $d_{\max}$, so that the maximum possible distance between a couple of sensors is $d_{\max}$. The antenna positions are arbitrary and can follow the most common L-shape [23] or others geometries, such as circular arrays [24], arbitrary shapes [25] of optimized ones [26, 27]. The transmitting antenna, that is located in $P_0 = [r_0^{(0)}, \theta_0^{(0)}]$, using polar coordinates, and in $[x_0, y_0]$, using cartesian ones, emits a narrowband signal with wave-length λ_0. The transmitter is located in the far field area w.r.t. the center of the array and the wavelength: its distance is $r_0^{(0)} >> \lambda_0$ and $r_0^{(0)} >> d_{max}$. The value of θ_0 expresses the AoA that has to be estimated by signals impinging in the receiving array. Differently from the ideal LOS case N_p scatterers are present in the model [85, 86]. Scatterer n_p is located in $P_{n_p} = [r_{n_p}^{(0)}, \theta_{n_p}^{(0)}]$, using polar coordinates, in $[x_{n_p}, y_{n_p}]$, using cartesian ones. The scatterers are located in the far field area w.r.t. the center of the array and the wavelength: their distance is $r_{n_p}^{(0)} >> \lambda_0$ and

$r_{n_p}^{(0)} >> d_{max}$ [85] In Sec. 4.2 a Uniformly Sampled Channel Impulse Response (CIR) (US-CIR), that is a CIR constituted by equally spaced impulses [83, 84], will be used to represent the channel of the radio scattering model above. The geometric characteristics of US-CIR [87, 88] will be analysed to test its applicability in real scenarios. The US-CIR model will be then used in 4.3 to verify the relations between the CIRs of all N_a array sensors w.r.t. the transmitter. In Sec. 4.4 a practical algorithm to easily generate a geometrically meaningful CIRs for all the array sensors starting from a main CIR is developed. Finally, in Sec. 4.5 the relation between the pdf of received QAM signals and the position of the channel scatterers is investigated in an AoA estimation point of view.

US-CIR based Scattering Geometric Model (U-SGM)

The CIR generated by scatterers involving the signals emitted by the transmitting antenna and impinging in the the nominal center P_0 of a generic array, namely $h^{(0)}(t)$, is herein considered. For the sake of simplicity the center of the array is considered the center of the axis. The considered CIR is a US-CIR and its absolute value is depicted in Fig. 4.1. Its analytic expression is characterized by $N_p + 1$ impulses uniformly spaced by T_p:

$$h^{(0)}(t) = \sum_{n_p=0}^{N_p} h_{n_p}^{(0)} \delta(t - \tau_{n_p}^{(0)}) \,, \tag{4.1}$$

where $\delta(t)$ is the Dirac impulse in the continuous time domain and where the characteristics of the impulses are

$$\begin{aligned} \tau_{n_p}^{(0)} &= \tau_0^{(0)} + n_p T_p \,, \\ |h_{n_p}^{(0)}| &\propto e^{-\frac{r_{0n_p}^{(0)}}{r_{\text{norm}}}} \,, \\ \angle h_{n_p}^{(0)} &= e^{j2\pi \frac{r_{0n_p}^{(0)}}{\lambda_0}} \,, \end{aligned} \tag{4.2}$$

where n_p is the impulse/scatterer index and T_p their uniform inter-impulse temporal distance. The length $r_{0n_p}^{(0)}$ is the linear distance that the signal runs across to go from the transmitter to the center of the array passing from the n_p-th scattered. In particular $r_{00}^{(0)} = r_0^{(0)}$ is the LOS distance between transmitter and the center of the array. The parameter r_{norm} is a normalization distance that expresses the Path Loss (PL) and depends on propagation condition [89]. The CIR $h^{(0)}(t)$ considered in Fig. 4.1 is constituted by $N_p + 1$ impulses where the first one ($n_p = 0$) represents the LOS component and the others N_p are caused by the N_p scatterers considered in the model. The impulses of the US-CIR are T_p-spaced. The assumption that the repetitions of the transmitted signals at the receiver caused by scatterers are generated only by a first reflection is made. Multiple reflection between different scatterers are than considered neglectable likewise the model in [87]. Each impulse express the effect of one, and only one, reflection caused by a single

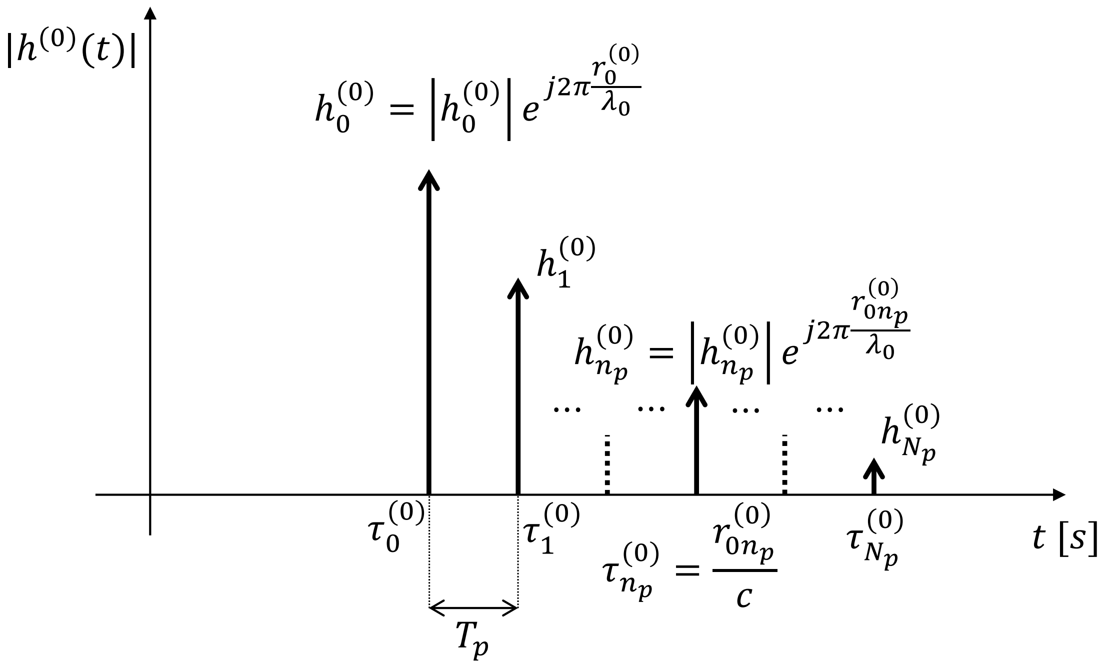

Figure 4.1: CIR of a signal emitted by transmitter antenna and received in the center of the receiving array.

scatterer. The first impulse is temporary located in $\tau_0^{(0)} = r_0^{(0)}/c_0$ and represents the LOS component. The scatterers impulses are located in $\tau_{0n_p}^{(0)} = \tau_0^{(0)} + n_p T_p$ where n_p is the scatterer index. The n_p-th scatter impulse value is $h_{n_p}^{(0)} = |h_{n_p}^{(0)}| \exp{(j2\pi r_{0n_p}^{(0)}/\lambda_0)}$, is dependent only from the value of $r_{0n_p}^{(0)}$. The value of $\angle h_{n_p}^{(0)}$ depends only by the scatterer position. In Fig. 4.2 is depicted the geometric scattering model for one scatterer ($N_p = 1$) of the US-CIR in (4.1), that is the geometrical interpretation of the n_p-th impulse of the CIR in Fig. 4.1 [86, 88]. The distances in Fig. 4.2 follow the geometric rule

$$r_{0n_p}^{(0)} = r_{0n_p} + r_{n_p}^{(0)} \,, \tag{4.3}$$

where $r_{0n_p}^{(0)} = c_0 \tau_{0n_p}^{(0)}$ is the full length of the path of the signal reflected by the n_p-th scatterer (see Fig. 4.2). The parameter $r_{0n_p}^2 = (x_{n_p} - x_0)^2 + (y_{n_p} - y_0^2)$ is the euclidean distance between the n_p-th scatterer and the transmitter that is located in $P_0 = [x_0, y_0]$. The parameter $(r_{n_p}^{(0)})^2 = (x_{n_p}^{(0)})^2 + (y_{n_p}^{(0)})^2$ is the euclidean distance between the n_p-th scatterer and the center of the axis. The expression in (4.3) represents an ellipse with the first focus $F_0 = [0, 0]$ located in the center of the array and the other focus P_0 positioned in the transmitter coordinates. The major axis of the ellipse lies in the line that connects the transmitter and the array center. The ellipse in (4.3) can be represented symbolically as $r_{0n_p}^{(0)} = \overline{P_0 P_{n_p}} + \overline{F_0 P_{n_p}}$ where the operator $\overline{AB}$ expresses the euclidean distance between the point A and the point B. The value of the major axis of the ellipse is proportional to $n_p T_p$ and implies that the each one of the N_p scatterers is arbitrary positioned in one of the N_p equispaced concentric ellipses. Where concentric ellipses means ellipses with the

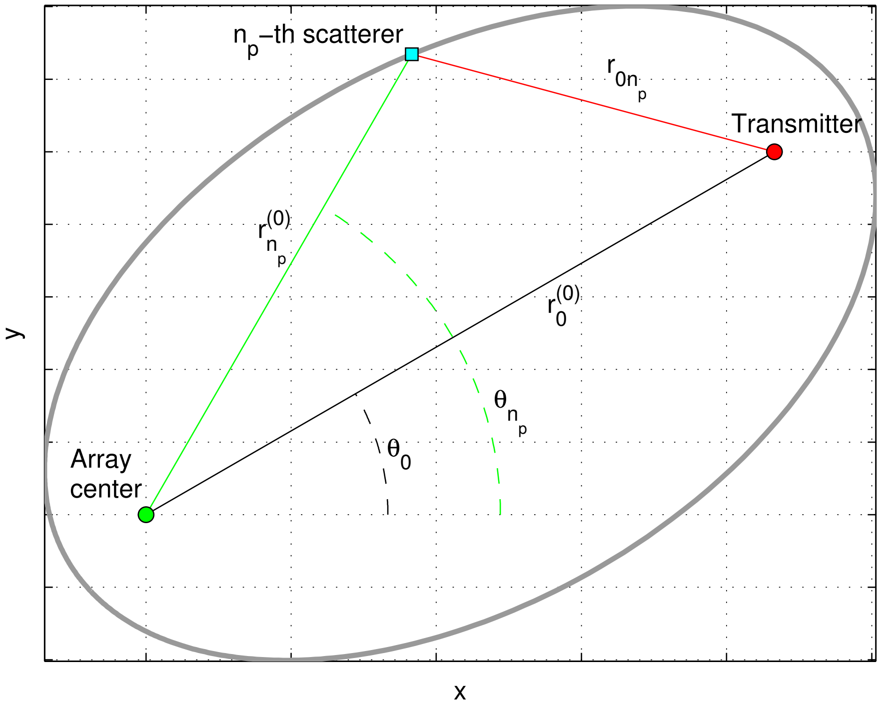

Figure 4.2: Scattering ellipse n_p, representing the possible positions for the n_p-th scatterer related to the CIR model in Fig. 4.1. θ_{n_p} represents the AoA of the n_p scatterer.

same focuses but different major axis length.

Concluding, the generic n_p-th impulse represented in Fig. 4.1 and expressed by (4.3) is geometrically caused by a scatterer positioned in the n_p scattering ellipse (4.3) depicted in Fig. 4.2 for any value of the scatterer AoA θ_{n_p}.

The position of the transmitter in Fig. 4.1 does not respect the condition $r_0^{(0)} >> d_{\max}$ introduced in Sec. 4.1 to better illustrate the system elements. The angle θ_0 expresses the transmitter AoA that have to be estimated. The angle θ_{n_p} instead indicates the AoA of the delayed signal replica reflected from the n_p-th scatterer.

The more T_p is small and the more the number of scatterers N_p is large, the more all the scatterers ellipses can cover the 2D cartesian space. Furthermore, only a subset of $N_p'l \leq N_p$ scatterers can be used in the U-SGM model forcing others to $|h_{n_p}^{(0)}| = 0$ as visible in Fig. 4.6 where $N_p' = 4$. Previous considerations show that the U-SGM is able to emulate any scatterers configuration despite its artificially time sampled impulses.

Antenna Array's CIRs in U-SGM Scenario

In Sec. 4.2 the CIR w.r.t. the center of an arbitrary complex array is considered. That CIR was assumed US-CIR by definition of the scattering model. In the following the CIRs $h^{(n_a)}(t)$ of the channel between the transmitter and a generic antenna n_a of the array is analysed. Impulses of $h^{(0)}(t)$ in Fig. 4.1 are equispaced of T_p by definition (US-CIR). Differently the CIRs $h^{(n_a)}(t)$ are composed, in general, by randomly spaced impulses (see Fig. 4.3) because of the different positions of the antennas w.r.t. the center of the array. Its expression is

$$h^{(n_a)}(t) = \sum_{n_p=0}^{N_p} h_{n_p}^{(n_a)} \delta(t - \tau_{n_p}^{(n_a)}), \tag{4.4}$$

where n_a is the antenna index an where

$$\begin{aligned} &\tau_{n_p-1}^{(n_a)} - \tau_{n_p}^{(n_a)} \neq T_p \,, \\ &|h_{n_p}^{(n_a)}| \propto e^{-\frac{r_{0n_p}^{(n_a)}}{r_{\text{norm}}}} \,, \\ &\angle h_{n_p}^{(n_a)} = e^{j2\pi \frac{r_{0n_p}^{(n_a)}}{\lambda_0}} \,, \end{aligned} \tag{4.5}$$

where n_p is the impulse index and $r_{0n_p}^{(n_a)}$ is the full length of the path of the transmitted signal reflected by the n_p-th scatterer and impinging in the n_a array sensor. The n_p-th impulse represented in Fig. 4.3 and analytically described in (4.5) is geometrically obtainable with a scatterer positioned in the ellipse depicted in Fig. 4.4. A two elements receiving array is depicted in Fig. 4.4 for the sake of the example and to enhance the differences w.r.t. the CIR in Fig. 4.1. The position of the transmitter in Fig. 4.4 does not respect the condition $r_0^{(0)} >> d_{\max}$ introduced in Sec. 4.1 to better illustrate the system elements.

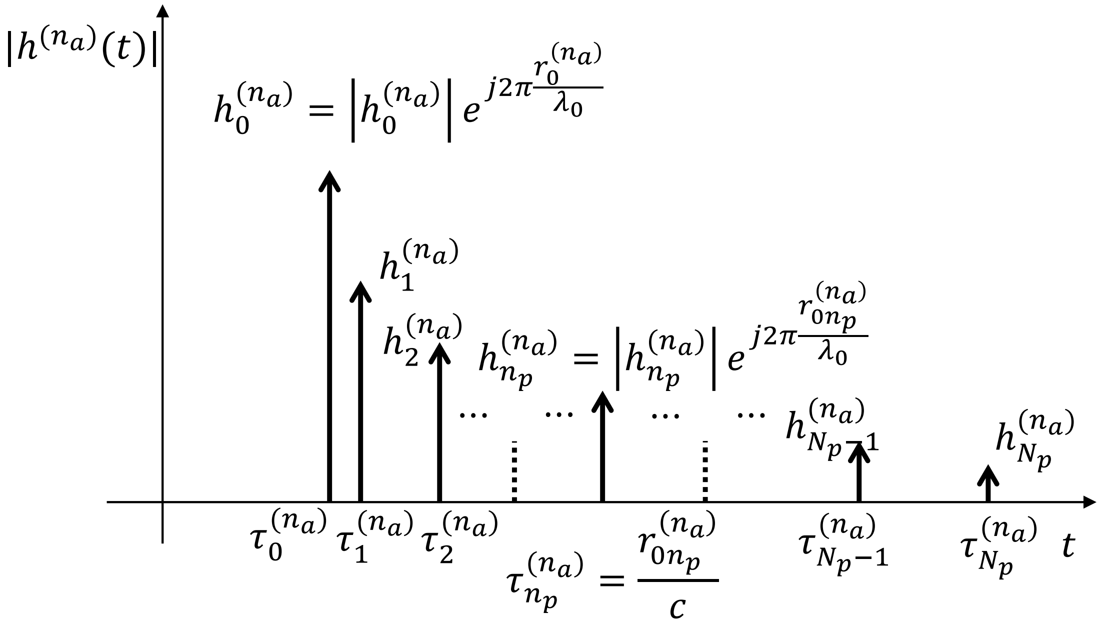

Figure 4.3: CIR of a signal emitted by transmitter antenna and received by the n_a-th sensor of the antenna array.

In Sec. 4.4 are discussed the assumption made and the techniques used to represent the generic antenna sensor CIR $h^{(n_a)}(t)$ using the array US-CIR $h^{(0)}(t)$.

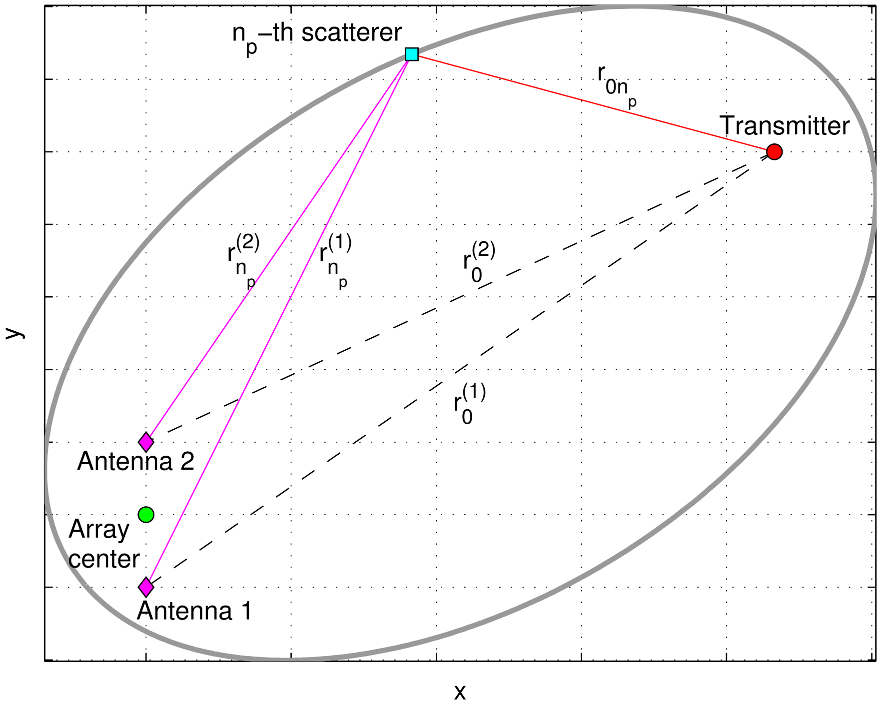

Figure 4.4: Ellipse representing the possible positions of the n_p-th scatterer related to the CIR model in Fig. 4.3. A two elements ULA is depicted.

Antenna Array's CIRs Statistical Generation in U-SGM Scenario

To evaluate performances of different AoA estimation algorithms with a simulative approach it is necessary to statistically generate the CIRs for the system introduced in Ch. 4.1. In the following the array US-CIR valid for the center of the array, described in Sec. 4.2, is used as a base to randomly generate geometrically reasonable CIRs $h^{(n_a)}(t)$ for each antenna of the array.

Three sets of parameters are needed to generate a the generic CIR for the antenna n_a composed by N_p scatterers and the LOS component:

- $N_p + 1$ amplitudes $|h^{(n_a)}_{n_p}|$,
- $N_p + 1$ phases $\angle h^{(n_a)}_{n_p}$,
- $N_p + 1$ ToAs $\tau^{(n_a)}_{n_p}$.

In the following Sec. is showed how these parameters are related to each other and to the positions of the scatterers P_{n_a} and the transmitter P_0.

CIR Amplitudes Generation

Considering the far field assumption $r_0^{(0)} >> d_{max}$ w.r.t. the array area, it is possible to reasonably approximate the CIR impulses amplitudes in 4.5 as

$$\rho_{n_p} := |h_{n_p}^{(n_a)}| \approx |h_{n_p}^{(0)}| \propto e^{-\frac{r_{0n_p}^{(0)}}{r_{\text{norm}}}} \quad \forall n_a \in [1, 2, \ldots, N_a], , \tag{4.6}$$

assuming the amplitude of each scatterer reflection identical to ρ_{n_p} for every antenna. The LOS component amplitude is included in the approximation in (4.5). A similar approximation about the PL component is made in the Rice channel modelling [90, 91].

CIR Phases Generation

The phase of the delayed reflected signal coming from the n_p-th scatterer of the system is related to its AoA θ_{n_p} like the LOS component is related the main AoA θ_0 (2.13). Scatterers impulses phases at different antennas are not approximated as identical such as their PLs [90, 91]. The phase of CIR impulses in 4.5 can be then obtained using the n_p-th scatterer AoA θ_{n_p} and antennas positions $[x_{n_a}^{RX}, y_{n_a}^{RX}]$, similarly to 2.13, as following:

$$\begin{aligned} \alpha_{n_p}^{(n_a+1)} &:= \angle h_{n_p}^{(n_a+1)} = \alpha_{n_p}^{(n_a)} + \Delta\alpha_{n_p}^{(n_a+1)}, \\ \Delta\alpha_{n_p}^{(n_a+1)} &= 2\pi \frac{d^{(n_a+1)}}{\lambda_0} \sin\left(\theta_{n_p} + \delta\theta^{(n_a+1)}\right), \end{aligned} \tag{4.7}$$

where $\alpha_{n_p}^{(n_a)}$ is defined as the PoA of the n_p-th scatterer reflection at the n_a-th antenna, $\angle h_{n_p}^{(n_a)}$. The parameter $\Delta\alpha_{n_p}^{(n_a+1)}$ represents instead the D-PoA between n_a+1-th and n_a-th antennas regarding the the n_p-th scatterer reflection. The indexing $n_p = 0$ represents the LOS component. The angle $\delta\theta^{(n_a+1)}$ is the inclination angle of the antenna couple n_a - n_a+1 w.r.t. the y axis introduced in (2.3). The distance value $d^{(n_a+1)}$ is the inter element distance of the antenna couple n_a - n_a+1. The angle θ_{n_p} is the AoA of the of the n_p-th scatterer reflection, with θ_0 indicating the radio source LOS AoA. The expression in (4.7) is obtained applying (2.13) to the n_p scatterer. It is important to notice how the parameter $\Delta\alpha_{n_p}^{(n_a+1)}$ is dependent only by scatterers AoAs θ_{n_p} and the antenna couple orientation and distance, namely $\delta\theta^{(n_a+1)}$ and d^{n_a+1}. For the sake of the example in Fig. 4.4 is depicted a 2 elements ULA along the y axis that yields to a value of $\delta\theta^{(2)} = 0$ between antenna 1 and 2. The expression in (4.7) for the n_p-th scatterer implies that the n_a+1-th antenna CIR impulses phases are generated differentially from previous antenna values. For this reason, for each scatterer n_p, the value of $\alpha_{n_p}^{(1)}$ must be defined previously to determine all the remaining $N_a - 1$ phases from $\alpha_{n_p}^{(2)}$ to $\alpha_{n_p}^{(N_a)}$. The values of $\alpha_{n_p}^{(1)}$ are generated randomly as $U(0, 2\pi)$ [91], where $U(0, 2\pi)$ is the Uniform random distribution between 0 and 2π. The values of the AoAs θ_{n_a} of the N_p spurious scatterers can be generated randomly as

$U(0, 2\pi)$ to obtain $\Delta\alpha_{n_p}^{(n_a+1)}$ using (4.7) and the array geometry defined by $\delta\theta^{(n_a+1)}$ and d^{n_a+1}.

CIR ToAs generation

The third set of parameters needed to randomly generate $h^{(n_a)}(t)$ is composed by the ToAs, comprising the LOS ToA $\tau_0^{(n_a)}$ and the scatterers ToAs $\tau_{n_p}^{(n_a)}$. A scenario where the transmitter is far from the whole array w.r.t. the array size ($r_0^{(0)} >> d_{max}$) is considered. Scatterers are assumed to be far from the array w.r.t. its size d_{max}: $r_{n_a}^{(0)} >> d_{max}$. It is then reasonable to approximate the $N_p + 1$ CIR impulses ToAs identical for all antennas, where a similar conclusion is made in the reasoning made for Rayleigh channel definition [91].

$$\tau_{n_p} := \tau_{n_p}^{(n_a)} \approx \tau_{n_p}^{(0)} = \tau_0^{(0)} + n_p T_p \,, \tag{4.8}$$

where the approximation in 4.8 considers the ToA τ_{n_p} of the scatterer n_p the same for each antenna n_a. The scatterers are T_p spaced for every antenna. This approximation holds only for the CIR impulses positions calculus and not for their phases as discussed in Sec. 4.4.2. The CIR impulses phases are instead generated regarding their AoAs θ_{n_p}.

The random generation of the CIRs with the approximations made in this Sec. leads to identical CIR absolute value shapes as visible in Fig. 4.5. The key difference between CIRs stands in the phase of the impulses, that carries the AoA information about the RF source LOS and the reflections as explained in (4.7). In Fig. 4.6 is depicted an example of the simulated CIRs of a 2 elements antenna array without considering the LOS component. The CIR sampling time is $T_p = T_{symb}/13$. To simulate a continuous CIR, $N_p = 61$ but only $N'_P = 4$ scatterer are effectively present in the channel. This is possible imposing $h_{n_p}^{(n_a)} = 0$ for the un-activated scatterers.

MP Effects on Numerical Modulation Constellations

The multipath scenario introduced in Sec. 4.3 is herein considered. In Ch. 3 the effects of hardware impairments in numerical constellations have been discussed, analogously in this Sec. the effects of multipath in QAM and A-PSK will be treated.

The RF signal $z^{(RF)}(t)$ impinging at the receiver's antenna is generated modulating a numeric symbol a_n with a transmitting interpolation filter $g(t)$. Impinging signal $z^{(RF)}(t)$ is then down-converted by receiver branches generating

$$y_n = y_n^{(I)} + j y_n^{(Q)} \,, \tag{4.9}$$

where $y_n^{(I)}$ and $y_n^{(Q)}$ are the signals elaborated by the I and Q branches respectively and T_s is the sampling period. In the ideal case where no impairments are considered and where

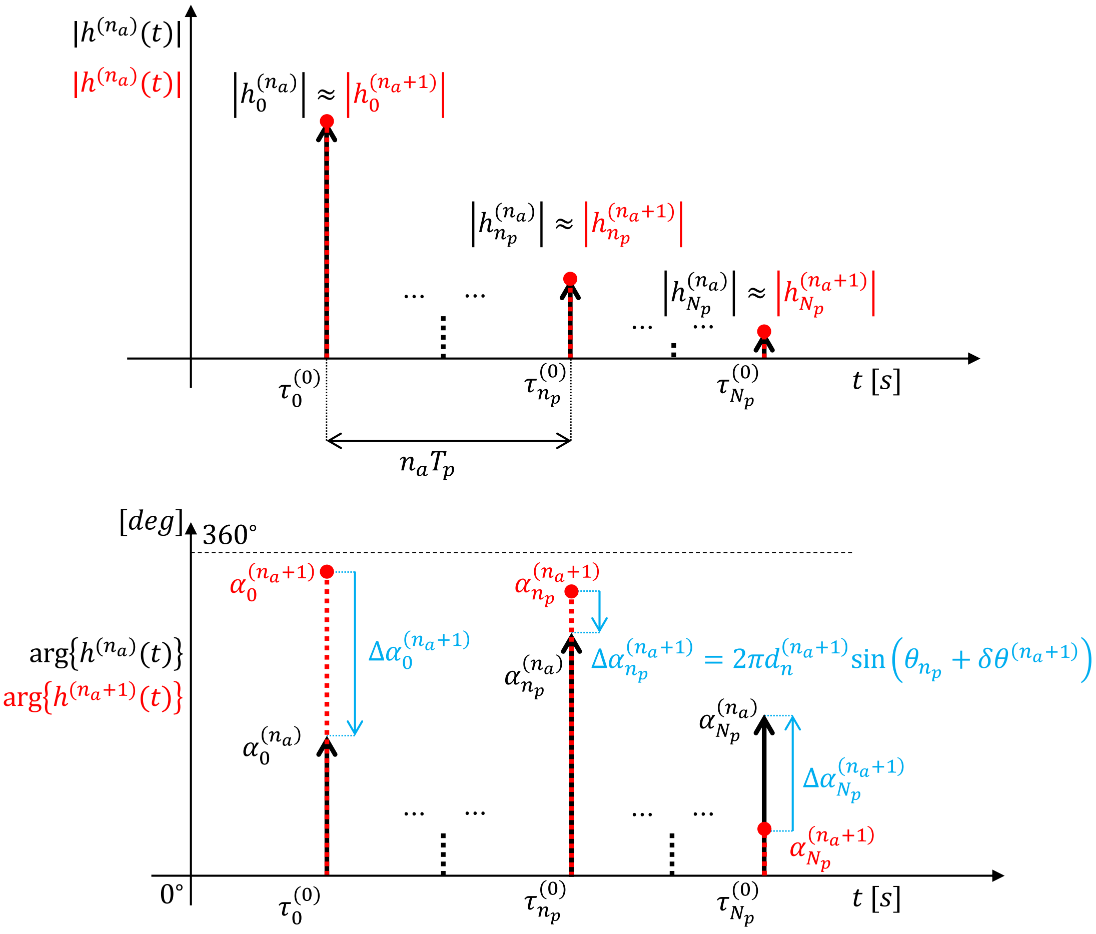

Figure 4.5: Approximated CIR of a signal emitted by transmitter antenna and received by the n_a-th and $n_a + 1$-th sensors of an antenna array.

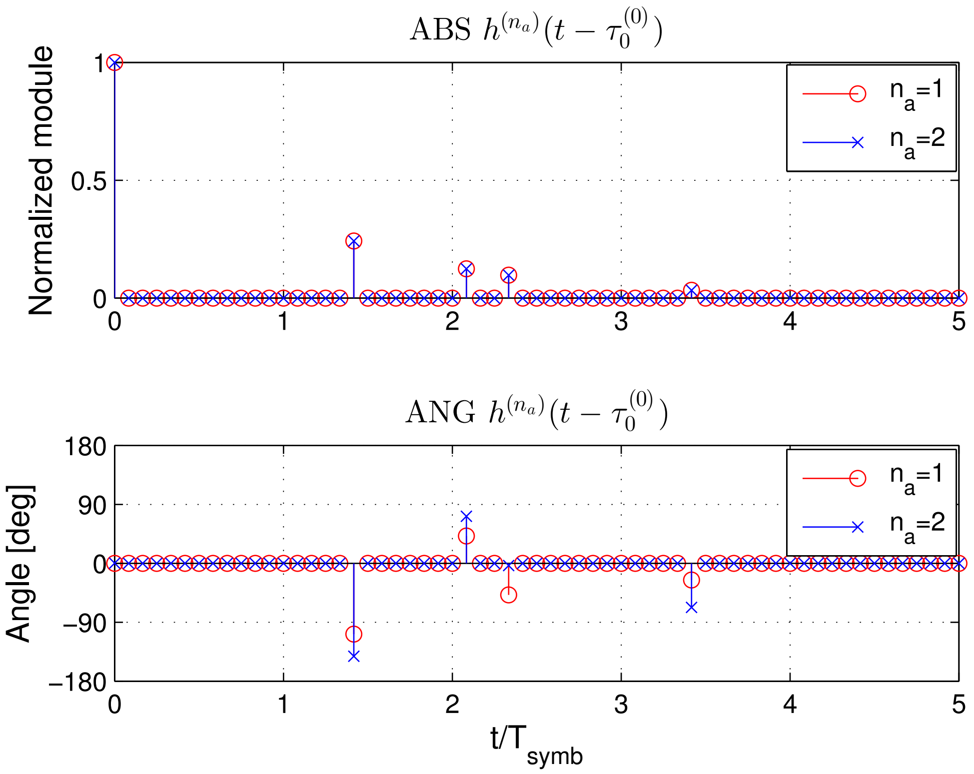

Figure 4.6: Examples of the generated CIRs for a 2 antennas receiving array. $T_s = T_{symb}/13$

receiving filter is synchronized and matched to the transmitter's one ($T_s = T_{\text{symb}}$)

$$y_n = a_n + w_n \tag{4.10}$$

where a_n is the symbol of a unitary energy M-sized numerical constellation that is transmitted by receiver with period T_{symb}. The parameter $w_n = w(n_T s) \sim \mathcal{N}(0, \sigma_w)$ is the sampled C-AWGN with zero mean and standard deviation σ_w.

Receiving Architectures Comparison

In this Sec. the receiving architecture in Fig. 4.7 is considered, where the receiving filter is a generic Low Pass Filter (LPF) and the output samples are sampled, in general, at $T_s \neq T_{\text{symb})}$. Oversampling signals at the receiver side using a LPF is used in Ch. 5 and is justified when the transmitter's parameters such as symbol period and transmitting filter are unknown. The expression in (4.10 with the receiving architecture in Fig. 4.7 becomes

$$y_n = \hat{a}_n + w_n \,, \tag{4.11}$$

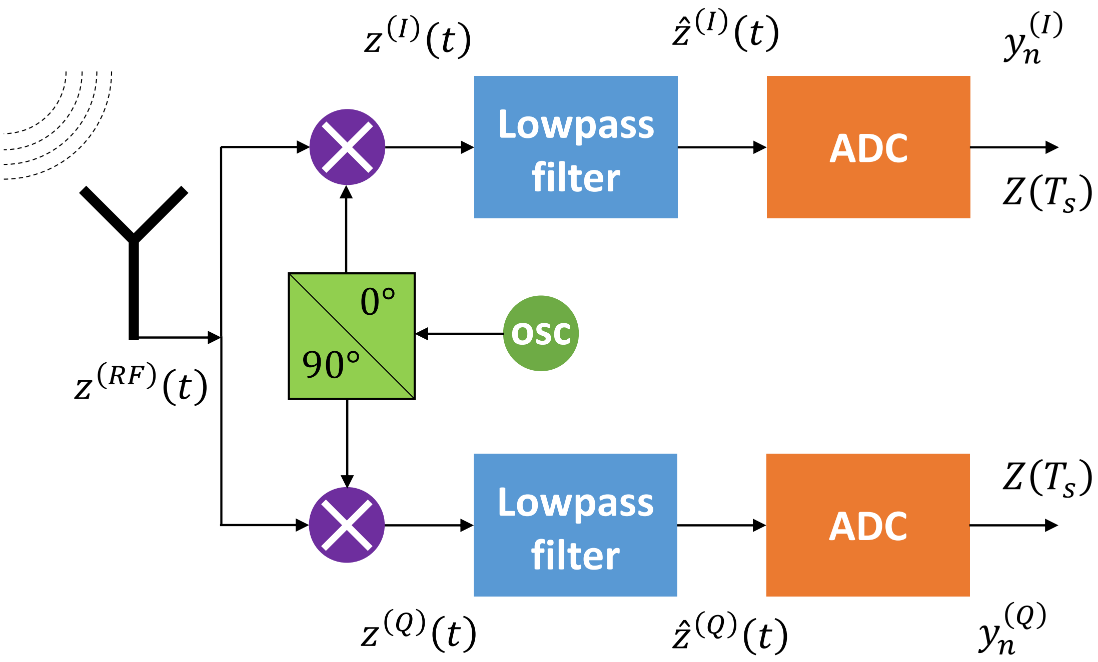

Figure 4.7: Scheme of receiver with LPF.

where $\hat{a}_n$ represents the equivalent received symbol modified by the sampling of the transmission filter $g(t)$, and where

$$\hat{a}_n = a_k\, g\Big(\mathfrak{R}(nT_s + \Delta T_s, T_{\text{symb}})\Big)\,, \tag{4.12}$$

$$nT_s = kT_{\text{symb}} + \mathfrak{R}(nT_s + \Delta T_s, T_{\text{symb}})\,, \tag{4.13}$$

$$\mathfrak{R}(nT_s, T_{\text{symb}}) = nT_s \pmod{T_{\text{symb}}}\,. \tag{4.14}$$

The operator $\mathfrak{R}(nT_s+\Delta T_s, T_{\text{symb}})$ represents the remainder of the division of $nT_s+\Delta T_s$ by T_{symb}, its value is limited by definition between 0 and T_{symb}. The parameter ΔT_s represents a sampling offset due to unsynchronized receiver and transmitter w.r.t. symbol timing, its value is limited by definition to the interval $[0, T_s[$. The index k represents the transmitted symbol index associated to the interval $[kT_{\text{symb}}, (k+1)T_{\text{symb}}[$. The transmission filter $g(t)$ is defined inside a limited domain, restricted to the symbol period $[0, T_{\text{symb}}[$.

The equivalent symbol $\hat{a}_n$ is an element of the equivalent constellation $\hat{\mathcal{A}}$ generated sampling the transmission filter $g(t)$ fed by the numerical constellation $\mathcal{A}$:

$$\begin{aligned} &\hat{\mathcal{A}} := \mathcal{A} \times \mathcal{G}(nT_s + \Delta T_s, T_{\text{symb}})\,, \\ &\mathcal{A} = \left\{a^{(m)}\right\}_{m=1,\ldots,M}\,, \\ &\mathcal{G}(nT_s + \Delta T_s, T_{symb}) = \left\{g\Big(\mathfrak{R}(nT_s + \Delta T_s, T_{\text{symb}})\Big)\right\}_{n=1,\ldots,q}\,. \end{aligned} \tag{4.15}$$

The operator $[\times]$ represents the Cartesian product between sets. Considering for the sake of the example the generic relation $\mathcal{Z} = \mathcal{X} \times \mathcal{Y}$ between the sets $\mathcal{X}$ and $\mathcal{Y}$, the cardinality of the resulting set $\mathcal{Z}$, namely $|\mathcal{Z}|$, is $|\mathcal{X}| \cdot |\mathcal{Y}|$. M is the cardinality of the transmitted constellation $\mathcal{A}$. The set $\mathcal{G}$ is constituited by all the possible samples of $g(t)$ generated by the unsynchronized receiver. The cardinality of $\mathcal{G}(nT_s + \Delta T_s, T_{\text{symb}})$ is q, where q is the smaller integer solution of

$$\begin{aligned} &qT_s = pT_{\text{symb}} \, , \\ &q, p \in \{1, 2, \dots\} \, . \end{aligned} \tag{4.16}$$

The cardinality of $\hat{\mathcal{A}}$ is then qM: $|\hat{\mathcal{A}}| = qM$. The integer p represents the minimum number of symbol periods needed to acquire the full constellation $\hat{\mathcal{A}}$.

The analytic expression of the pdf of y_n in (4.11) is

$$f(y_n) = \frac{1}{qM} \sum_{m=1}^{qM} f_{\mathcal{N}_2} \left(y_n, \begin{bmatrix} \mathcal{R}(\hat{a}^{(m)}) \\ \mathcal{I}(\hat{a}^{(m)}) \end{bmatrix}, \sigma_w^2 \mathbb{I}_2 \right) \, , \tag{4.17}$$

where $\hat{a}^{(m)}$ are symbols of $\hat{\mathcal{A}}$ and are considered equiprobable since the elements of $\mathcal{A}$ are by definition equiprobable.

In the following are discussed the effects on a transmitted 4-QAM constellation to understand the difference between previous receving architectures, namely the one that is provided by the matched filter (Fig. 3.2) and the one proposed above (Fig. 4.7).

Firstly, for the sake of the example a transmitter that emits with period T_{symb} symbols of a 4-QAM constellation is considered. Transmitter uses as transmitting filter a Root Raised Cosine (RRC) $g(t)$. The corresponding receiver down-convert and samples the received signals using a synchronized matched filter. In Fig. 4.8 is depicted the waveform of the signals involved in the I branch over time. A statistical analysis analogous to the one done in Ch. 3 about hardware impairments effects is done depicting the C-CP and the P-CP of y_n. In Fig. 4.9 are visible the 4 peaks of the pdfs of y_n if ideally received with a synchronized matched filter.

Secondarily, under the previous assumptions for the transmitter, a receiver that down-converts and samples with period $T_s < T_{\text{symb}}$ the received signals using the LPF in Fig. 4.7 is considered. In Fig. 4.10 are depicted the time shapes of the signals involved in the I branch. In Fig. 4.10 is visible how the higher sampling rate at the receiver, $T_s = T_{\text{symb}}/6$, causes the sampling of the tails of the RRC filter w.r.t. the ideal case in Fig. 4.8.

In Fig. 4.11 are depicted the C-CP and the P-CP of y_n. The higher sampling rate at the receiver, $T_s = T_{symb}/6$, w.r.t. the ideal case, generates several peaks in the pdfs of y_n. Additional peaks are caused by the samples of the tails of the RRC filter visible in Fig. 4.10. Additional acquired samples leads to additional peaks in the pdf in 4.11 that are consistent with the angular position of the normally sampled pdf in4.9. Il the following the pdfs analized in this Sec. will be analised when affected by MP.

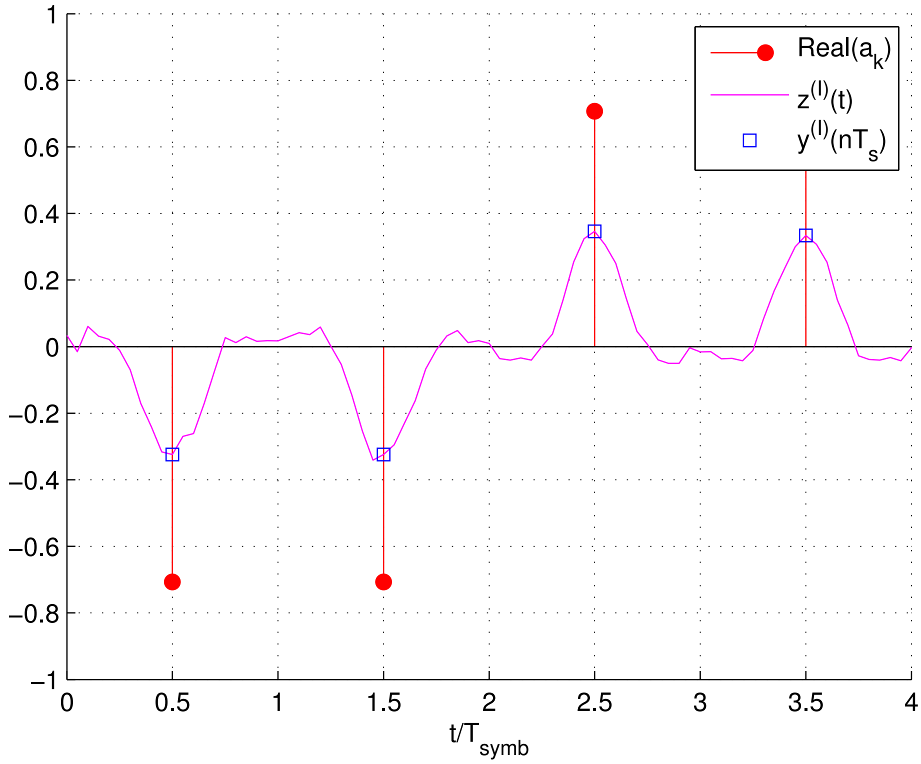

Figure 4.8: Received 4-QAM time signals at the I branch shaped by a RRC filter and received by a proper matched filter.

Applying the MP

The effects of the MP model introduced in Sec. 4.2 on numerical constellation received with the architecture in Fig. 4.7 will be now discussed. The multipath channel is described with the US-CIR

$$h^{(0)}(t) = \sum_{n_p=0}^{N_p} \underbrace{\rho_{n_p} e^{j\alpha_{n_p}^{(0)}}}_{h_{n_p}^{(0)}} \delta(t - \tau_0 - n_p T_p)\,, \tag{4.18}$$

where for the sake of simplicity the scatterers inter arrival period T_p is considered equal to the sampling period T_s. The parameter τ_0 is the ToA of the LOS component. The angle $\alpha_{n_p}^{(0)}$ represents the PoA shift caused by the n_p-th scatterer. Using the receiver in Fig. 4.7, that is provided with a LPF, the received signal y_n is

$$\begin{aligned} y_n &= \hat{a} * h^{(0)}(nT_s) + w_n\,, \\ &= \sum_{n_p=0}^{N_p} \hat{a}_{n-n_p} \rho_{n_p} e^{j\alpha_{n_p}^{(0)}} + w_n\,, \\ &= \hat{a}_n \rho_0 e^{j\alpha_0^{(0)}} + \cdots + \hat{a}_{n-n_p} \rho_{n_p} e^{j\alpha_{n_p}^{(0)}} + \cdots + \hat{a}_{n-N_p} \rho_{N_p} e^{j\alpha_{N_p}^{(0)}} + w_n\,, \end{aligned} \tag{4.19}$$

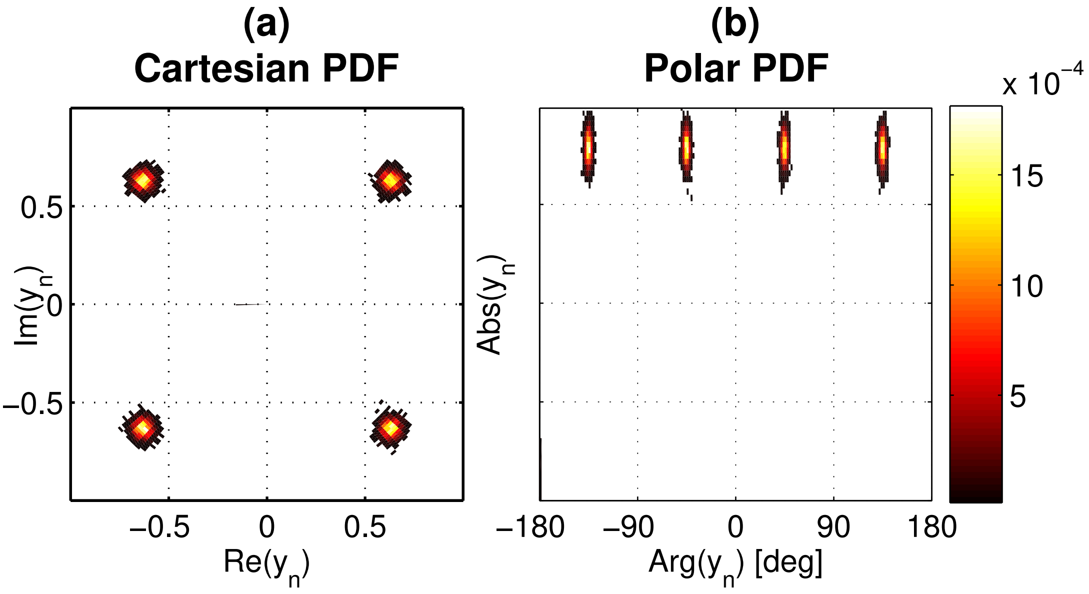

Figure 4.9: Received 4−QAM signal pdfs, ideal case. (a) C-CP. (b) P-CP.

where $\hat{a}$ indicates the symbols generated by the sampled transmission filter introduced in (4.12) and the operator $a * b$ identifies the convolution operation between a and b. The full analytic expression of the pdf of y_n in (4.19), that is influenced by the N_p long channel and the receiving architecture in Fig. 4.7, is

$$f(y_n) = \frac{1}{(pM)^{N_p+1}} \sum_{m_0=1}^{M} \sum_{m_1=1}^{M} \cdots \sum_{m_{N_p}=1}^{M} f_{\mathcal{N}_2}\left(y_n, \begin{bmatrix} \mathcal{R}(\sum_{n_p=0}^{N_p} \rho_{n_p} \hat{a}^{(m_{n_p})} e^{j\alpha_{n_p}^{(0)}}) \\ \mathcal{I}(\sum_{n_p=0}^{N_p} \rho_{n_p} \hat{a}^{(m_{n_p})} e^{j\alpha_{n_p}^{(0)}}) \end{bmatrix}, \sigma_w^2 \mathbb{I}_2 \right) , \tag{4.20}$$

that is a set of a zero mean BND pdfs with standard deviation σ_w, each one translated in everyone of the $(pM)^{N_p+1}$ possible values of the super-symbol $\hat{a}(h^{(0)}) = \sum_{n_p=0}^{N_p} \rho_{n_p} \hat{a}^{(m_{n_p})} e^{j\alpha_{n_p}^{(0)}}$ of the channel impaired constellation $\hat{\mathcal{A}}(h^{(0)})$. Where

$$\begin{aligned} \hat{\mathcal{A}}(h^{(0)}) &:= \hat{\mathcal{A}} \times \mathcal{H} \, , \\ \mathcal{H} &:= \left\{ h_{n_p}^{(0)} \right\}_{n_p=1,\dots,N_p} \, . \end{aligned} \tag{4.21}$$

the cardinality of $\hat{\mathcal{A}}(h^{(0)})$ is $(N_p+1)|\hat{\mathcal{A}}|$: $|\hat{\mathcal{A}}(h^{(0)})| = q(N_p+1)M$.

The complex expression in (4.20) can be also iteratively represented obtaining $f(y_n) =$

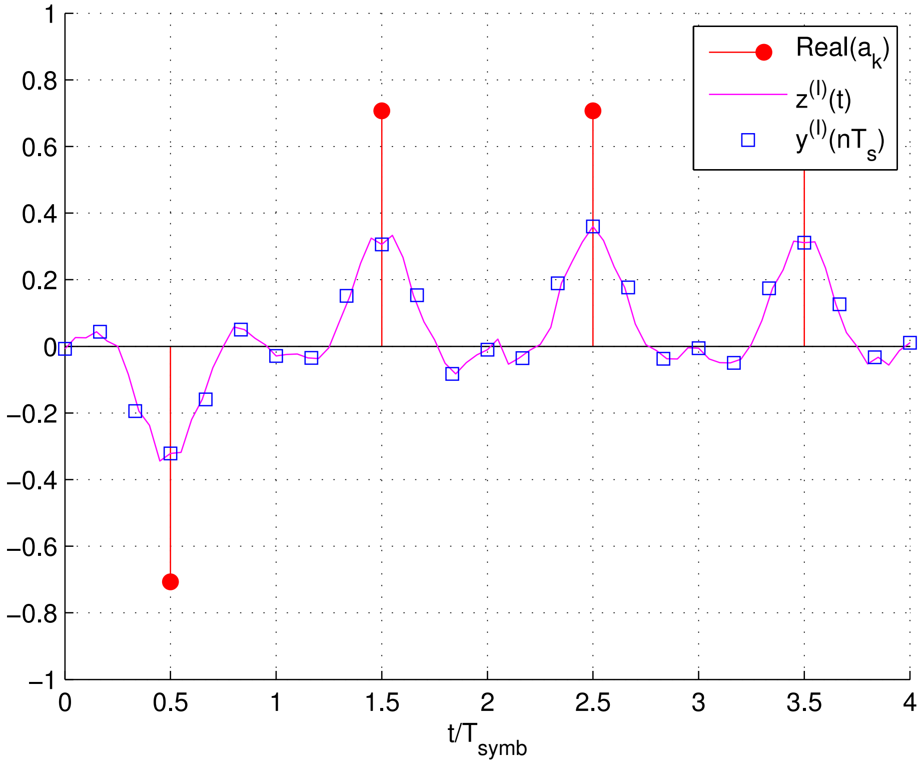

Figure 4.10: I component of the received 4-QAM time signal. Signal is modulated with a RRC filter and received by a LPF with rate $T_s = T_{\text{symb}}/6$.

$f_{0:N_p}(y_n)$ iteratively in N_p steps from the expression of $f_{n_p:N_p}(y_n)$, as following

$$f(y_n) = f_{0:N_p}(y_n) = \frac{1}{qM} \sum_{m=1}^{qM} f_{1:N_p}(y_n - \rho_0 \hat{a}^{(m)} e^{j\alpha_0^{(0)}}) \,, \tag{4.22}$$

$$f_{n_p:N_p}(y_n) = \frac{1}{qM} \sum_{m=1}^{qM} f_{n_p+1:N_p}(y_n - \rho_{n_p} \hat{a}^{(m)} e^{j\alpha_{n_p}^{(0)}}) \,, \tag{4.23}$$

$$f_{N_p-1:N_p}(y_n) = \frac{1}{qM} \sum_{m=1}^{qM} f_{N_P}(y_n - \rho_{N_p-1} \hat{a}^{(m)} e^{j\alpha_{N_p-1}^{(0)}}) \tag{4.24}$$

The last iteration in (4.22) is obtained starting from the pdf f_{N_P} contained in (4.24). The pdf f_{N_P} is obtained, as iteration 0, translating $f_{\text{norm}}(x)$, a BND with zero mean and standard deviation σ_w, in the qM values of $\rho_{N_p} \hat{a}^{(m)} e^{j\alpha_{N_p}^{(0)}}$. In the generic n_p-th following iteration, the pdf $f_{n_p:N_p}(y_n)$, is obtained translating the previously generated pdf $f_{n_p+1:N_p}$ in the pM values of $\rho_{n_p} \hat{a}^{(m)} e^{j\alpha_{n_p}^{(0)}}$:

$$f_{N_p}(y_n) = \frac{1}{qM} \sum_{m=1}^{qM} f_{\text{norm}}(y_n - \rho_{N_p} \hat{a}^{(m)} e^{j\alpha_{N_p}^{(0)}}) \,, \tag{4.25}$$

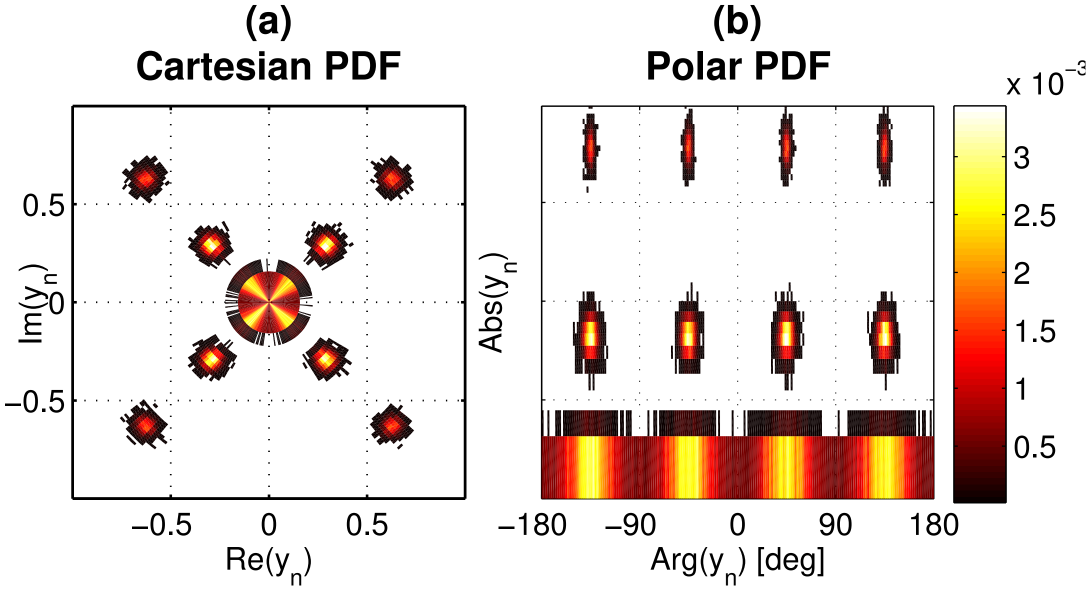

Figure 4.11: Received 4−QAM signal pdfs. Signal is modulated with a RRC filter g and received by a LPF with rate $T_s = T_{\text{symb}}/6$. (a) C-CP. (b) P-CP.

where

$$f_{\text{norm}}(x) = f_{\mathcal{N}_2}\left(x, \begin{bmatrix}0\\0\end{bmatrix}, \sigma_w^2 \mathbb{I}_2\right) . \tag{4.26}$$

For the sake of simplicity an example comprising a channel with 1 scatterer ($N_p = 1$) and an ideal receiving architecture with matched filter as in Fig. 3.2 is considered

$$y_n = \overbrace{\hat{a}_n \rho_0 e^{j\alpha_0^{(0)}}}^{\text{LOS component: } n_p=0} + \overbrace{\hat{a}_{n-1} \rho_1 e^{j\alpha_1^{(0)}}}^{\text{Scattering component: } n_p=1} + w_n . \tag{4.27}$$

The term representing the LOS complex component is composed by a complex symbol of constellation $\hat{\mathcal{A}}$ attenuated by ρ_0 and rotated by the PoA $\alpha_0^{(0)}$, this is the LOS received signal without noise and multipath effects. The term representing the reflected component is composed by a symbol of constellation $\hat{\mathcal{A}}$ attenuated by ρ_1 and rotated by $\alpha_1^{(0)}$. As displayed in (4.19), since both symbols $\hat{a}_n$ and $\hat{a}_{n-1}$ are elements of a constellation with cardinality $|\hat{\mathcal{A}}|$, the received signal pdf is a BND translated in all possible equiprobable $|\hat{\mathcal{A}}|^2$ values of the macro-symbol $\rho_0 \hat{a}_n e^{j\alpha_0^{(0)}} + \rho_1 \hat{a}_{n-1} e^{j\alpha_1^{(0)}}$. In Fig. 4.12 are depicted the pdfs of y_n under the following set of parameters: $N_p = 1$, $T_s = T_{\text{symbol}}$, $\Delta T_s = T_{\text{symbol}}/2$. Multipath parameters are $\alpha_1^{(0)}$=27deg and $\rho_1^{(0)}$=0.4. Besides, the LOS AoA parameter are $\alpha_0^{(0)}$=0deg for Fig. 4.12.

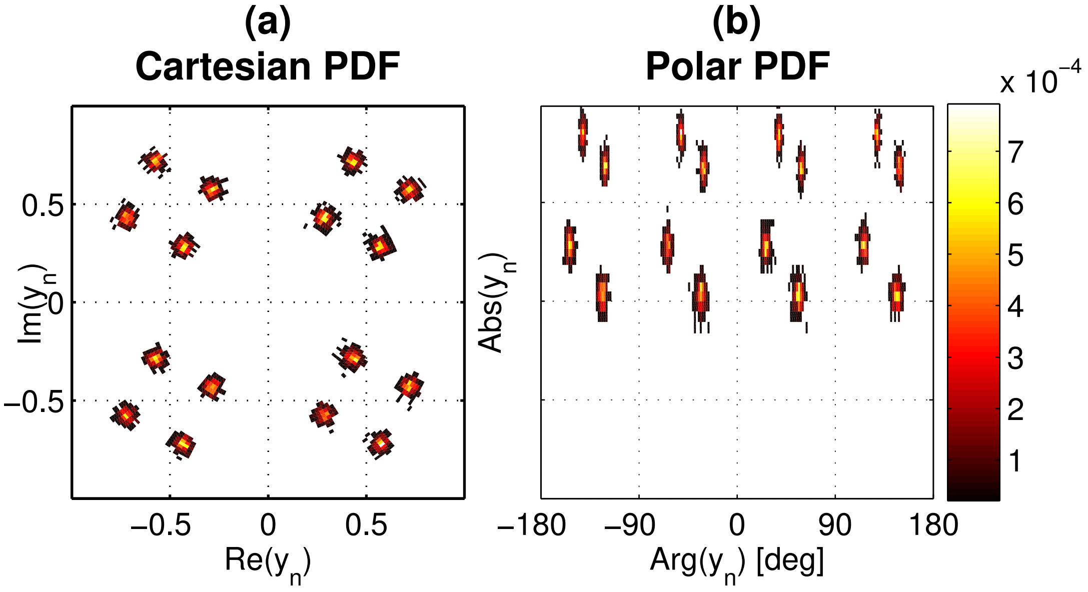

Figure 4.12: Received 4−QAM signal pdfs, $N_p = 1$ multipath case. LOS parameter: $\alpha_0^{(0)}$=0deg. Scatterer parameter: $\alpha_0^{(0)}$=27deg. (a) C-CP. (b) P-CP.

Geometric Interpretation of AoAs on Received pdfs

In this Sec. are considered the effects of MP in the pdfs of constellations of received signals. The same multipath model and receiving hardware considered in (4.27) are assumed. A ULA receiving array with 2 antennas lying in the y axis and $d/\lambda_0 = 1/8$ is considered. Received signals are respectively $y_n^{(1)}$ and $y_n^{(2)}$, their expressions, considering the antenna array's CIRs hypothesis introduced in Sec. 4.4 are

$$
\begin{aligned}
y_n^{(1)} &= \hat{a}_n \rho_0 e^{j\alpha_0^{(1)}} + \hat{a}_{n-1} \rho_1 e^{j\alpha_1^{(1)}} + w_n^{(1)}, \\
y_n^{(2)} &= \hat{a}_n \rho_0 e^{j\alpha_0^{(2)}} + \hat{a}_{n-1} \rho_1 e^{j\alpha_1^{(2)}} + w_n^{(2)}.
\end{aligned} \tag{4.28}
$$

As discussed in Sec. 4.4 the LOS phases $\alpha_0^{(n_a)}$ are related to the AoA θ_0. The phases $\alpha_1^{(n_a)}$ are instead related to the scatterer AoA θ_1. Channel phases are related to the AoAs following (4.7):

$$
\begin{aligned}
\Delta\alpha_0^{(2)} &= \alpha_0^{(2)} - \alpha_0^{(1)} = 2\pi \frac{d}{\lambda_0} \sin(\theta_0), \\
\Delta\alpha_1^{(2)} &= \alpha_1^{(2)} - \alpha_1^{(1)} = 2\pi \frac{d}{\lambda_0} \sin(\theta_1),
\end{aligned} \tag{4.29}
$$

where the D-PoAs $\Delta\alpha_0^{(2)}$ and $\Delta\alpha_1^{(2)}$ are related to the AoAs θ_0 and θ_1, respectively. A scenario with $\theta_1 = -61°$ is considered, leading to $\Delta\alpha_1^{(2)} = -51°$. In Fig. 4.13 are depicted the pdfs of $y_n^{(1)}$ and $y_n^{(2)}$. The AoA $\theta_1 = 0°$ is considered, leading to a $\Delta\alpha_0^{(2)} = -51°$. Comparing the pdfs in Fig. 4.13 it is evident the macro-rotation of 0° of the LOS constellations $\hat{\mathcal{A}}\rho_0 e^{j\alpha_0^{(1)}}$ due only to the AoA $\theta_0 = 0°$. The MP affects the pdfs with the received sub-constellations $\hat{\mathcal{A}}\rho_1 e^{j\alpha_1^{(n_a)}}$ translated in the values of the LOS constellation. Graphically is visible in Fig. 4.13 how the sub-constellation of antenna 2 is the sub-constellation of antenna 1 further rotated by $\Delta\alpha_1^{(2)}$. As described in (4.29) this rotation of sub-constellations visible comparing the pdfs of different antennas is due only to the scatterer AoA θ_1. Analogously to Fig. 4.13, in Fig. 4.14 are depicted the pdfs of $y_n^{(1)}$ and $y_n^{(2)}$ with the same MP parameters but with a different AoA configuration. The LOS AoA $\theta_1 = 30°$ is considered, leading to a $\Delta\alpha_0^{(2)} = 22.5°$ Comparing Fig. 4.13 and Fig. 4.14 it is evident the macro-rotation of the LOS constellation due to different AoAs. Contrariwise, despite the change of the LOS AoA θ_0 and the consequent rotation of the LOS constellation, the translated scatterer sub-constellations pdf, namely $f_{N_p}(y_n) = f_1(y_n)$, keep their patterns different only by a constant rotation factor $\Delta\alpha_1^{(2)}$ caused only by θ_1. In fact its expression $f_1(y_n) = \frac{1}{4}\sum_{m=1}^{4} f_{\text{norm}}(y_n - \rho_{N_p}\hat{a}^{(m)}e^{j\alpha_{N_p}^{(0)}})$ does not contain the AoA parameters $\alpha_0^{(n_a)}$ and ρ_0. This observation can be extended to any arbitrary

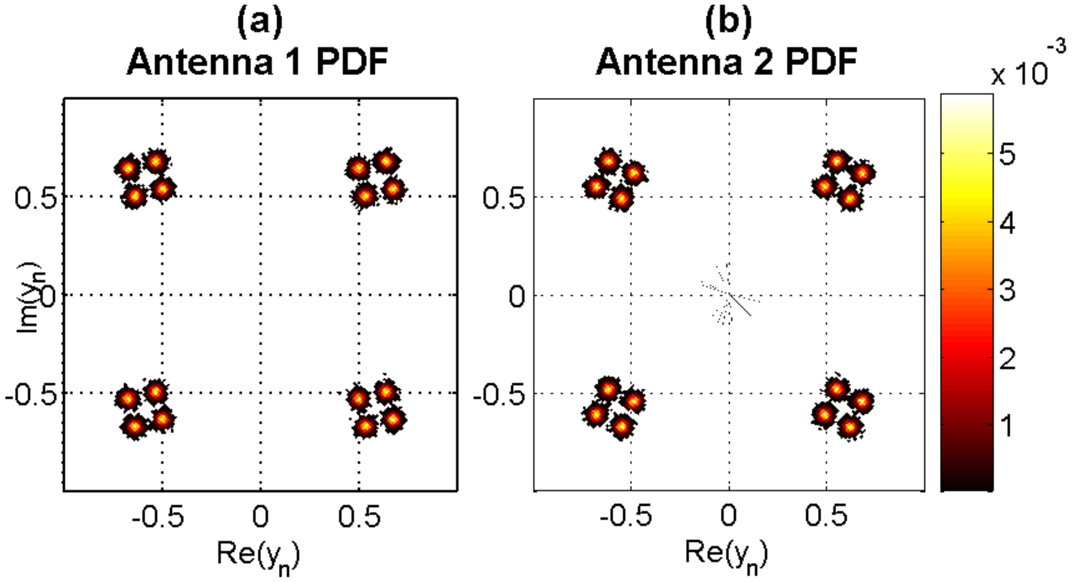

Figure 4.13: Received 4−QAM signal pdfs, $N_p = 1$ multipath case. LOS parameter: $\theta_0^{(0)}$=0deg. Scatterer parameter: $\theta_1^{(0)}$=−61deg.

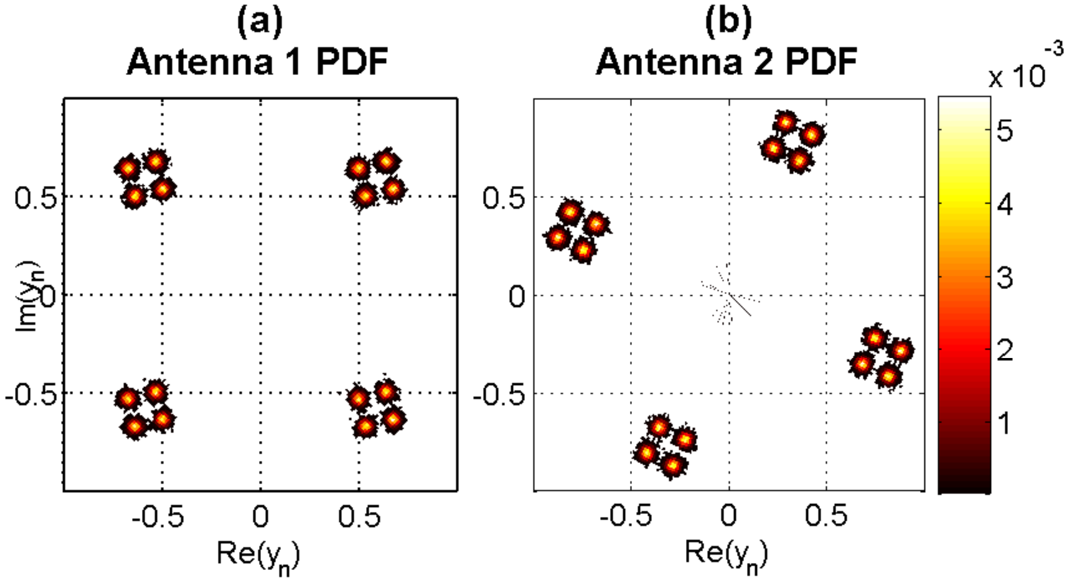

Figure 4.14: Received 4−QAM signal pdfs, $N_p = 1$ multipath case. LOS parameter: $\theta_0^{(0)}$=30deg. Scatterer parameter: $\theta_1^{(0)}$=−61deg.

N_p long US-CIR, in fact the partial pdf $f_{1:N_p}(y_n)$ introduced in (4.23) does not contain parameters influenced by AoA $\alpha_0^{(0)}$ and ρ_0 but only from scatterers AoAs.

The fact that the LOS AoA θ_0 does not directly influence $f_{1:N_p}(y_n)$, that is instead influenced only by scatterers AoAs θ_{n_p}, can be interpreted as a MP statistical fingerprint of the channel.

Conclusions

In this Ch. the Uniformly Sampled CIR (US-CIR) expression has been discussed as a simplification of real scenarios with continuous CIR expressions. A geometrical interpretation of the positions of the scatterers that produce a determined US-CIR has been carried out in Sec. 4.2. In Sec. 4.2 has been been verified that the US-CIR is able to represent a real MP scenario because the reduction of the CIR time sampling period allows an increased space resolution for scatterers positions. Considering a generic array of antennas, a method to obtain the CIR for each antenna from a main US-CIR has been developed in Sec. 4.3. A statistical method to generate the array CIRs with a real geometrical meaning has been developed in Sec. 4.4. The effects on the pdfs of received signals of the sensors CIRs have been analysed in Sec. 4.5 providing an graphical fingerprint interpretation of the array Uniformly Sampled CIR (US-CIR) in an AoA point of view.

Impaired Constellation Statistical Pattern Exploitation for AoA Estimation

5

In this Sec. two novel methods for AoA estimations are presented, namely Constellation Statistical Pattern Identification and Overlap (CSP-IDO) [33] in Sec. 5.1.4 and 2D CSP-IDO (BCID) in Sec. 5.2. Both CSP-IDO and BCID methods approach to AoA estimation is based on the statistical pattern exploitation of signals impinging on the receiving array sensors.

Single-Receiver Switched Opportunistic Approach to AoA Estimation in Hardware Impaired Scenarios

In this section, a novel switched hardware approach to AoA estimation in radio systems that signal using QAM is presented. The proposed algorithm, namely constellation statistical CSP-IDO, is based on the comparison of the probability density functions of successive signal snapshots from antennas (asynchronous approach). Contrariwise, other AoA techniques such as differential methods, beamforming and MUltiple SIgnal Classification (MUSIC) techniques are designed to acquire in parallel signals from the antennas (synchronous approach). CSP-IDO allows a significantly reduced hardware usage with respect to synchronous methods, without deteriorating precision. The proposed algorithm used with a time switched antenna approach leads to better performance in terms of overall hardware complexity, power consumption and possibly costs. Furthermore, CSP-IDO is robust to transmitter hardware impairments with respect to synchronous methods.

Introduction

Radio localization techniques such as AoA algorithms play an important role in the wider universe of positioning systems, e.g., GNSSs). The advantage of terrestrial radio localization w.r.t. GNSS is its feasible deployment in environments where satellite visibility is not achievable, i.e. indoor and canyon like scenarios [3].

AoA algorithms are dependent on which type of signals the transmitter emits. Several techniques have been developed to locate radio sources emitting specific waveforms, i.e. narrow band signals [5,6], broad band signals [7] and ad-hoc sequences [8]. Furthermore, the algorithm can be designed ad hoc to use certain waveforms and protocols, or it can work opportunistically by intercepting existing signals and requiring minimum knowledge on the signal format itself.

The algorithm herein proposed is designed to work opportunistically, using random QAM signals, and passively, without the need of calibration or previously agreed protocols. The main features of the proposed technique, namely constellation statistical pattern identification and overlap (CSP-IDO), are its reduced hardware that requires a single RF chain, its robustness to hardware impairments, and its passive/opportunistic applicability. The CSP-IDO method, illustrated in Sec. 5.1.4, is based on the analysis of the pdfs of successive signal snapshots taken from the antennas (asynchronous approach). Contrariwise, other AoA methods, such as beamforming [34,35] and root - multiple signal classifier (root-MUSIC (root-MUSIC)) [36], have been conceived to synchronously (in parallel) acquire signals from the antenna elements (synchronous approach).

This Ch. is organized as follows. The hardware simplification w.r.t. other methods is obtained thanks to the joint use of the CSP-IDO algorithm with the time switched antenna array. This is presented in Sec. 5.1.2. The simpler hardware translates in reduced power consumption and weight reduction which may ease portability and applications in the consumer domain. The robustness of the CSP-IDO method to the RF and baseband hardware impairments is discussed in Sec. 5.1.4. In Sec. 5.1.5, the proposed technique performance, in terms of AoA estimation RMSE, is evaluated and compared to other methods. It is shown that the proposed method is significantly more robust in presence of the hardware impairments discussed in Sec. 5.1.3 such as DCOs, IQU and it is applicable with the switched antenna architecture. It is envisioned, as a conclusion, that the method is applicable in several scenarios for passive/opportunistic AoA estimation, e.g. for localization of UAV [92], and for radio sources position monitoring [93].

Hardware Architecture for AoA Estimation

The baseband model for the transmitter is depicted in Fig. 5.1.a. The transmitter comprises a quadrature amplitude modulator (QAM) with pulse shaping filter $g(t)$ and a single antenna.

The radio receiver for the AoA estimation comprises three sections: the sensor part, consisting of an array of antennas, the RF front-end together with the signal acquisition stage, and the signal processing unit. Although not constrained to, we consider a uniform linear antenna array. Other structures can be considered with both two-dimensional and three-dimensional geometries [24,25].

The most common receiver front-end requires an RF down-conversion stage per antenna element as shown in Fig. 5.1.b [41, 94]. We propose the use of a time switched architecture that requires a single down-conversion branch as shown in Fig. 5.1.c. The multi branch receiver scheme in Fig. 5.1.b will be denoted in the following as full parallel architecture (FPA). FPA represents the baseline architecture used by synchronous AoA estimation methods that require the signals to be acquired synchronously from the antennas. The single receiver scheme in Fig. 5.1.c will be denoted in the following as TSA. TSA is the architecture considered by the proposed CSP-IDO technique that uses an asynchronous AoA estimation approach. The oversampling block present in both the FPA Fig. 5.1.b and TSA Fig. 5.1.c schemes comprises a low pass filter (LPF) and a sampling stage with sampling frequency higher than the transmitted symbol rate.

We assume that the transmitter in Fig. 5.1.a is affected by several and typical hardware impairments such as IQU, DCO and PO [41]. The receiver can also have antenna branches experiencing a different PO. The effect of these impairments on the QAM signal at the receiver side is discussed in Sec. 5.1.3.

pdf of Received Impaired QAM Signal

The transmitter in Fig. 5.1.a sends the data symbols a_n belonging to the uniformly spaced QAM square constellation. The discrete time signal is shaped with the pulse $g(t)$ and undergoes the transformations due to the various stages and impairments. The received signal is then acquired. In the ideal scenario, where the transmit and receive filters are matched and there are no impairments, the sampled received signal at one antenna branch can be written as

$$y_n = y(nT_{sym}) = a(nT_{sym}) + w(nT_{\mathrm{sym}}) \,, \tag{5.1}$$

where $w_n = w(nT_{sym}) \sim \mathcal{N}(0, \sigma_w)$ is the sampled additive white Gaussian noise (AWGN) with zero mean and standard deviation σ_w. The symbols $a_n = a(nT_{\mathrm{sym}})$ are the elements of a unitary energy M-QAM constellation transmitted at rate $1/T_{\mathrm{sym}}$.

As it will be explained in the following, we are interested in computing the probability density function (pdf) of the received discrete time signal. In the ideal case, just considered, the joint pdf of the real and imaginary parts of y_n is

$$f_{M\text{-QAM}}(y_n) = \sum_{m=1}^{M} P[a_n = a^{(m)}] \cdot f_{\mathcal{N}_2}\left(y_n, \begin{bmatrix} \mathcal{R}(a^{(m)}) \\ \mathcal{I}(a^{(m)}) \end{bmatrix}, \sigma_w^2 \mathbb{I}_2\right) , \tag{5.2}$$

where $\mathbb{I}_2$ is the 2×2 identity matrix. The symbol $a^{(m)}$ is the m-th element of an M-QAM constellation and $P[a_n = a^{(m)}]$ is the symbol probability. The function $f_{\mathcal{N}_2}$ in (5.2)

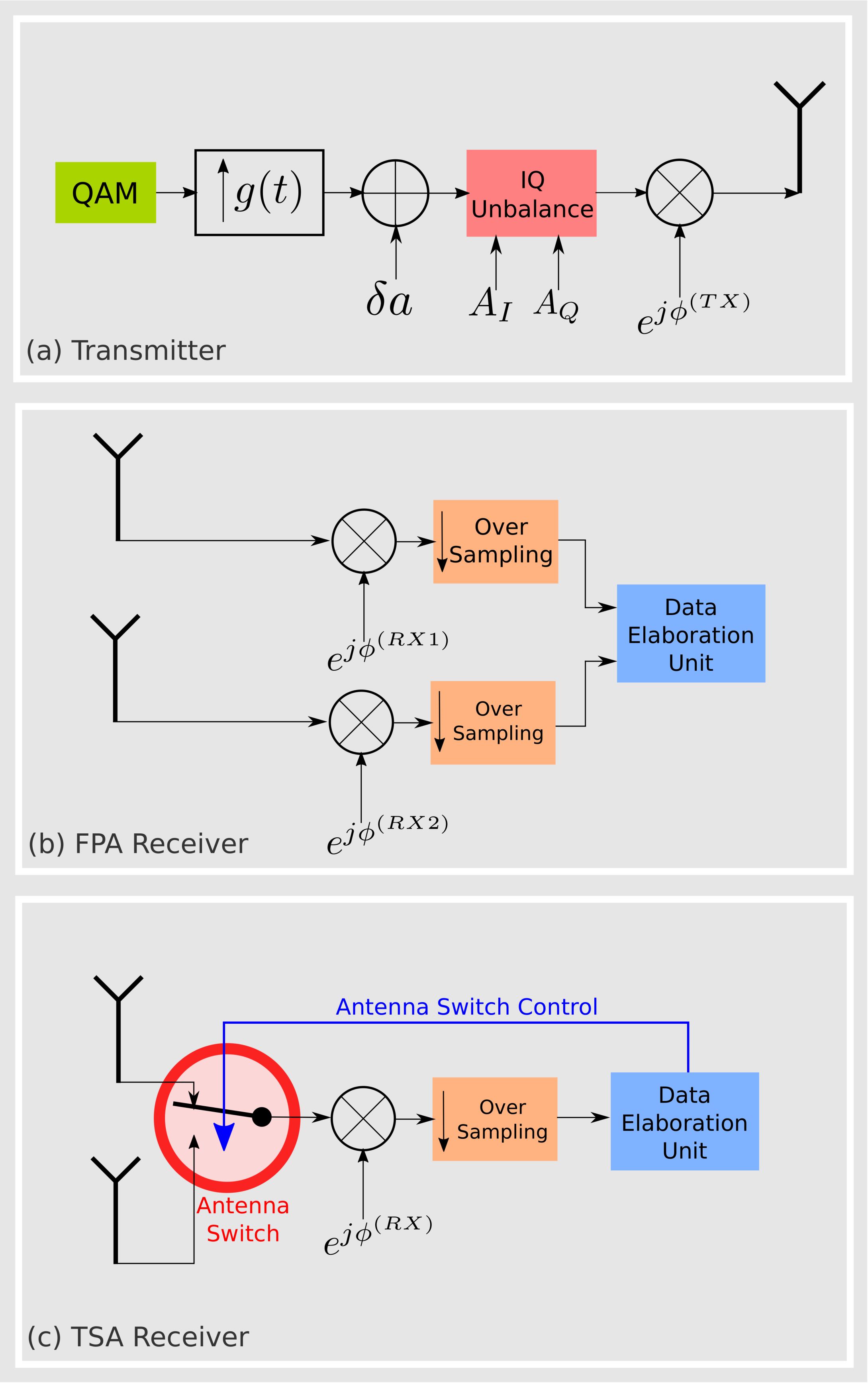

Figure 5.1: Hardware baseband schemes. (a) Transmitter. (b) FPA receiver. (c) TSA receiver.

represents the pdf of the bivariate normal distribution (BND) that is defined as

$$\begin{aligned} f_{\mathcal{N}_2}(y, \bar{\mu}, \mathbf{\Sigma}) &= \frac{1}{2\pi|\mathbf{\Sigma}|^{1/2}} e^{\frac{1}{2}(\bar{y}-\bar{\mu})^T \mathbf{\Sigma}^{-1}(\bar{y}-\bar{\mu})} , \\ \bar{y} &= \begin{bmatrix} \mathcal{R}(y) & \mathcal{I}(y) \end{bmatrix}^T , \\ \bar{\mu} &= \begin{bmatrix} \mathcal{R}(\mu) & \mathcal{I}(\mu) \end{bmatrix}^T , \\ \mathbf{\Sigma} &= \begin{bmatrix} \sigma_{\mathcal{R}}^2 & \rho\sigma_{\mathcal{R}}\sigma_{\mathcal{I}} \\ \rho\sigma_{\mathcal{I}}\sigma_{\mathcal{R}} & \sigma_{\mathcal{I}}^2 \end{bmatrix} , \end{aligned} \tag{5.3}$$

where $\mathcal{R}$ and $\mathcal{I}$ represent the real and imaginary part operator, respectively. The vector $\bar{y}$ comprises the real and the imaginary parts of y, and μ is the complex mean. $\mathbf{\Sigma}$ is the covariance matrix of the real and imaginary parts. The variables $\sigma_{\mathcal{R}}$ and $\sigma_{\mathcal{I}}$ are the standard deviations of $\mathcal{R}(y)$ and $\mathcal{I}(y)$, respectively. The constant ρ is the correlation coefficient between $\mathcal{R}(y)$ and $\mathcal{I}(y)$.

In the next sections, we will investigate the effect of the various hardware impairments on the pdf of the received signal. In particular, we will consider the effect of oversampling at the receiver side, the effect of DCO, of IQU as well as the effect of asynchronous transmitter and receiver oscillators. All of this is instrumental to introduce the proposed AoA estimation algorithm.

Oversampling the Received Signal

If the received signal is oversampled at the output of an ideal LPF, we obtain

$$\begin{aligned} y_n^{\mathrm{OVR}} &= y(nT_{\mathrm{ovr}}) = a * g(nT_{\mathrm{ovr}}) \cdot e^{j\beta_{\mathrm{fly}}} + w(nT_{\mathrm{ovr}}) \\ &= \tilde{a}_n \cdot e^{j\beta_{\mathrm{fly}}} + w_n , \end{aligned} \tag{5.4}$$

where $*$ stands for the interpolation and convolution operator, and $T_{\mathrm{ovr}} = T_{\mathrm{sym}}/N_{\mathrm{ovr}}$ is the sampling period at the receiver. The symbol $\tilde{a}_n$ represents the equivalent received constellation symbol modified by the oversampled transmission filter. The effect of the signal propagation time $\tau_{\mathrm{fly}} = \frac{-\beta_{\mathrm{fly}}}{2\pi f_0}$ between the transmitting and receiving antenna is modelled by the exponential term $e^{j\beta_{\mathrm{fly}}}$ where f_0 is carrier frequency. Thus, the pdf of y_n^{OVR} is

$$\begin{aligned} & f_{M\text{-QAM}}^{\mathrm{OVR}}(y_n^{\mathrm{OVR}}) = \\ & \frac{1}{MN_g} \sum_{m=1}^{MN_g} f_{\mathcal{N}_2} \left(y_n^{\mathrm{OVR}}, \mathbf{R}_{\beta_{\mathrm{fly}}} \begin{bmatrix} \mathcal{R}(\tilde{a}^{(m)}) \\ \mathcal{I}(\tilde{a}^{(m)}) \end{bmatrix}, \sigma_w^2 \mathbb{I}_2 \right) , \end{aligned} \tag{5.5}$$

where $\tilde{a}^{(m)}$ is a symbol generated from the M-QAM constellation interpolation with the oversampled transmission filter $g(nT_{\mathrm{ovr}})$ as shown in (5.4). The parameter N_g is the number of coefficients of the oversampled pulse g. The occurrence symbol probability is assumed to be uniform with value $1/(MN_g)$. The matrix $\mathbf{R}_{\beta_{\mathrm{fly}}}$ is the rotation matrix that expresses the effect produced by the propagation time τ_{fly}, in particular

$$\mathbf{R}_{\beta_{\text{fly}}} = \begin{bmatrix} \cos(2\pi\beta_{\text{fly}}) & -\sin(2\pi\beta_{\text{fly}}) \\ \sin(2\pi\beta_{\text{fly}}) & \cos(2\pi\beta_{\text{fly}}) \end{bmatrix} . \tag{5.6}$$

In Fig. 5.2, the pdf (5.5) is shown both in rectangular and polar coordinates. A RRC pulse with oversampling factor $N_{\text{ovr}} = 12$. The isolated peak values of the pdf placed in the domain area with the highest absolute value are generated by the peak of the RRC. The portion of the pdf located in the domain area with the lowest absolute value is generated by the tails of the RRC. The non zero propagation time affects the pdf in (5.5) with a clockwise rotation of $\beta_{\text{fly}} = -2\pi f_0 \tau_{\text{fly}}$ radians.

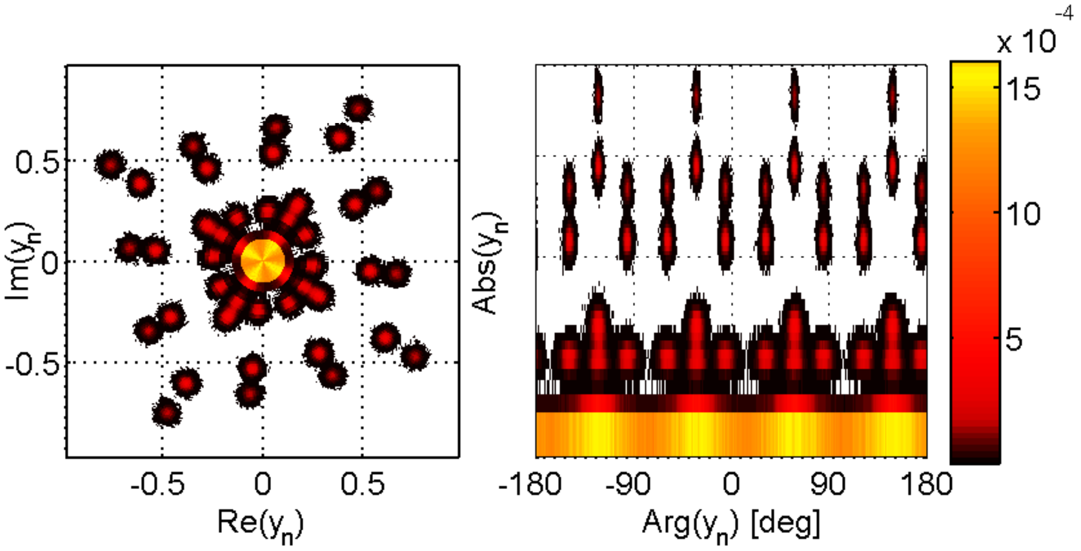

Figure 5.2: pdf of the received QAM signal (filtered by an RRC). Left: Cartesian representation. Right: polar representation.

Constellation Impaired by DCO

If we consider the DC offset caused by the DAC at the transmitter, the received oversampled signal can be written as

$$y_n^{\text{DCO}} = (\tilde{a}_n + \delta a) \cdot e^{j\beta_{\text{fly}}} + w_n \,, \tag{5.7}$$

where $\delta a = \delta a_Q + j\delta a_Q$ is the complex offset constant with real and imaginary components equal to δa_Q and δa_I, i.e. , the DCO introduced by the I and Q branch of the DAC, respectively. Thus, the pdf of y_n^{DCO} is

$$f_{M\text{-QAM}}^{\mathrm{DCO}}(y_n^{\mathrm{DCO}}) = \frac{1}{MN_g}\sum_{m=1}^{MN_g} f_{\mathcal{N}_2}\left(y_n^{\mathrm{DCO}}, \mathbf{R}_{\beta_{\mathrm{fly}}}\begin{bmatrix}\mathcal{R}(\tilde{a}^{(m)}+\delta a)\\ \mathcal{I}(\tilde{a}^{(m)}+\delta a)\end{bmatrix}, \sigma_w \mathbb{I}_2\right). \tag{5.8}$$

In Fig. 5.3, the pdf in (5.8) is shown both in rectangular and polar coordinates. The DCO impairment affects the pdf in (5.8) with a translation of the domain w.r.t. the ideal one. The translation is applied before the propagation time rotation effect. In the polar representation of (5.8) in Fig. 5.3, it is clearly visible how the translation of the pdf domain modifies the periodic symmetry w.r.t the phase axes from period $\pi/2$ to 2π.

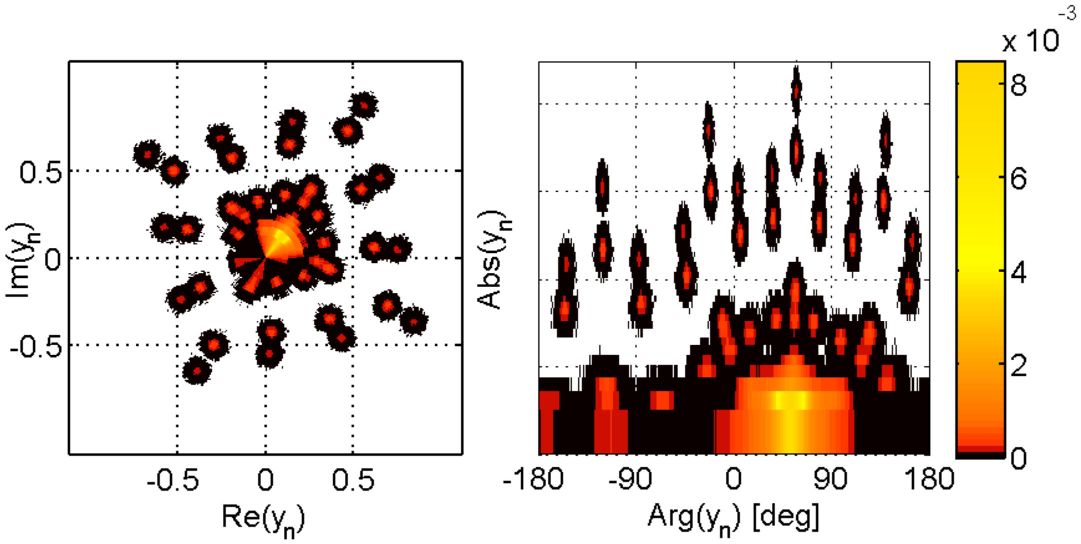

Figure 5.3: pdf of the received QAM signal (filtered by an RRC and affected by DCO). Left: Cartesian representation. Right: polar representation.

Constellation Impaired by IQU

The I-Q imbalance generated by the mixers asymmetric amplification of the I and Q components is translated at the receiver side in the following signal:

$$y_n^{\mathrm{IQU}} = [A_I\mathcal{R}(\tilde{a}_n) + jA_Q\mathcal{I}(\tilde{a}_n)]\cdot e^{j\beta_{\mathrm{fly}}} + w_n\,, \tag{5.9}$$

where A_I and A_Q are the different amplifications introduced by the mixers respectively to the I and Q branches of the quadrature modulator. It follows that the pdf of the received signal y_n^{IQU} becomes

$$f_{M\text{-QAM}}^{\mathrm{IQU}}(y_n^{\mathrm{IQU}}) = \frac{1}{MN_g}\sum_{m=1}^{MN_g} f_{\mathcal{N}_2}\left(y_n^{\mathrm{IQU}}, \mathbf{R}_{\beta_{\mathrm{fly}}}\mathbf{A}\begin{bmatrix}\mathcal{R}(\tilde{a}^{(m)})\\ \mathcal{I}(\tilde{a}^{(m)})\end{bmatrix}, \sigma_w^2\mathbb{I}_2,\right), \tag{5.10}$$

where,

$$\mathbf{A} = \begin{bmatrix} A_I & 0 \\ 0 & A_Q \end{bmatrix}. \tag{5.11}$$

In Fig. 5.4, the pdf reported in (5.10) is shown both in rectangular and polar coordinates. The IQU impairment affects the pdf (5.10) with the scale factors A_I and A_Q applied to the real and complex parts of y_n^{IQU}. The transformation is applied before the rotation caused by the propagation time. In the polar representation of (5.10) in Fig. 5.4, we can see how the asymmetric scale factor of the pdf domain changes the periodic symmetry w.r.t the phase axes from period $\pi/2$ to π.

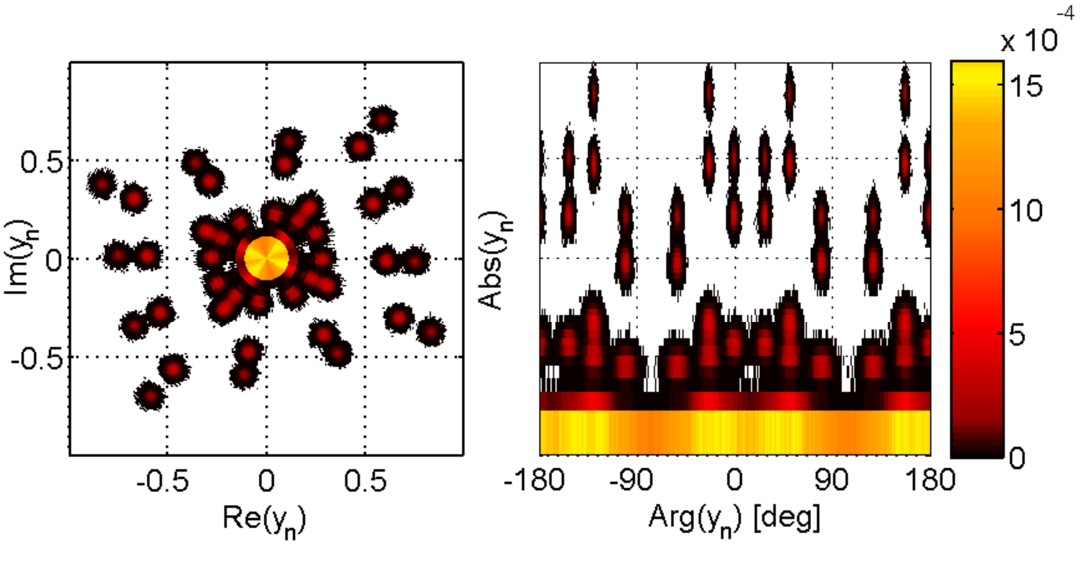

Figure 5.4: pdf of the received QAM signal (filtered by an RRC and affected by IQU). Left: Cartesian representation. Right: polar representation.

Constellation Statistical Pattern Identification and Overlap Algorithm (CSP-IDO)

In order to estimate the AoA, the proposed CSP-IDO algorithm performs the comparison of the pdf patterns of successive signal snapshots taken from the antennas. It works with the TSA which requires a single RF down conversion stage.

To proceed we consider two receiving antennas. The antenna 1 is positioned in the Cartesian coordinates $(0, -d/2)$ and the antenna 2 in $(0, +d/2)$. The transmitter antenna is located at distance $D >> d$ from the center of the axis. Its angular position w.r.t. the positive x-axis where the receiver is located is θ. Using the TSA receiver, both time switched antennas share the same constellation transformations, in the presence of the hardware impairments discussed before in Sec. 5.1.3. Only the propagation time to reach the antennas is in general different depending on the relative position of the transmitter w.r.t the receiver antennas. If the FPA receiver is used, then each RF down conversion branch can exhibit in addition a different POs due to non synchronized oscillators. The PO introduces distinct constellation rotations in each receiver antenna branch similarly to the propagation time rotation introduced in (5.4). It follows that the received sample signal can be written as:

$$y_n^{(i)} = [A_I \mathcal{R}(\tilde{a}_n + \delta a) + j A_Q \mathcal{I}(\tilde{a}_n + \delta a)] \cdot e^{j(\beta_{\text{fly}}^{(i)} + \Delta\phi^{(i)})} + w_n \,. \tag{5.12}$$

The constants A_I and A_Q account for the IQU impairment introduced in Sec. 5.1.3. The complex constant δa is the cause of DCO translation introduced in Sec. 5.1.3. The angular rotation parameter $\beta_{\text{fly}}^{(i)} = -2\pi f_0 \tau_{\text{fly}}^{(i)}$ is caused by the propagation time. The parameter $\Delta\phi^{(i)}$ is the PO between the transmitter oscillator and the i-th receiver oscillator. It causes a spurious constellation rotation. It follows that the pdf of the received samples $y_n^{(i)}$ at the i-th antenna of the FPA is:

$$f_{M\text{-QAM}}^{(i)}(y_n^{(i)}) = \frac{1}{MN_g} \sum_{m=1}^{MN_g} f_{\mathcal{N}_2}\left(y_n^{(i)}, \hat{\mathbf{U}}_i, \sigma_w^2 \mathbb{I}_2\right) \,, \tag{5.13}$$

where,

$$\hat{\mathbf{U}}_i = \mathbf{R}_{\Delta\phi^{(i)}} \mathbf{R}_{\beta_{\text{fly}}^{(i)}} \mathbf{A} \begin{bmatrix} \mathcal{R}(\tilde{a}^{(m)} + \delta a) \\ \mathcal{I}(\tilde{a}^{(m)} + \delta a) \end{bmatrix} . \tag{5.14}$$

The propagation time is included by the rotation matrix $\mathbf{R}_{\beta_{\text{fly}}^{(i)}}$ introduced in (5.6), while $\mathbf{R}_{\Delta\phi^{(i)}}$ models the constellation rotation caused by PO. The matrix $\mathbf{A}$ defined in (5.11) accounts for the IQU.

Considering the TSA, the parameters of the pdf in (5.14) for antenna 1 and 2 differ only for the propagation rotation matrix $\mathbf{R}_{\beta_{\text{fly}}^{(i)}}$ since such signal snapshots are received at different time instants by the same RF branch. Contrariwise, FPA provides also different

$\mathbf{R}_{\Delta\phi^{(i)}}$ since it is constituted by multiple RF branches that lead to different POs. It follows that the matrix in (5.14) associated to the signals taken from the two antennas of the TSA are related as follows:

$$\hat{\mathbf{U}}_2 = \mathbf{R}_{\Delta\beta}\hat{\mathbf{U}}_1 \,, \tag{5.15}$$

where $\Delta\beta = \beta^{(2)}_{\text{fly}} - \beta^{(1)}_{\text{fly}}$ is the differential phase of arrival (D-PoA). The D-PoA is the parameter that needs to be estimated to obtain the AoA.

The relation in (5.15) shows that the 2D patterns of the pdfs $f^{(1)}_{M\text{-QAM}}$ and $f^{(2)}_{M\text{-QAM}}$, differ for only the Cartesian rotation of their domain by $\Delta\beta$. Therefore, if $f^{(i)}(\gamma)$ is defined as the pdf of the phase $\gamma^{(i)}_n = \arg\left(y^{(i)}_n\right) \in [0, 2\pi)$ of the received samples from antenna i (where $\arg(\bullet)$ denotes the argument operator), it will be that the pdf associated to the signal of the other antenna is

$$f^{(2)}(\gamma) = f^{(1)}(\gamma + \Delta\beta)\,. \tag{5.16}$$

Then, the pdfs $f^{(1)}(\gamma)$ and $f^{(2)}(\gamma)$ differ only by an angular circular shift of $\Delta\beta$ in the 2π periodic domain $[0, 2\pi)$.

In the proposed method, namely Constellation Statistical Pattern Identification and Overlap (CSP-IDO), $\Delta\beta$ is estimated from the circular correlation between $f^{(1)}(\gamma)$ and $f^{(2)}(\gamma)$, that is defined as

$$\mathcal{C}(\Delta\gamma) = \int\limits_0^{2\pi} f^{(1)}(\gamma) f^{(2)}\left((\gamma - \Delta\gamma) \pmod{2\pi}\right) d\gamma \tag{5.17}$$

where the operator $\pmod{2\pi}$ denotes the modulo 2π operation. In the interval $\Omega_K = [-K, K)$ the circular correlation $\mathcal{C}(\Delta\gamma)$ reaches its maximum when $f^{(1)}(\gamma)$ and $f^{(2)}(\gamma)$ are overlapped. This happens when $\Delta\gamma = \Delta\beta$. The parameter $K = 2\pi d/\lambda_0$ is the maximum D-PoA obtainable by the array, λ_0 is the carrier wavelength. Then, the estimation $\widehat{\Delta\beta}$ of the D-PoA $\Delta\beta$ is obtained as follows:

$$\widehat{\Delta\beta} = \underset{\Delta\gamma\in\Omega_K}{\text{argmax}} \left\{\mathcal{C}(\Delta\gamma)\right\} \,, \tag{5.18}$$

where the operator $x_{max} = \underset{x}{\text{argmax}}\left\{p(x)\right\}$ returns the argument for which the function is maximum.

The CSP-IDO algorithm needs the practical evaluation of $f^{(i)}(\gamma)$ which is essentially done by computing the histogram of the received signal samples. The parallel processing of the signals $y^{(i)}_n$ using FPA is not necessary. For this reason, using the TSA, the pdfs can be calculated from successive time switched snapshots of the received signals acquired from different antennas, avoiding the use of a full bank of RF front-ends. In the following it will be illustrated how the hardware impairments introduced in Sec. 5.1.2, such as IQU, IQSand DCO affect the CSP-IDO behaviour. The phase patterns variations of the pdfs

$f^{(1)}(\gamma)$ and $f^{(1)}(\gamma)$, and of the circular correlation $\mathcal{C}(\Delta\gamma)$ are investigated. For the sake of the example, the distance between receiving antennas is setted as $d = \lambda_0/2$ leading to a value of D-PoA spanning from $-180°$ and $-180°$. This choice is made to better explain how the phase symmetries in the pdfs and in the circular convolution affect the estimation process.

Firstly, the oversampled ideal case without hardware impairments introduced in Sec. 5.1.3 is analysed. As discussed previously, the phase patterns $f^{(1)}(\gamma)$ and $f^{(1)}(\gamma)$ visible in Fig. 5.5.(a) are periodic with period 90°. For this reason the expression of the circular correlation $\mathcal{C}(\Delta\gamma)$ in Fig. 5.5.(b)is periodic of 90°. The estimation process in (5.18), that leads to $\widehat{\Delta\beta}$, must be performed in the domain $\Delta\gamma \in [-\pi/4, \pi/4]$ for consistent results. This limited domain reflects the estimation process limiting the D-PoAs resolution and then the range of AoA computable. This limitation can be solved providing antenna couples with distance lower than $\lambda/8$ leading maximum D-PoAs of $\pi/4$.

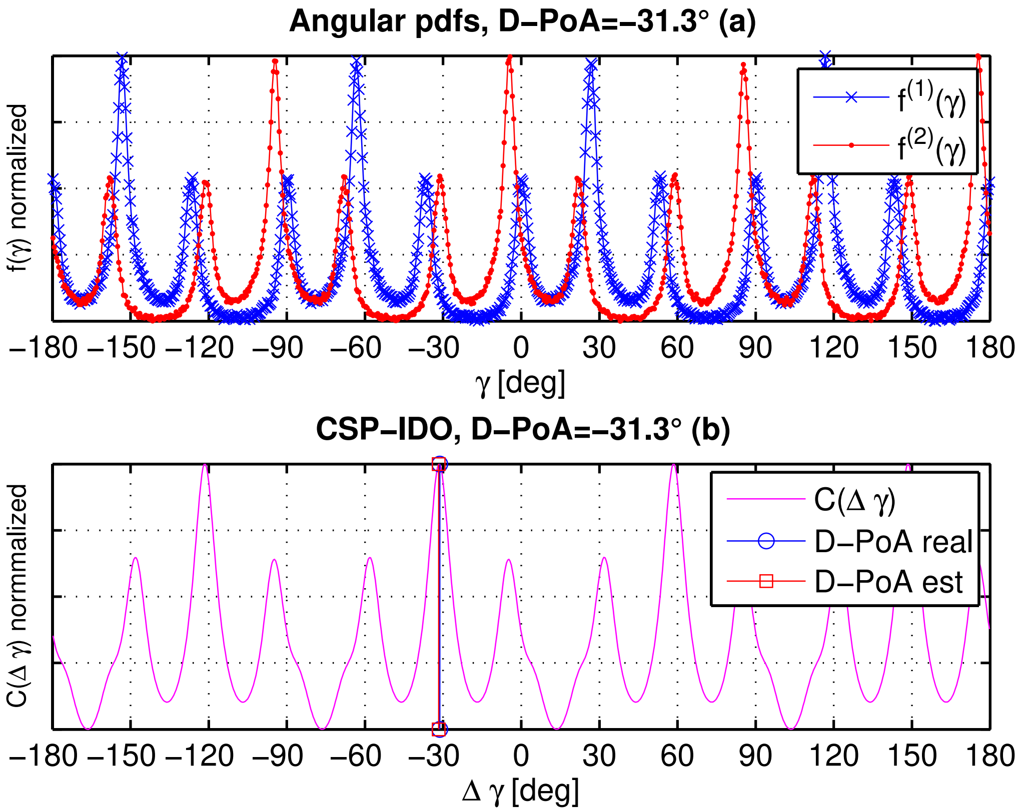

Figure 5.5: CSP-IDO method, no impairments. D-PoA $= -31.3°$. (a) Constellations angular histograms. (b) CSP-IDO circular correlation.

The effects on IQU introduced in Sec. 5.1.3 are now analysed. As discussed previously, the phase patterns $f^{(1)}(\gamma)$ and $f^{(1)}(\gamma)$ visible in Fig. 5.6.(a) are periodic with period 180°. For this reason the expression of the circular correlation $\mathcal{C}(\Delta\gamma)$ in Fig. 5.6.(b)is periodic of 180°. The estimation process in (5.18), that leads to $\widehat{\Delta\beta}$, must be performed in the domain $\Delta\gamma \in [-\pi/2, \pi/2]$ for unique results. This limited domain reflects the estimation process limiting the D-PoAs resolution and then the range of AoA computable. This limitation can be solved providing antenna couples with distance lower than $\lambda/4$ leading maximum D-PoAs of $\pi/2$.

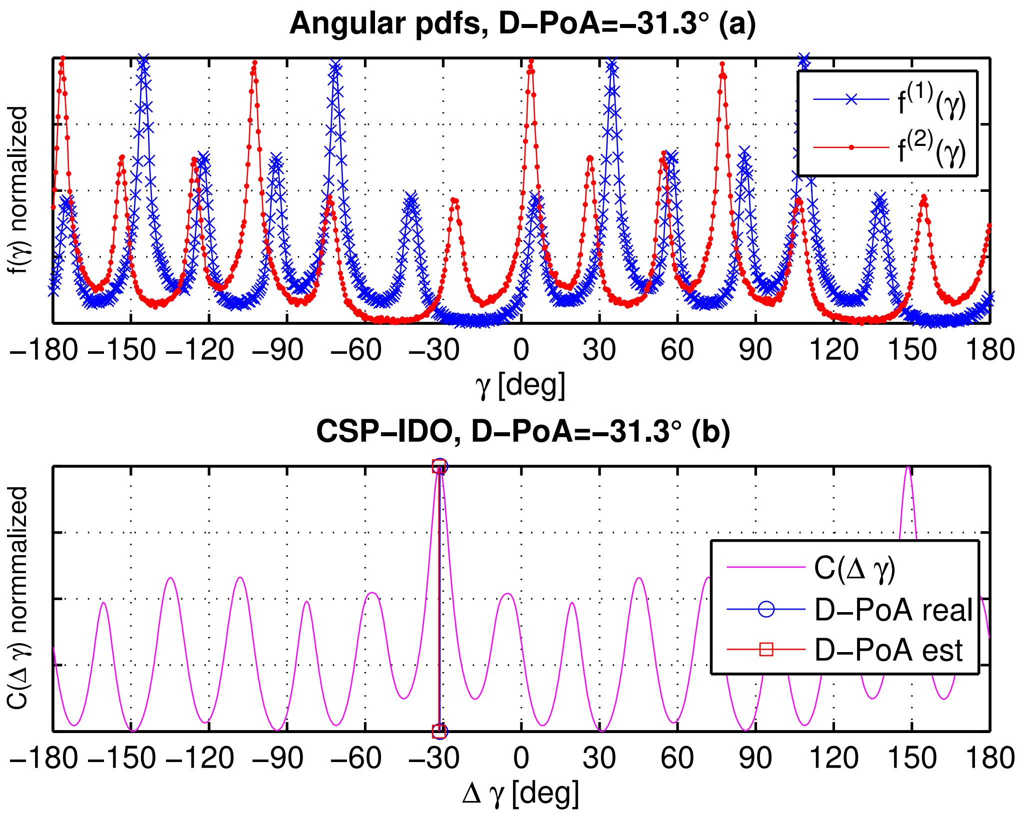

Figure 5.6: CSP-IDO method, impairment: IQU. D-PoA $= -31.3°$. (a) Constellations angular histograms. (b) CSP-IDO circular correlation.

The effects on IQS are now analysed. Similarly to IQU, the phase patterns $f^{(1)}(\gamma)$ and $f^{(1)}(\gamma)$ visible in Fig. 5.7.(a) are periodic with period 180°. For this reason the expression of the circular correlation $\mathcal{C}(\Delta\gamma)$ in Fig. 5.7.(b)is periodic of 180°. The estimation process in (5.18), that leads to $\widehat{\Delta\beta}$, must be performed in the domain $\Delta\gamma \in [-\pi/2, \pi/2]$ for unique results. This limited domain reflects the estimation process limiting the D-PoAs resolution and then the range of AoA computable. This limitation can be solved providing antenna couples with distance lower than $\lambda/4$ leading maximum D-PoAs of $\pi/2$.

The effects on DCO introduced in Sec. 5.1.3 are now analysed. Differently to IQU and IQS, the phase patterns $f^{(1)}(\gamma)$ and $f^{(1)}(\gamma)$ visible in Fig. 5.7.(a) are not periodic. For this reason the expression of the circular correlation $\mathcal{C}(\Delta\gamma)$ in Fig. 5.8.(b)is not periodic. The estimation process in (5.18), that leads to $\widehat{\Delta\beta}$, can be performed in the complete domain $\Delta\gamma \in [-\pi, \pi]$. Since periodicity limitation are not present, the estimation process can solve all possible D-PoAs leading then a full estimation range for the AoA.

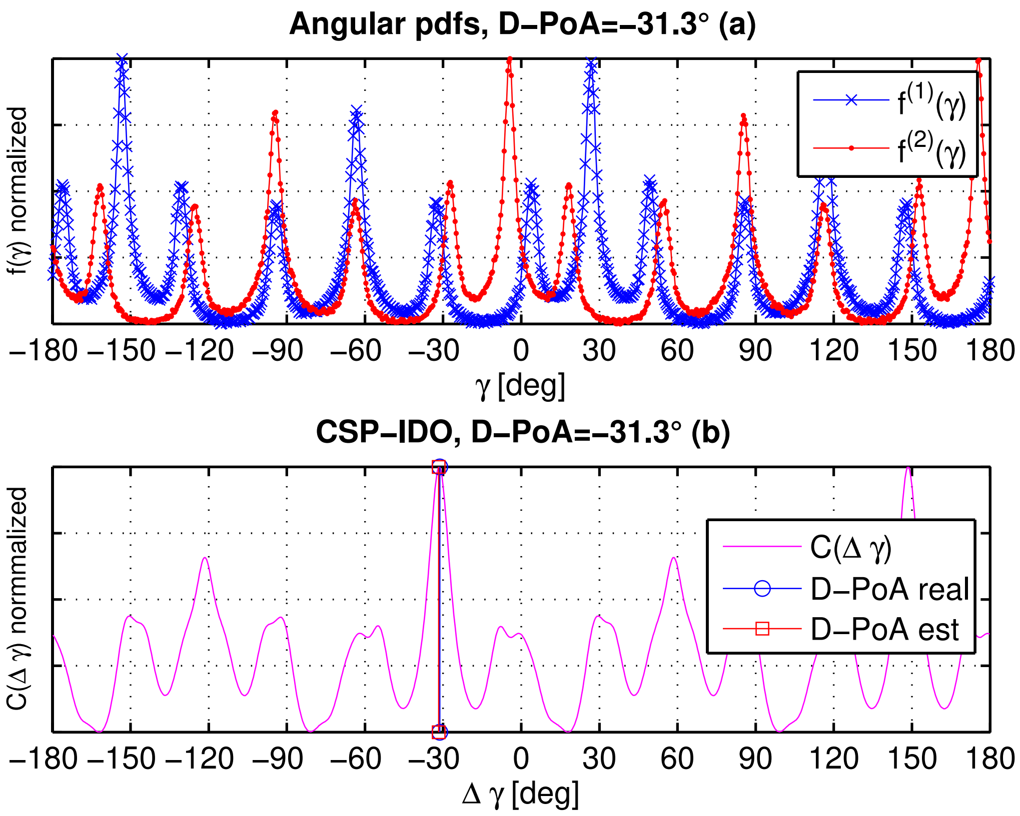

Figure 5.7: CSP-IDO method, impairment: IQS. D-PoA $= -31.3°$. (a) Constellations angular histograms. (b) CSP-IDO circular correlation.

Performance Analysis

For the performance evaluation, both the FPA and TSA systems are considered. The transmitter emits randomly generated 16-QAM data symbols with symbol rate $T_{\mathrm{sym}} = 4$ μs. The Signal to Noise Ratio (SNR) at the receiver is 20 dB. The carrier frequency is $f_0 = c_0/\lambda_0 = 2.4$ GHz, where c_0 is the speed of light and λ_0 is the carrier wavelength. The inter-antenna distance is set $d = \lambda_0/8$ m. The considered parameters are consistent to a single sub-channel of the multi-carrier system Institute of Electrical and Electronic Engineers (IEEE)802.11a [95].

For all simulation results, the same acquisition time $T_{\mathrm{tot}} = 320\,T_{\mathrm{sym}} = 1.28$ ms is used with the oversampling parameter $N_{\mathrm{ovr}} = 12$. The performance evaluation is made through $N_{\mathrm{it}} = 4 \cdot 10^4$ iterations. Furthermore, the received signals are affected by the impairments discussed, in order: transmitter DCO, transmitter IQU and oscillators PO. The DCO δa introduced in Sec. 5.1.3, is considered a zero mean Gaussian random variable with standard deviation $\sigma_{\mathrm{DCO}} = 1/30$. Similarly, the IQU parameters A_I and A_Q introduced in Sec. 5.1.3 are considered unitary mean Gaussian random variables with standard deviation $\sigma_A = 1/30$. The PO values $\Delta\phi^{(i)}$ are considered independent uniform random variables from 0 to 2π (this choice holds true since receiver branches are physically separated).

The CSP-IDO algorithm has been numerically implemented by estimating the pdfs in

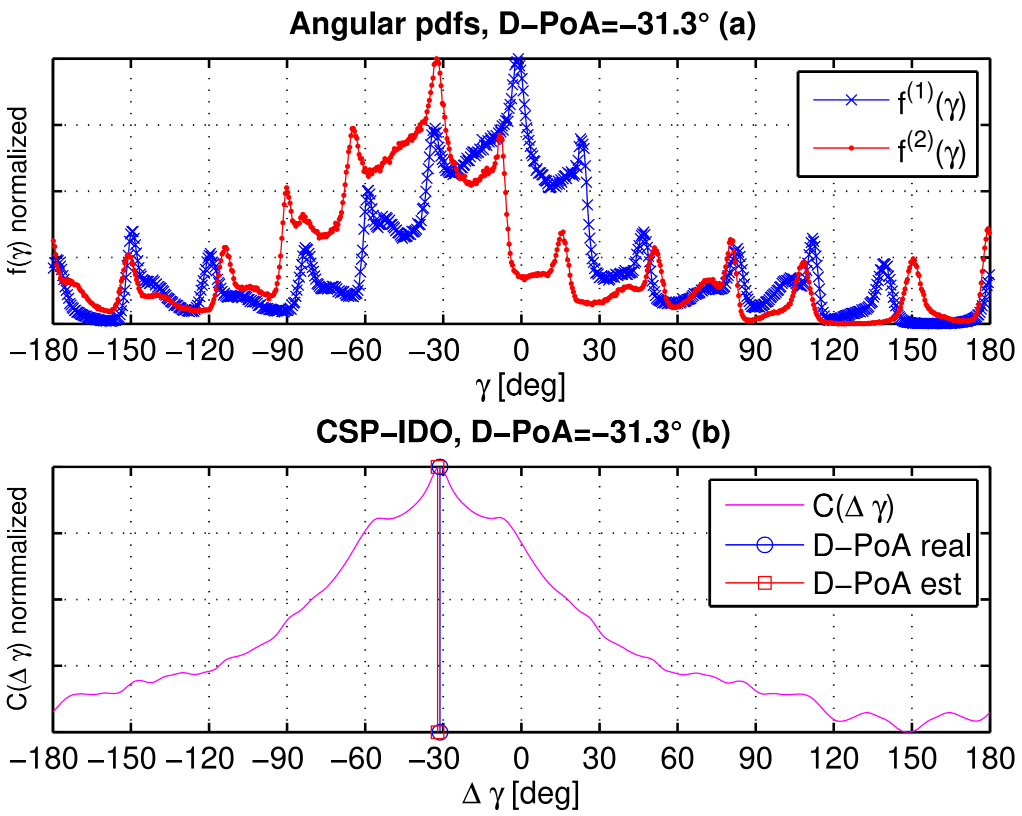

Figure 5.8: CSP-IDO method, impairment: DCO. PoA = −31.3°. (a) Constellations angular histograms. (b) CSP-IDO circular correlation.

(5.17) via the histogram computation.

The performance of the proposed CSP-IDO algorithm is compared with other 3 methods, that we denote with Method A and B, and with the root-MUSIC algorithm [36].

The Method A has been used in [41] with a calibration approach and essentially it estimates the antenna phase difference (and then the AoA) with the following metric:

$$\Delta\beta^{(A)} = \frac{1}{N} \arg\left[\sum_{n=1}^{N} y_n^{(2)} y_n^{(1)*}\right]. \tag{5.19}$$

where $N = 3840$ is the number of acquired samples. Method A needs calibration to compensate the detrimental effects of the hardware.

The Method B, is a proposed baseline technique that extracts the D-PoA from the average of the phase of the received signals with the following metric:

$$\Delta\beta^{(B)} = \frac{1}{N} \sum_{n=1}^{N} \left(\arg\left(y_n^{(2)}\right) - \arg\left(y_n^{(1)}\right)\right). \tag{5.20}$$

Method B, to correctly work, needs the QAM constellations to be symmetric. Method B is proposed as a comparison to Method A in terms of robustness w.r.t. SNR and hardware impairments since, in the ideal case, their means are identical.

From (5.18), (5.19), and (5.20) the AoA is obtained as

$$\theta = \arcsin\left[-\frac{\Delta\beta}{K}\right]. \tag{5.21}$$

The root-MUSIC algorithm performance is computed to test its robustness w.r.t. the SNR, the hardware impairments, the receiving architectures and the QAM modulation.

The performance of the AoA estimators is evaluated in terms of RMSE)

$$\mathrm{RMSE}(\theta, \tilde{\theta}) = \sqrt{\sum_{i=1}^{N_{it}} \frac{([\theta - \tilde{\theta}_i]_{-\pi,\pi})^2}{N_{it}}}, \tag{5.22}$$

where θ is the real AoA and $\tilde{\theta}_i$ is its estimate at iteration i. The operator $[\alpha]_{-\pi,\pi}$ denotes the wrapped angle α inside the $[-\pi, \pi)$ domain.

FPA Case

Herein, the Methods A, B and the root-MUSIC algorithm use the FPA while the CSP-IDO algorithm uses the TSA. The acquisition time is the same for both architectures. The hardware requirement for Methods A, B and for root-MUSIC is double w.r.t. the CSP-IDO algorithm. The RMSE of the AoA estimation as a function of the AoA is shown in Fig. 5.9. In Fig. 5.9.a the ideal case without hardware impairments is considered, while in Fig. 5.9.b the hardware impaired scenario is considered. Impaired hardware coefficents are presented in Sec. 5.1.5. In the ideal case, the FPA system with Method A, depicted in Fig. 5.9.a performs better than all other methods. This because Method A can exploit simultaneously a double number of samples w.r.t. CSP-IDO. This is particularly evident for large AoA. For smaller AoA (below 70 degrees), Method A and CSP-IDO perform similarly. In the impaired hardware case of Fig. 5.9.b, the CSP-IDO algorithm outperforms all methods. It is interesting to notice that CSP-IDO in the impaired hardware scenario performs better than itself in the ideal hardware scenario. This counter-intuitive behaviour is explained with the asymmetry of the received QAM constellation visible in Fig. 5.3 and Fig. 5.4 as a result of the presence of DCO and IQU. This asymmetry causes the circular correlation introduced in (5.17) to be sharper than the one obtained in the ideal scenario where the QAM constellations are symmetric. The root-MUSIC algorithm performance is affected in Fig. 5.9.a by the time varying QAM symbols. The root-MUSIC performance is then strongly decremented in Fig. 5.9.b by the hardware impairments. In fact nearly 70% of the iterations do not converge. The performance of Method B in both scenarios is very low, showing the weakness w.r.t. noise and impaired hardware.

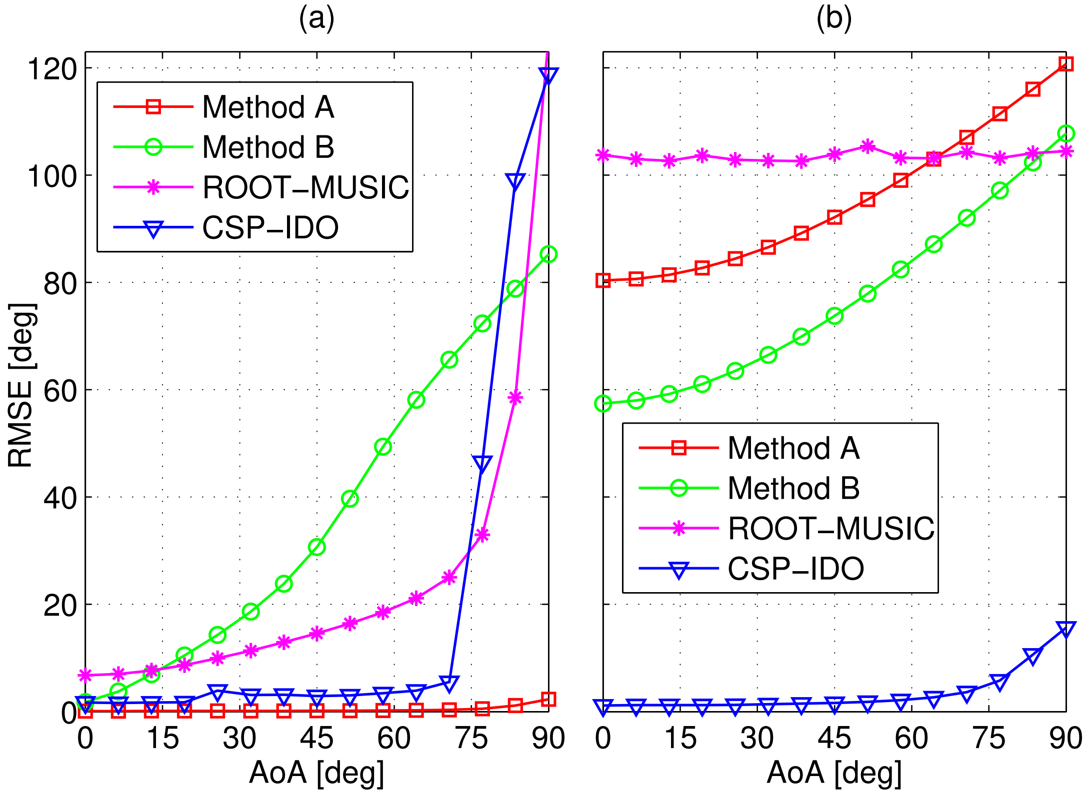

Figure 5.9: RMSE for different AoA. Methods A,B and root-MUSIC algorithm are applied to the FPA, CSP-IDO uses the TSA. (a) Ideal hardware. (b) Impaired hardware.

TSA Case

We now consider all methods applied to a system that uses the TSA. Again, the acquisition time is the same for all algorithms. In this scenario, the root-MUSIC method can't be applied correctly since it requires a simultaneous acquisition of the received signals to converge to meaningful results. The ideal case is considered in Fig. 5.10.a while the hardware impaired scenario is considered in Fig. 5.10.b. Impaired hardware coefficents are presented in Sec. 5.1.5. In both scenarios, the CSP-IDO outperforms Methods A and B, except when the AoA exceeds 80 degrees in the ideal case. For the same reasons explained in Sec. 5.1.5, the CSP-IDO algorithm performs better in the impaired hardware scenario than in the ideal hardware scenario. The performance of Method B in both scenarios are very low, showing its weakness w.r.t. noise and impaired hardware.

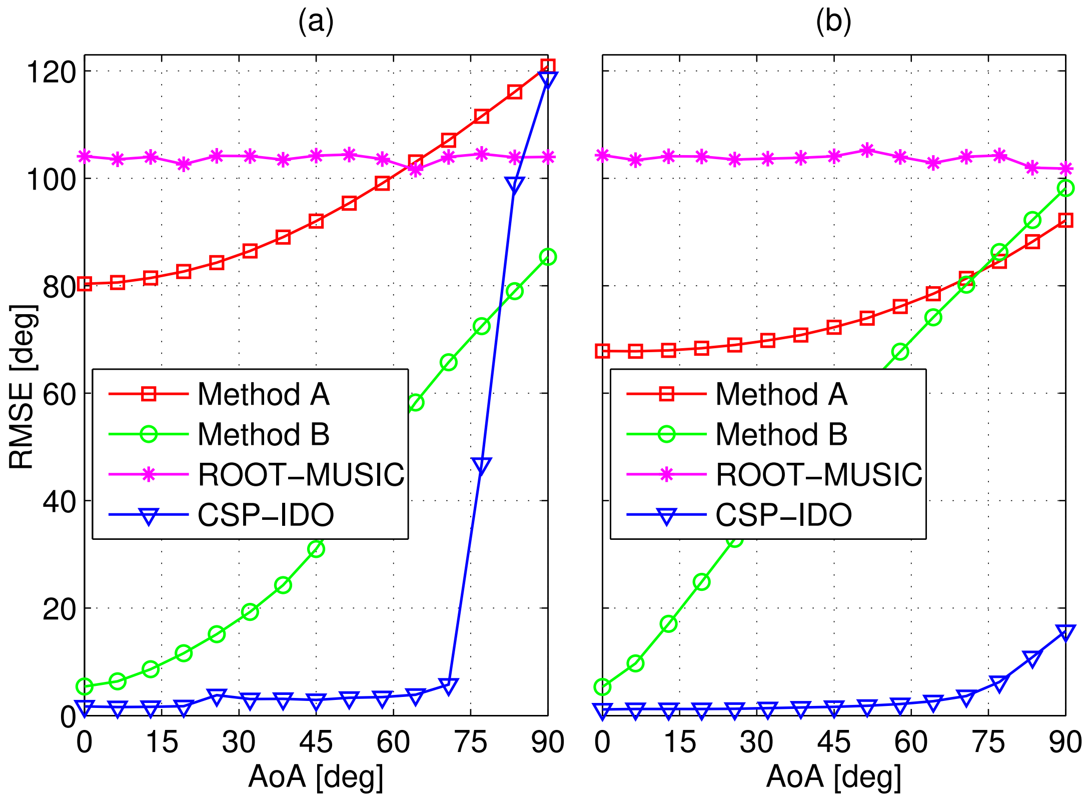

Figure 5.10: RMSE for different AoA. All methods are applied to TSA. (a) Ideal hardware. (b) Impaired hardware.

QAM Statistical Pattern Exploitation for AoA Estimation Using Switched Hardware in Impaired Scenarios

In this Sec. the statistical pattern exploitation technique used in Sec. 5.1.4, namely CSP-IDO [33], is extended to provide a better AoA. A novel method, namely 2D CSP-IDO (BCID), that exploits the full 2D patterns of received signals pdfs is presented. Moreover, the CSP-IDO and BCID performance and robustness in impaired receiving hardware and MP scenarios are analysed.

Introduction

The CSP-IDO method introduced in Sec. 5.1.4 is based on the analysis of the pdfs of the phase of the received signal in (5.13). CSP-IDO exploits the statistical phase pattern of the received signals to estimate the D-PoA and then the AoA. However, in its estimation process, CSP-IDO ignores the full 2D statistical pattern of received signals, see Fig. 5.2, ignoring the modulo part of the statistic (5.17). In this Sec. is proposed an evolution of the CSP-IDO method, namely BCID, that exploits the D-PoA, from the full bi-dimensional statistical pattern of received signals. The same models of received signals and hardware described in (5.12) are herein considered. The expression in (5.15) shows that the bi-dimensional patterns of the pdfs $f^{(1)}_{M\text{-QAM}}$ and $f^{(2)}_{M\text{-QAM}}$ differ for a rotation of their domain of $\Delta\beta$. As $f^{(i)}(\gamma, \rho)$, is herein defined the function that describes the bivariate pdf of the phase jointly to the modulo of the received samples from antenna i. Where, $\gamma^{(i)}_n = \arg\left(y^{(i)}_n\right)$ is the received signal phase and $\rho^{(i)}_n = |y^{(i)}_n|$ its absolute value. Similarly to (5.16), the relation between signals impinging in different antennas is

$$f^{(2)}(\gamma, \rho) = f^{(1)}(\gamma + \Delta\beta, \rho)\,. \tag{5.23}$$

The pdfs $f^{(1)}(\gamma, \rho)$ and $f^{(2)}(\gamma, \rho)$ differ only by an angular circular shift of $\Delta\beta$ of the parameter γ for every value of ρ. Differently than the expression in (5.16) that take in account only the value of γ, the relation in (5.23) is dependant also from the parameter ρ. The CSP-IDO method estimation process in (5.17) and (5.18) can be than generalized using the parameter ρ:

$$\mathcal{C}(\Delta\gamma, \rho) = \int\limits_0^{2\pi} f^{(1)}(\gamma, \rho) f^{(2)}((\gamma - \Delta\gamma) \pmod{2\pi}, \rho) d\gamma\,. \tag{5.24}$$

The correlation $\mathcal{C}(\Delta\gamma, \rho)$ reaches its maximum when $f^{(1)}(\gamma, \rho)$ and $f^{(2)}(\gamma, \rho)$ are overlapped, when $\Delta\gamma = \Delta\beta$. The BCID estimation $\widehat{\Delta\beta}(\rho)$ of the D-PoA $\Delta\beta$ is

$$\widehat{\Delta\beta}(\rho) = \underset{\Delta\gamma \in \Omega_K}{\operatorname{argmax}} \left\{\mathcal{C}(\Delta\gamma, \rho)\right\}\,, \tag{5.25}$$

where the operator $x_{max} = \underset{x}{\operatorname{argmax}}\ p(x)$ returns the argument for which the function is maximum. The interval $\Omega_K = [-K, K]$ is the D-PoA measure interval of the antenna couple that provides unambiguous results. The phase $K = 2\pi d/\lambda_0$ is the maximum D-PoA value measurable by the array.

To understand which ρ values of $\mathcal{C}(\Delta\gamma, \rho)$ provides more informations about the AoA are introduced 3 partial bi-dimensional cross correlations $\mathcal{C}(\Delta\gamma)^{\text{DW}}$, $\mathcal{C}(\Delta\gamma)^{\text{MID}}$ and $\text{UP}(\Delta\gamma)^{DW}$ that describes the lower, middle and higher values of ρ are defined as

$$\begin{aligned} \mathcal{C}(\Delta\gamma)^{\text{DW}} &= \frac{1}{R/3} \int_0^{\frac{1}{3}R} \mathcal{C}(\Delta\gamma, \rho) d\rho\,, \\ \mathcal{C}(\Delta\gamma)^{\text{MID}} &= \frac{1}{R/3} \int_{\frac{1}{3}R}^{\frac{2}{3}R} \mathcal{C}(\Delta\gamma, \rho) d\rho\,, \\ \mathcal{C}(\Delta\gamma)^{\text{UP}} &= \frac{1}{R/3} \int_{\frac{2}{3}R}^{R} \mathcal{C}(\Delta\gamma, \rho) d\rho \end{aligned} \tag{5.26}$$

where the partial bi-dimensional cross correlations introduced in (5.26) are averages of $\mathcal{C}(\Delta\gamma, \rho)$ for different values of ρ. The parameter R represents the maximum value of ρ.

The profiles of $\mathcal{C}(\Delta\gamma)^{\mathrm{DW}}$, $\mathcal{C}(\Delta\gamma)^{\mathrm{MID}}$ and $(\Delta\gamma)^{\mathrm{UP}}$ are compared in the following section.

Numerical Implementation

The pdfs $f^{(i)}(\gamma,\rho)$ analysed in (5.23) and (5.16) are numerically computed implementing a histogram, calculating the relative occurrences of $y_n^{(i)}$ inside a specific cell $\Sigma_{n_{\mathrm{ang}},n_{\mathrm{abs}}}$ of a 2D grid. In particular the grid used to implement the pdfs has polar symmetry to allow a phase shift of the histogram. The grid is composed by $N_{\mathrm{ang}} \cdot N_{\mathrm{abs}}$ cells used to compute the relative frequencies. Each cell $\Sigma_{n_{\mathrm{ang}},n_{\mathrm{abs}}}$ is defined as

$$\underline{/\Sigma_{n_{\mathrm{ang}},n_{\mathrm{abs}}}} \in \left[\alpha_{n_{\mathrm{ang}}-1}, \alpha_{n_{\mathrm{ang}}}\right] , \tag{5.27}$$

$$|\Sigma_{n_{\mathrm{ang}},n_{\mathrm{abs}}}| \in \left[r_{n_{\mathrm{abs}}-1}, r_{n_{\mathrm{abs}}}\right] . \tag{5.28}$$

The histogram grid, depicted in Fig. 5.11 is composed by

- $N_{\mathrm{ang}}+1$ lines with slope $\alpha_{n_{\mathrm{ang}}}$ and passing through the center of the axis that generate N_{ang} circular sectors.
- $N_{\mathrm{abs}}+1$ circles with ray $r_{n_{\mathrm{abs}}}$ and concentric to the center of the axis that generate N_{abs} annuluses.

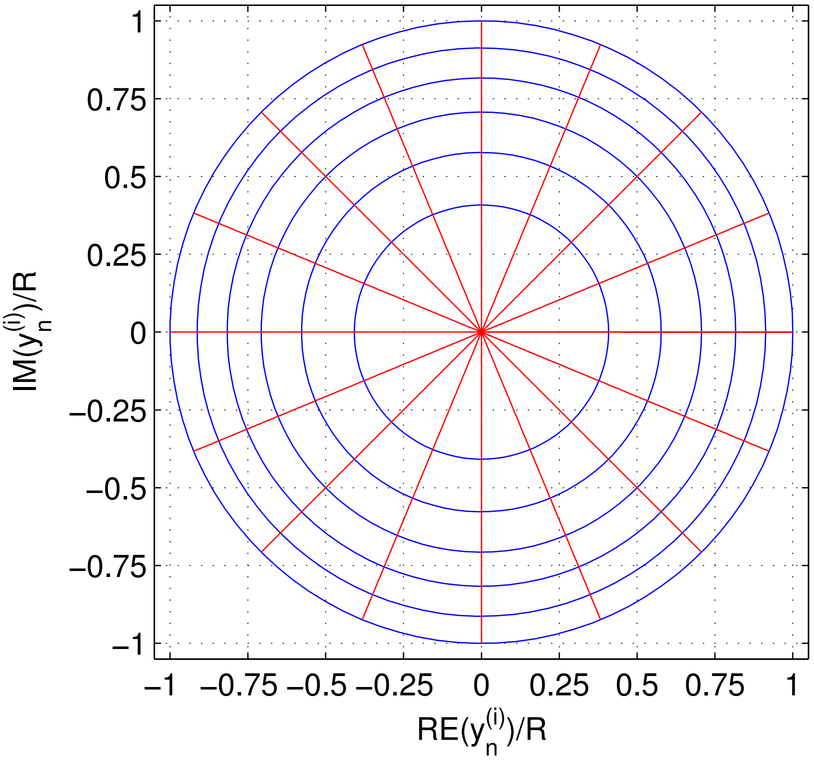

Figure 5.11: Example of histogram grid with $N_{\mathrm{ang}} = 16$ and $N_{\mathrm{abs}} = 6$. Each cell has the same surface.

Each cell has, in general, a surface of $S_{n_\text{ang},n_\text{abs}} = \pi(r^2_{n_\text{abs}} - r^2_{n_\text{abs}-1})/N_\text{ang}$. In order to generate a grid with cells having the same surface $S = \frac{\pi R^2}{N_\text{ang}N_\text{abs}}$, where R is the ray of the external circle of the grid, it is imposed that

$$S_{n_\text{ang},n_\text{abs}} = S\,, \tag{5.29}$$

that leads to

$$\alpha_{n_\text{ang}} = -pi + \frac{2\pi}{N_\text{ang}} n_\text{ang} \qquad n_\text{ang} \in [0, 2, \dots, N_\text{ang}]\ , \tag{5.30}$$

$$r_{n_\text{abs}} = \sqrt{\frac{N_\text{ang}}{\pi} S + r^2_{n_\text{abs}}} \qquad n_\text{abs} \in [0, 2, \dots, N_\text{abs}]\ , \tag{5.31}$$

where $r_0 = 0$ and $r_{N_\text{abs}} = R$. An example of a polar grid used to estimate the pdfs $f^{(i)}(\gamma, \rho)$ following the rules in (5.31) and (5.30) is visible in Fig. 5.11.

If N_{acq} samples of $y_n^{(i)}$ are acquired to estimate $f^{(i)}(\gamma, \rho)$ and $N_{n_\text{ang},n_\text{abs}}$ samples fall within the cell defined by $\Sigma_{n_\text{ang},n_\text{abs}}$ than

$$\begin{aligned} &f^{(i)}_{n_\text{ang},n_\text{abs}} := \frac{N_{n_\text{ang},n_\text{abs}}}{N_{acq} S}\,, \\ &f^{(i)}_{n_\text{ang},n_\text{abs}} \approx f^{(i)}\left(-\pi + \frac{2\pi(n_\text{ang} - 1/2)}{N_\text{ang}}, \frac{r_{n_\text{abs}} + r_{n_\text{abs}-1}}{2}\right)\,, \\ &n_\text{ang} \in [0, 2, \dots, N_\text{ang}] \qquad n_\text{abs} \in [0, 2, \dots, N_\text{abs}]\ , \end{aligned} \tag{5.32}$$

where

$$\sum_{n_\text{ang}=1}^{N_\text{ang}} \sum_{n_\text{abs}=1}^{N_\text{abs}} N_{n_\text{ang},n_\text{abs}} = N_{acq}\,. \tag{5.33}$$

Considered the numerical approximation in (5.32) the continuous circular convolution in (5.24) can be computed as follows

$$\begin{aligned} &\mathcal{C}_{n_\text{shift},n_\text{abs}} := \frac{2\pi}{N_\text{ang}} \sum_{n_\text{ang}=0}^{N_\text{ang}-1} f^{(1)}_{n_\text{ang},n_\text{abs}} f^{(2)}_{(n_\text{ang}-n_\text{shift}) \pmod{N_\text{ang}-1}, n_\text{abs}}\,, \\ &\mathcal{C}_{n_\text{shift} n_\text{abs}} \approx \mathcal{C}\left(-\pi + \frac{2\pi(n_\text{shift} - 1/2)}{N_\text{ang}}, \frac{r_{n_\text{abs}} + r_{n_\text{abs}-1}}{2}\right)\,, \\ &n_\text{ang} \in [0, 2, \dots, N_\text{ang}] \qquad n_\text{abs} \in [0, 2, \dots, N_\text{abs}]\ . \end{aligned} \tag{5.34}$$

Given the approximation in (5.34) the D-PoA estimation in (5.25) can be numerically obtained from

$$\widehat{\Delta\beta}_{n_\text{abs}} = -\pi + \frac{2\pi}{N_\text{ang}} \left(\underset{n_\text{shift} \in \tilde{\Omega}_K}{\text{argmax}} \left\{ \mathcal{C}_{n_\text{shift},n_\text{abs}} \right\} - 1/2 \right)\,, \tag{5.35}$$

that leads to N_{abs} D-PoA estimations and where

$$\tilde{\Omega}_K = \left\{ n_{\text{ang}} \in [1, \ldots, N_{\text{ang}}] \text{ s.t. } \left| \alpha_{n_{\text{ang}}} - \frac{\pi}{N_{\text{ang}}} \right| \leq K \right\} , \tag{5.36}$$

that is the set of indexes n_{ang} associated to angles $\alpha_{n_{\text{ang}}}$ that are inside Ω_K. The expression in (5.35) carries out N_{abs} estimations for the D-PoA that, using the formula in (5.21) gives the AoA estimations. To clean the estimations $\widehat{\Delta\beta}_{n_{\text{abs}}}$ from spurious values caused by unwanted factors such as receiver hardware impairments, MP, non AWGN noise or non linearities, a filtering step is applied to obtain $\widehat{\Delta\beta}'_{n_{\text{abs}}}$:

$$\widehat{\Delta\beta}'_{n_{\text{abs}}} = \left\{ \widehat{\Delta\beta}_{n_{\text{abs}}} \text{ s.t. } \left| \widehat{\Delta\beta}_{n_{\text{abs}}} - m_{\Delta\beta} \right| \leq \sigma_{\Delta\beta} \right\} , \tag{5.37}$$

where $m_{\Delta\beta}$ and $\sigma_{\Delta\beta}$ are the average and the standard deviation of $\widehat{\Delta\beta}_{n_{\text{abs}}}$.

Performance Evaluation

In this Sec. the comparison between CSP-IDO and BCID methods in in terms of D-PoA and AoA estimation is made. Where not specified, propagation channel is considered ideal and hardware impairments are not considered. Where not specified, parameters used in this and following Sec. are $M = 64$, SNR = 20dB and $N_{\text{ovr}} = 3$. The acquisition time is $200MT_{\text{symb}}$ for both the TSA and the FPA. However, the hardware used for the CSP-IDO and BCID estimations is the half of other simultaneous methods. The receiving array is composed by $N_a = 2$ antennas located in the y axis at distance $d = \lambda_0/2$. The receiving hardware is considered ideal. Transmitting hardware is considered impaired with the same parameters on Sec. 5.1.5. The TSA is adopted for the CSP-IDO and BCID methods while for the other methods the FPA is adopted.

Performance Evaluation: Ideal Case

In this Sec. the comparison between CSP-IDO and BCID methods in in terms of D-PoA and AoA estimation is made in the ideal scenario, without hardware impairments. As discussed in Sec. 2.5 antenna arrays for AoA purposes must have $d \leq \lambda/2$ to correctly estimate the full range of AoAs from −180° to 180°. However, as introduced in Sec. 5.1.4, the CSP-IDO method that uses QAM constellations to provide the D-PoA estimation narrows the minimum inter element distance to $d \leq \lambda/8$ in the ideal case. To evaluate how these constraints influence the AoA estimation using the BCID method in Fig. 5.12 and Fig. 5.13 are depicted the 2D cross correlation functions introduced in (5.24). In particular $\mathcal{C}(\Delta\gamma, \rho)$ is represented in polar coordinates as a function of the AoAs $\theta = \arcsin(-\Delta\gamma/K)$ reversing the rule in (5.21) for all D-PoAs $\Delta\gamma$:

$$\mathcal{C}(-K \sin\theta, \rho) \, . \tag{5.38}$$

In Fig. 5.12 $\mathcal{C}$ is depicted in polar coordinates as a function of the AoA in the configuration $d \leq \lambda/2$ that leads to $K = \pi$. The Fig. 5.12 illustrates in $\mathcal{C}$ 4 spurious peaks caused by the D-PoA periodicity that leads to an ambiguous estimation of the AoA for CSP-IDO and BCID. The reduction of the inter-element distance, namely $d \leq \lambda/8$, that leads to $K = \pi/4$ produce an unambiguous estimation of the AoA as visible in Fig. 5.13.

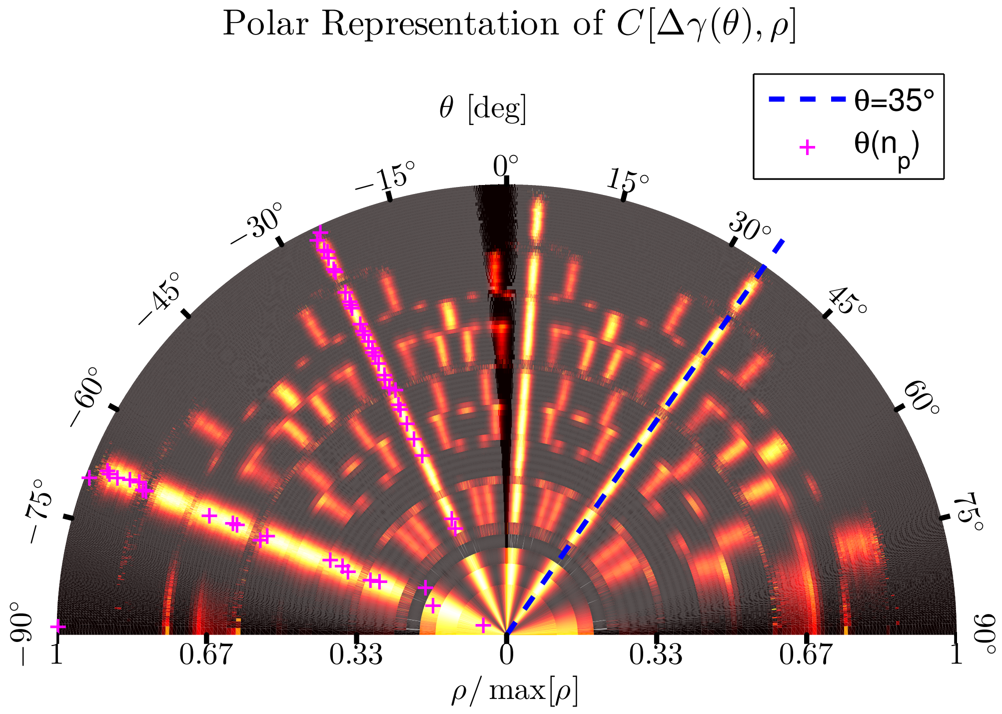

Figure 5.12: Polar representation of $C(\Delta\gamma(\theta_0), \rho)$. Ideal hardware at transmitter side. $K = 180°$.

InFig. 5.15 and Fig. 5.14 are depicted the partial BCID correlation functions introduced in (5.26). As discussed previously, the ambiguity of the case with $K = \pi/2$ w.r.t. the case with $K = \pi/8$ is evident by the 4 peaks carried out by the cyclic correlations in Fig. 5.14 w.r.t. the single peak in Fig. 5.15. It is visible in both Fig. 5.14 and Fig. 5.15 how in the ideal case analysed in this Sec. $C(\rho)^{\mathrm{UP}}$ provides a betted ratio between the maximum correlation peak positioned in $\Delta\beta$ and the other spurious peaks located in the cyclic correlations tails.

Performance Evaluation: Impaired Transmitter Case

In this Sec. the comparison between CSP-IDO and BCID methods in terms of D-PoA and AoA estimation is made in the scenario where the transmitter's hardware is impaired. Propagation channel is considered ideal and receiver's hardware impairments are not considered. In Fig. 5.16 is depicted the polar representation of the 2D BCID circular

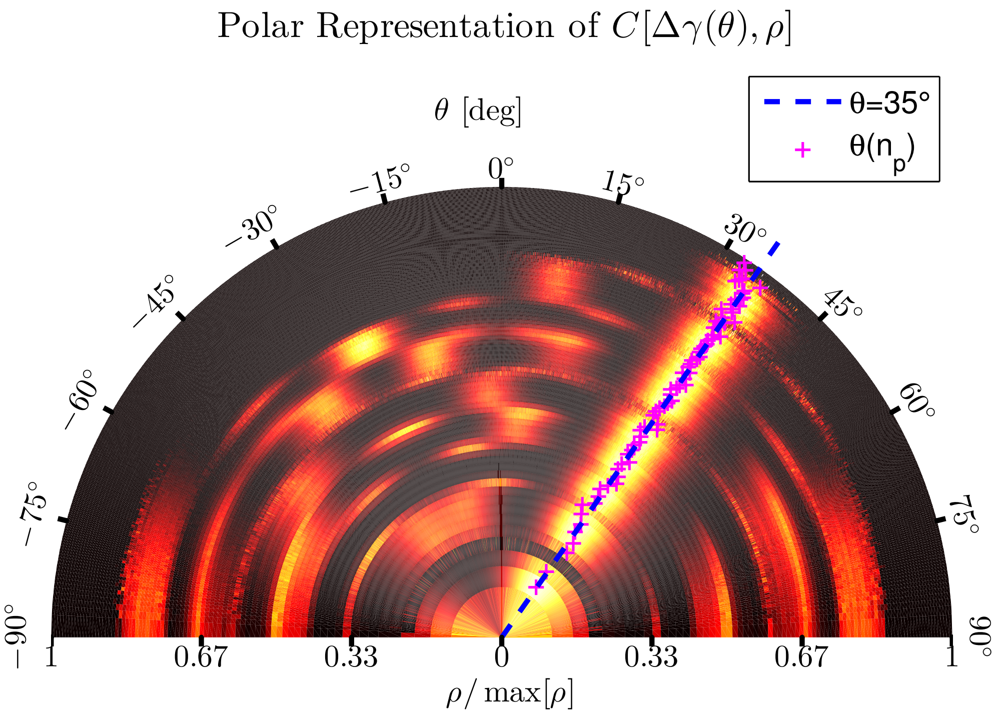

Figure 5.13: Polar representation of $C(\Delta\gamma(\theta_0), \rho)$. Ideal hardware at transmitter side. $K = 45°$.

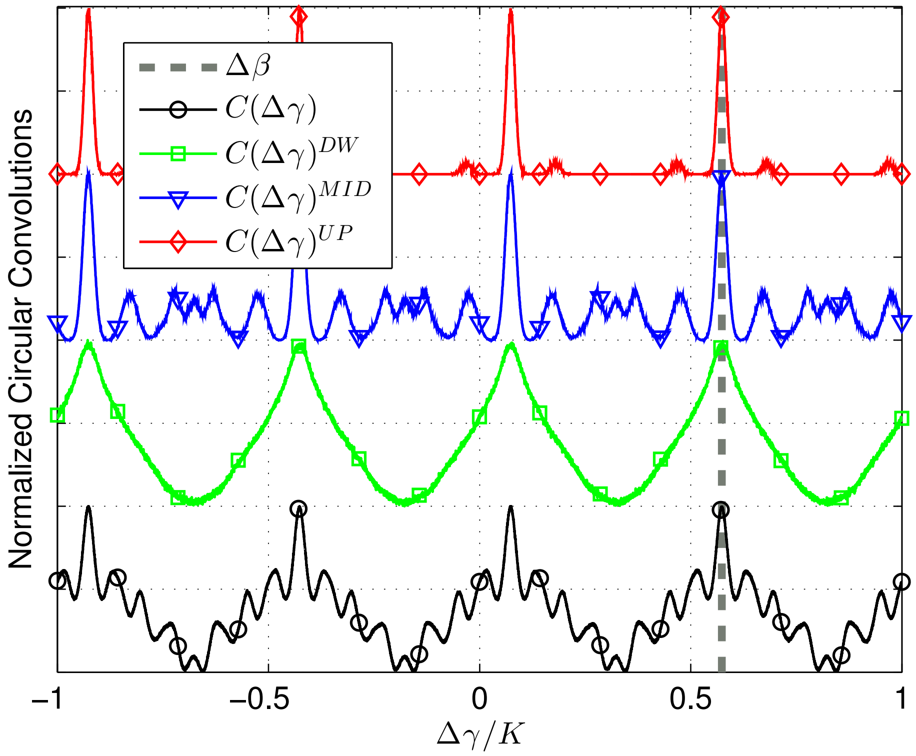

Figure 5.14: Comparison between circular correlations. Ideal hardware at transmitter side. $K = 180°$.

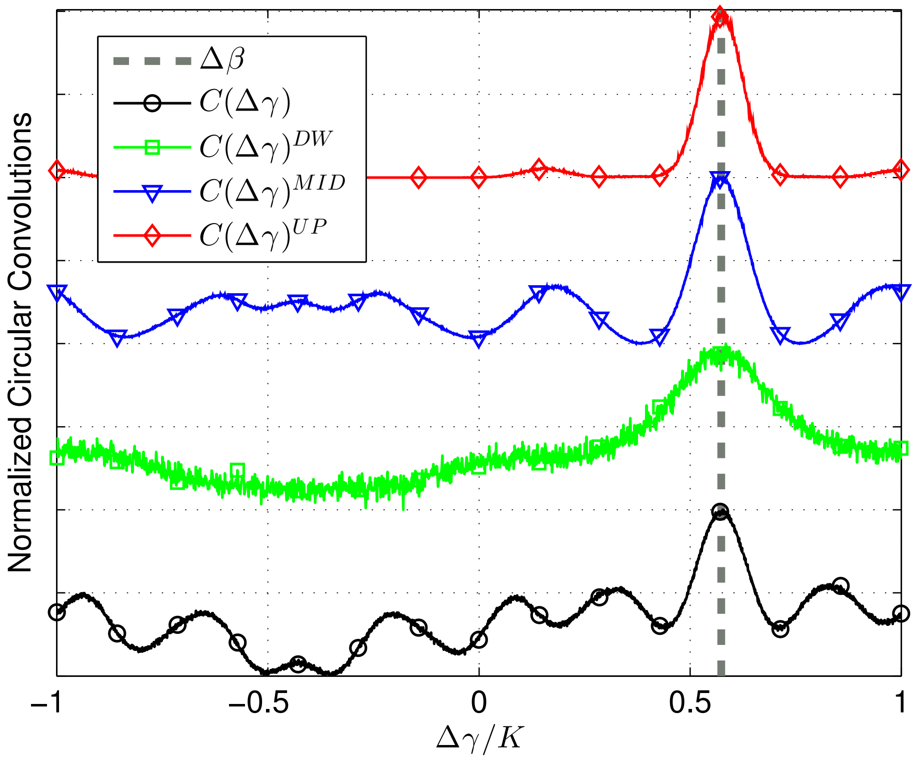

Figure 5.15: Comparison between circular correlations. Ideal hardware at transmitter side. $K = 45°$.

correlation introduced in (5.24) in terms of AoA θ in the impaired transmitter scenario. Comparing the ideal correlation in Fig. 5.13 with the impaired one in Fig. 5.16 it is evident how the transmitter impairments effects on the constellation introduced in Sec. 3 do not affect significantly the correlation. Furthermore, despite the detrimental effects of the impaired transmitter, the impaired circular correlation has lower spurious side lobes. In Fig. 5.17 are depicted the partial circular correlations introduced in (5.26) in the impaired transmitter scenario. Comparing them with the ideal ones in Fig. 5.15 it is possible to notice how $\mathcal{C}(\Delta\gamma)^{\mathrm{UP}}$ is unchanged, $\mathcal{C}(\Delta\gamma)^{\mathrm{MID}}$ has a better peak-to-side lobes ratio and $\mathcal{C}(\Delta\gamma)^{\mathrm{DW}}$ is less noisy. In Fig. 5.18 is depicted the RMSE$(\theta, \tilde{\theta})$ regarding the AoA estimation $\tilde{\theta}$ (5.22) as a function of the real AoA θ comparing the ideal case with the impaired transmitter case. Performance analysis in Fig. 5.18 shows the behaviour of CSP-IDO and BCID in the scenario with ideal channel, ideal transmitter and ideal receiver, in Fig. 5.18.(a), and impaired transmitter in Fig. 5.18.(b).

Performance analysis in Fig. 5.18 shows how, in general, the BCID and the CSP-IDO perform similarly in a broad range of AoAs. In particular the circular correlation used for the D-PoA estimation is $\mathcal{C}(\Delta\gamma)^{(\mathrm{UP})}$ introduced in (5.26). Both methods perform better than method A because of the PO system impairment introduced in Sec. 3.6.

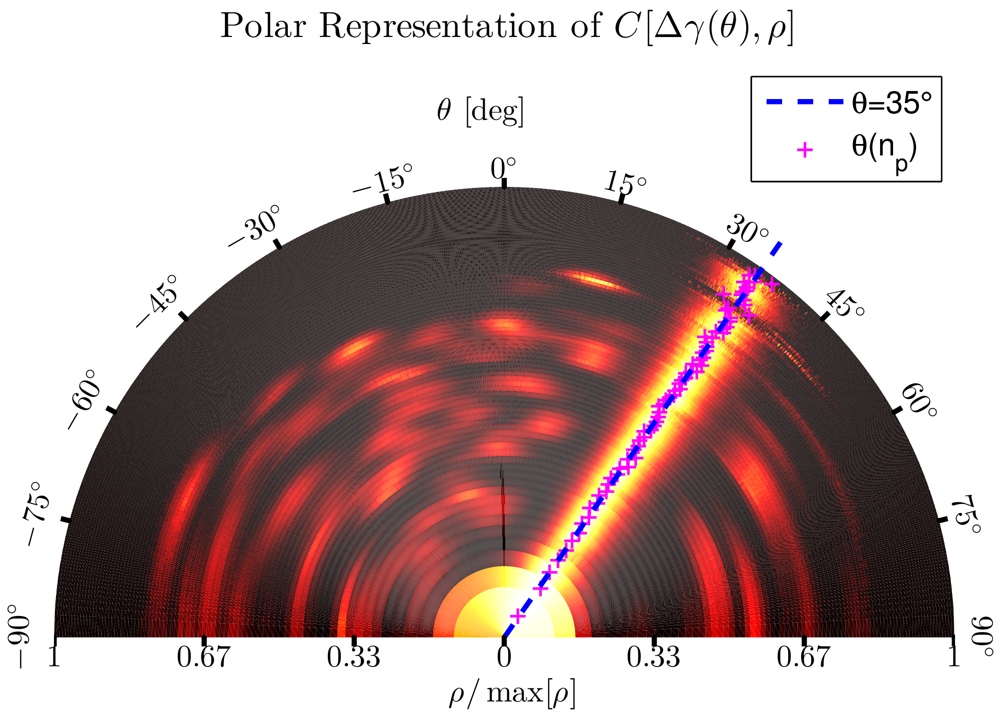

Figure 5.16: Polar representation of $C(\Delta\gamma(\theta_0), \rho)$. Impaired hardware at the transmitter side. $K = 45°$.

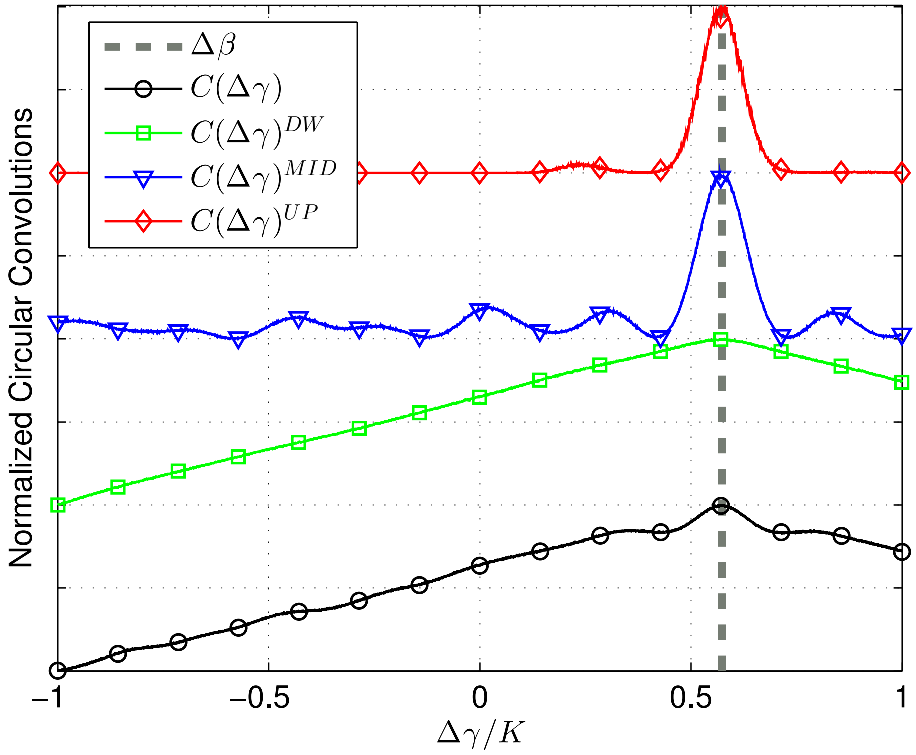

Figure 5.17: Comparison between circular correlations. Impaired hardware at the transmitter side. $K = 45°$.

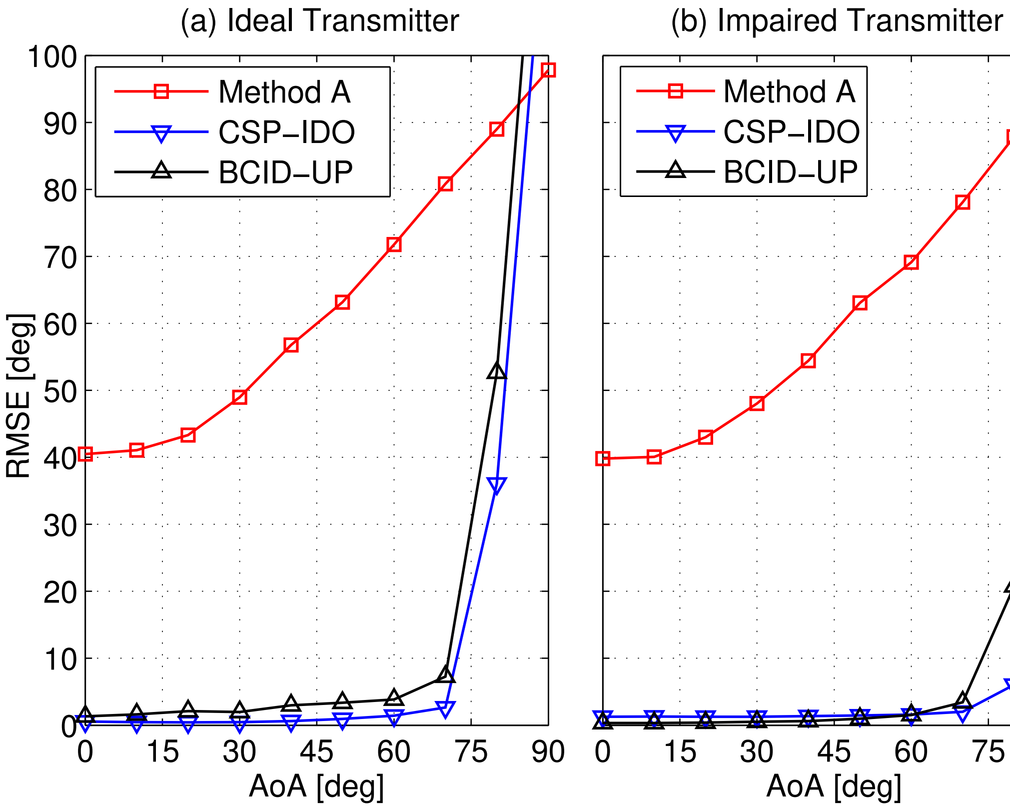

Figure 5.18: RMSE$(\theta, \tilde{\theta})$ as a function of θ.(a) Ideal transmitter case. (b) Impaired transmitter case.

Performance Evaluation: Impaired Receiver Case

In this Sec. the comparison between CSP-IDO and BCID methods in terms of D-PoA and AoA estimation is made in the scenario where the receiver's hardware is impaired. Propagation channel is considered ideal. In Fig. 5.19 is depicted the polar representation of the 2D BCID circular correlation introduced in (5.24) in terms of AoA θ in the impaired receiver scenario. Comparing the ideal correlation in Fig. 5.13 with the impaired one in Fig. 5.19 it is evident how the receiver impairments affect the circular correlation widening the main lobe and increasing the noise floor. In Fig. 5.20 are depicted the partial circular correlations introduced in (5.26) in the impaired receiver scenario. Comparing them with the ideal ones in Fig. 5.15 it is possible to notice how $\mathcal{C}(\Delta\gamma)^{\mathrm{UP}}$, $\mathcal{C}(\Delta\gamma)^{\mathrm{MID}}$ and mostly $\mathcal{C}(\Delta\gamma)^{\mathrm{DW}}$ have wider and more noisy lobes. In Fig. 5.21 is depicted the RMSE$(\theta, \tilde{\theta})$ of BCID and CSP-IDO methods regarding the AoA estimation $\tilde{\theta}$ (5.22) as a function of the real AoA θ comparing the ideal case with the impaired receiver case. Performance analysis in Fig. 5.21 show the behaviour of CSP-IDO and BCID in the scenario with ideal channel, impaired transmitter and ideal receiver, in Fig. 5.21.(a), and impaired receiver in Fig. 5.24.(b). Performance analysis in Fig. 5.21 shows how, in general, the BCID method performs better than CSP-IDO. In particular, the circular correlation used for the D-PoA estimation is $\mathcal{C}(\Delta\gamma)^{(\mathrm{UP})}$ introduced in (5.26). The performance depicted in Fig. 5.21.(a),

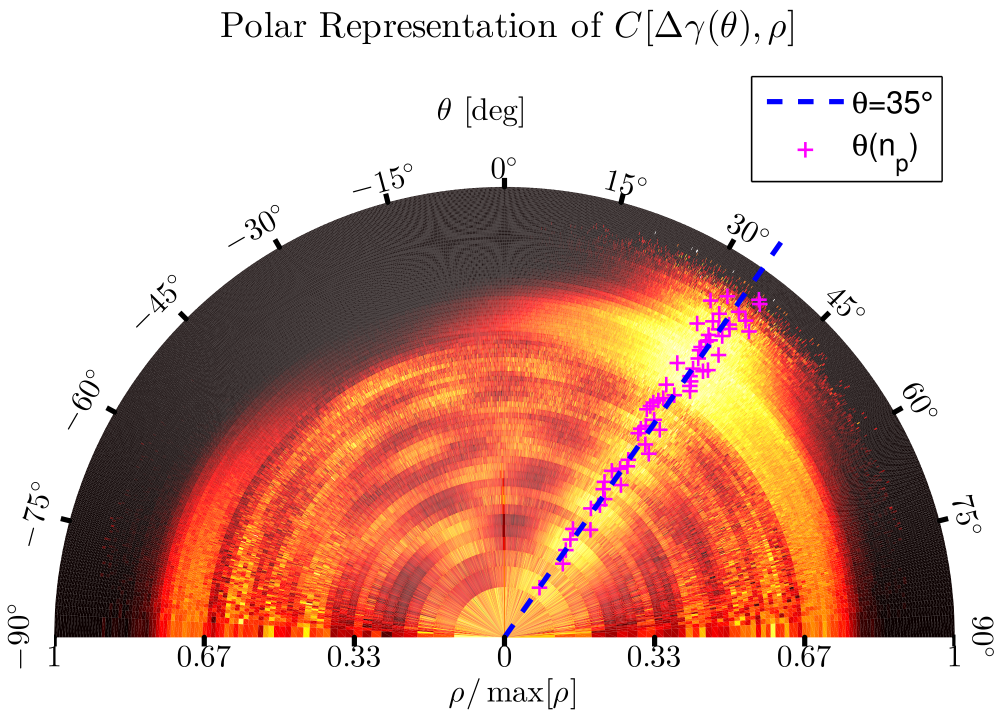

Figure 5.19: Polar representation of $C(\Delta\gamma(\theta_0),\rho)$. Impaired hardware at the receiver side. $K = 45°$.

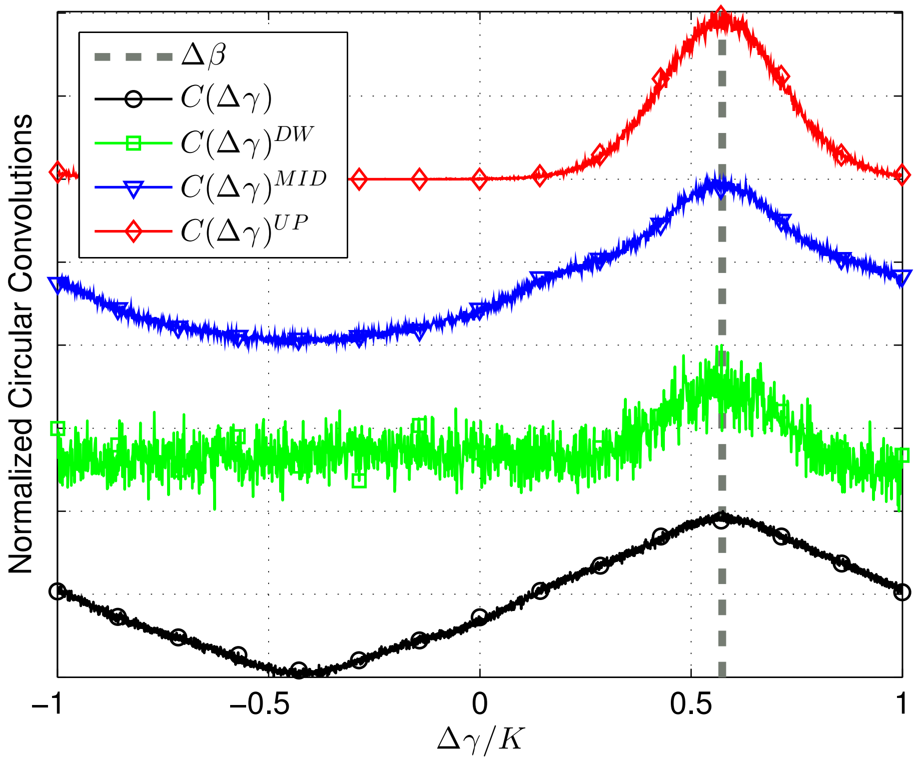

Figure 5.20: Comparison between circular correlations. Impaired hardware at the receiver side. $K = 45°$.

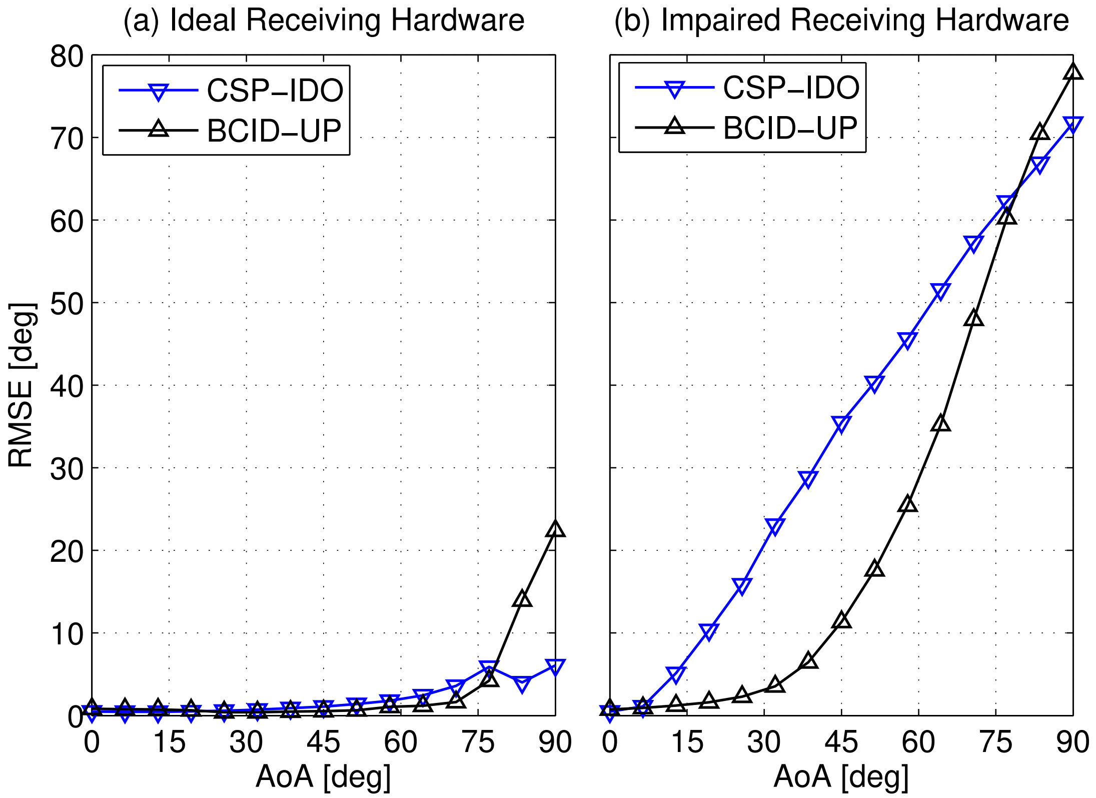

Figure 5.21: RMSE($\theta, \tilde{\theta}$) as a function of θ. Impaired hardware at the transmitter.(a) Ideal receiver case. (b) Impaired receiver case.

that are obtained with impaired transmitter and ideal receiver, show better performance of BCID w.r.t. CSP-IDO under 75deg. The performance depicted in Fig. 5.21.(b), that are obtained with impaired transmitter and impaired receiver, show better performance of BCID w.r.t. CSP-IDO for all AoA range, showing that BCID is considerably more robust to receiver impairments w.r.t. CSP-IDO, mostly under 45deg.

Performance Evaluation: Multi-path (MP) Case

In this Sec. is analysed how the effects of the MP channel introduced in Ch. 4 affects of the CSP-IDO and the BCID AoA estimations. The considered channel is generated by N_p' scatters, each one forms the channel as its n_p-th impulse. The n_p impulse is temporary located in n_pT_p where T_p is the US-CIR sampling period. The amplitude of the scatterers impulses on the channel expression are

$$|h_{n_p}^{(n_a)}| = e^{-\frac{\tau_0 + n_p T_p}{\tau_{\text{norm}} T_{\text{symb}}}} \; \forall n_a \in 1, 2\,, \tag{5.39}$$

where τ_{norm} is the channel characteristic length expressed as multiple of T_{symb}. The parameter τ_0 is the ToA of the LOS component. The formal length of the channel is considered to be $5\tau_{\text{norm}}T_{\text{symb}}$, after that time the channel amplitude is considered to be 0. This assumption leads to the a maximum number of scatterers of $N_p = 5\tau_{\text{norm}}T_{\text{symb}}/T_p - 1$, excluding the LOS impulse. Only a random subset of $N_p' \leq N_p$ scatterers is considered, that scatterers have the amplitude described in (5.39). The channel phases related to each antennas are obtained following the equations in Sec. 4.4.2. To evaluate how these constraints influence the AoA estimation using the BCID method in Fig. 5.22 is depicted the 2D cross correlation functions introduced in (5.24). In particular the $\mathcal{C}(\Delta\gamma, \rho)$ is represented in polar coordinates as a function of the AoAs $\theta = \arcsin(-\Delta\gamma/K)$ reversing the rule in (5.21) for all D-PoAs. In Fig. 5.24 is depicted the RMSE$(\theta, \tilde{\theta})$ regarding the

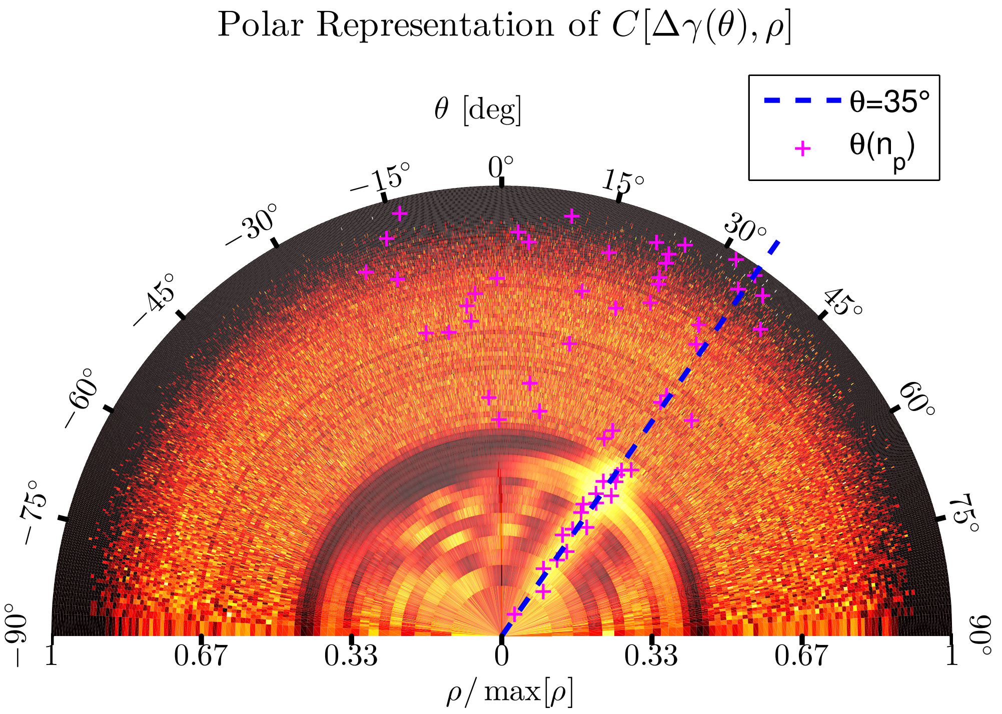

Figure 5.22: Polar representation of $C(\Delta\gamma(\theta_0), \rho)$. MP channel, $N_p' = 2$, $\tau_{\text{norm}} = 2$. $K = 45°$.

AoA estimation $\tilde{\theta}$ (5.22) for all methods as a function of the real AoA θ and the value of N_p' considering a MP scenario with $\tau_{\text{norm}} = 2$. The performance analysis in Fig. 5.24 show the behaviour of CSP-IDO and BCID in the scenario with ideal receiver, impaired transmitter and ideal channel, in Fig. 5.24.(a), and MP channel in Fig. 5.24.(b). In the ideal channel scenario ($\tau_{\text{norm}} = 0$), depicted in Fig. 5.24.(a), BCID and CSP-IDO perform similarly under 75deg. In particular the circular correlation used for the D-PoA estimation is $\mathcal{C}(\Delta\gamma)^{(\text{UP})}$ introduced in (5.26). The performance in the MP scenario, depicted in Fig. 5.24.(b), show better performance of BCID w.r.t. CSP-IDO under 30deg and worst for higher values.

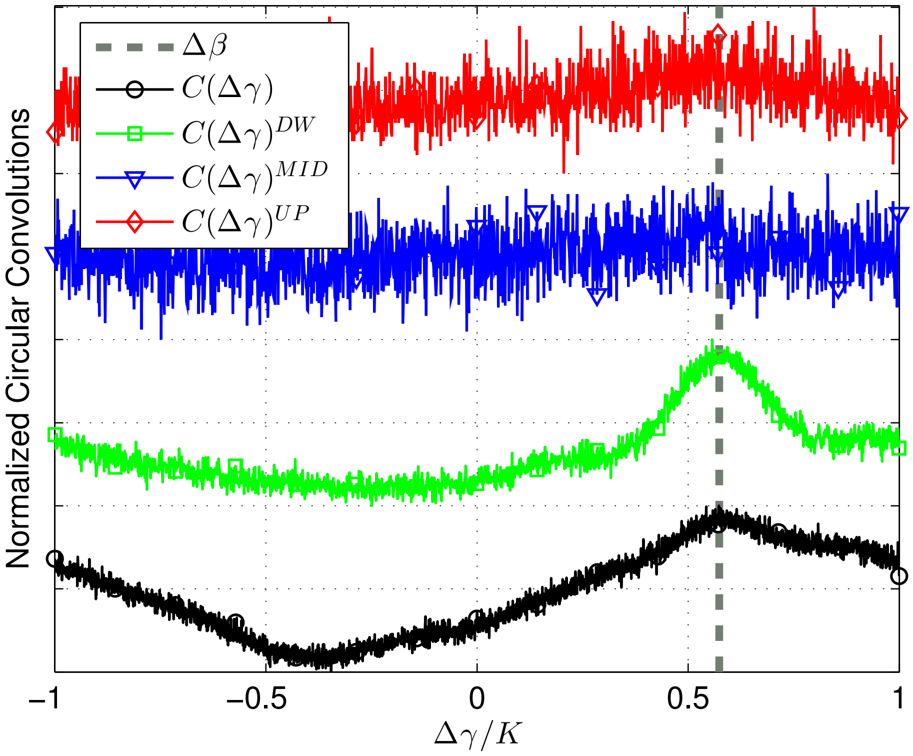

Figure 5.23: Comparison between circular correlations. MP channel, $N'_p = 2$, $\tau_{\text{norm}} = 2$. $K = 45°$.

Conclusions

In this Ch. two novel techniques that estimate the AoA exploiting the statistical proprieties of modulated signals impinging on a generic receiving array have been presented. In particular the pdfs of the received signals have been manipulated to reciprocally overlap their 1D pattern in the CSP-IDO method (Sec. 5.1), or their 2D pattern in the BCID method(Sec. 5.2). The proposed methods are suitable to work with a-simultaneous signal acquisitions from the array sensors, where other simultaneous methods, such as MUSIC-like algorithms, fail to be applied. The proposed algorithms, applied to a TSA at the receiver, provide a substantial reduction of hardware employment w.r.t. simultaneous approaches. Furthermore, CSP-IDO and BCID are able to improve their performance exploiting the transmitter impaired hardware signature. Since the use of the proposed methods exploits the received signals pdfs their application is possible with any type on numerically modulated signals, such as QAM or A-PSK. For this reason CSP-IDO and BCID can also be applied to one or multiple sub-carriers of a multi-carrier modulation system, such as Orthogonal Frequency Division Multiplexing (OFDM), to improve the performance. The performance has been evaluated also in scenarios where the estimation process is affected by MP and impaired hardware at the receiver showing enough robustness. Proposed techniques thanks to their passive/opportunistic approach to AoA

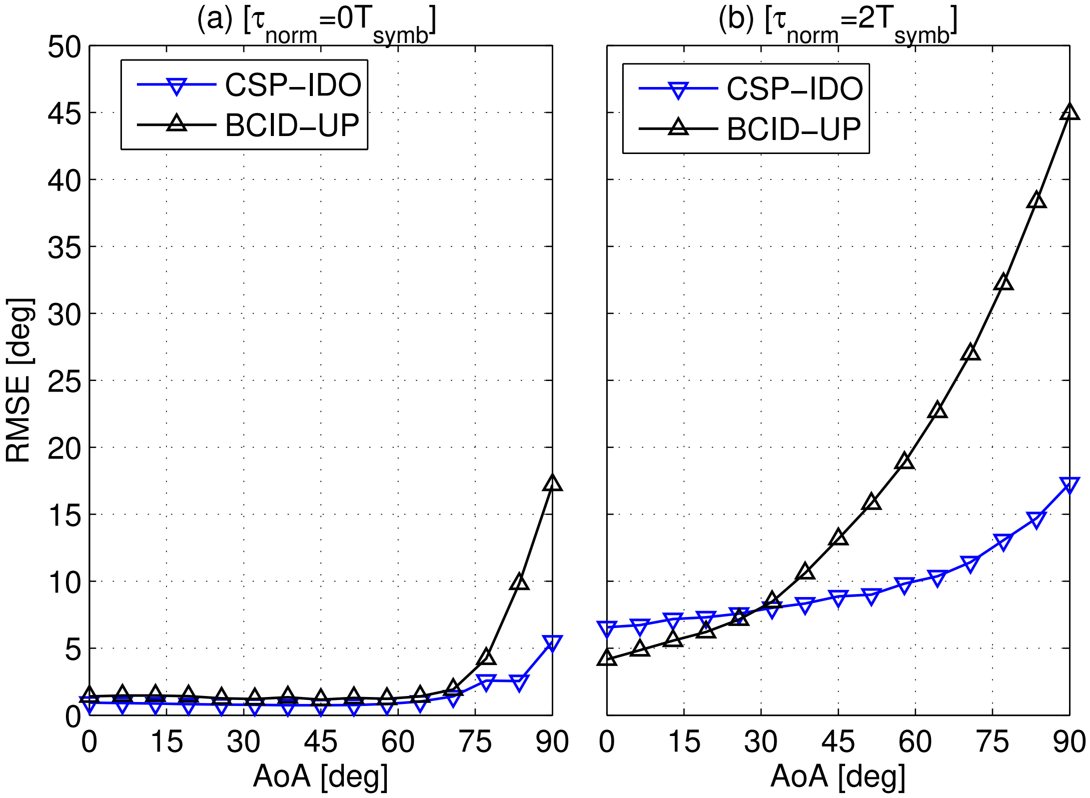

Figure 5.24: RMSE$(\theta, \tilde{\theta})$ as a function of θ in a MP scenario. Impaired hardware at the transmitter. $N_p' = 1$. (a) $\tau_{\text{norm}} = 0$. (b) $\tau_{\text{norm}} = 1$.

localization and thanks to the limited hardware usage are suited to be used in a eavesdropping scenario with low-end hardware.

6 Particle Filtering for Dynamic AoA Estimation

In this Ch. the statistical Particle Filtering (PF) techniques [43] are applied to AoA dynamic tracking. The PF methods, known also as Sequential Monte Carlo (SMC), are techniques designed for the iterative estimation of the hidden state of a dynamic system from the knowledge of a set of incomplete and noisy measures of the system [44]. These methods are herein applied to the dynamic AoA estimation of RF sources that are moving in the 2D or 3D space. In particular in Sec. 6.1 the dynamic 2D AoA tracking of an electric vehicle [93] is implemented through a receiving antenna array. Performance are carried out testing the algorithms in a real case scenario. In Sec. 6.2 the dynamic 3D tracking of a UAV is implemented through a 3 axial array of antennas proposing a UAV tracking system and a UAV auto navigation system in a simulative approach.

Opportunistic Vehicle Tracking

The completion of the IEEE 802.11p standard paves the way for the long awaited deployment of Vehicle-to-Vehicle (V2V) and Vehicle-to-Infrastructure (V2I) communication networks. They will enable the establishment of ad hoc car networks for the diffusion of sensor information and the implementation of a plethora of new services most of which requiring position information. In this respect, Global Positioning System (GPS) based positioning plays an important role. In this Ch. , it is considered a different type of localization method that is based on the usage of roadside localization nodes. The basic idea is to use the IEEE 802.11p infrastructure in a “passive” way trying to enable a positioning service opportunistically listening to V2V and V2I communications. The usage of Road Side Units (RSUs) that detect position information from vehicles is interesting for instance to enable traffic monitoring services for consumer applications like driver assistance or in the emerging technology of self-driving cars. Positioning is performed using an ad hoc multiple antenna receiver that estimates the angle of arrival of the signal impinging the array. To offer good performance particle filtering is deployed for the estimation of the angle-of-arrival and track the position of the vehicles as they move with a broad range of velocities.

Introduction

A vehicular communication network most likely based on IEEE 802.11p [37] will become soon a reality. This will enable the establishment of ad hoc car networks for the diffusion and gathering of sensor information and the implementation of a plethora of new services [38]. Among all possible new applications, the most important ones are probably those that exploit localization information, i.e., context aware services. In this respect, GPS positioning plays an important role in the full development of this ecosystem of services. However, the usage of other localization technologies is relevant in situations where GPS does not fulfil the requirements, e.g., in terms of precision, response time, and coverage. The usage of RSUs) that detect position information from vehicles is interesting for instance to offer a traffic control monitoring service for safety [39] or vehicle flows analysis and management [40], or it can be an enabling service for consumer applications like driver assistance and in the emerging technology of self-driving cars. Furthermore, in such applications the identification of the vehicle can also be useful. GPS itself cannot provide identification information unless it is coupled with another data communication technology. In other cases, the identification of the nodes is not important but the position information cannot be obtained by sharing GPS information using a IEEE 802.11p based network because such information is available only to privileged nodes or is protected for privacy or security issues to other users. Therefore, we herein consider a different type of localization method that exploits an existing vehicular communication network infrastructure (and in particular the IEEE 802.11p network) in an "opportunistic" way trying to obtain the vehicles position, in a certain area, by listening to V2V-V2I communication signals using an RSU. Such an approach can avoid the use of GPS or complement it, provide more accuracy and reliability in certain scenarios. Essentially, this approach is host-based, i.e., it is made directly by the RSU node. We focus on the RSU, its architecture and algorithms. The RSU comprises an array of antennas and estimates the AoA of the signals transmitted by the vehicles that impinge the array. This AoA estimation approach can be challenging because of hardware impairments (as phase noise) and multipath propagation [41]. AoA estimation can be done with subspace methods as the MUSIC algorithm [42] which detect multiple emitters and compensate, in part, multipath effects. In this Ch. instead, we consider first a simple AoA phase differential approach. Then, the AoA estimates are refined using a statistical method based on PF [43]. Particle filtering was proposed originally for iteratively estimate the hidden state of a dynamic system approximating its continuous pdf with a weighted set of M discrete samples [44]. The experimental test bed visible in Fig. 6.1 has been deployed to evaluate algorithm performance.

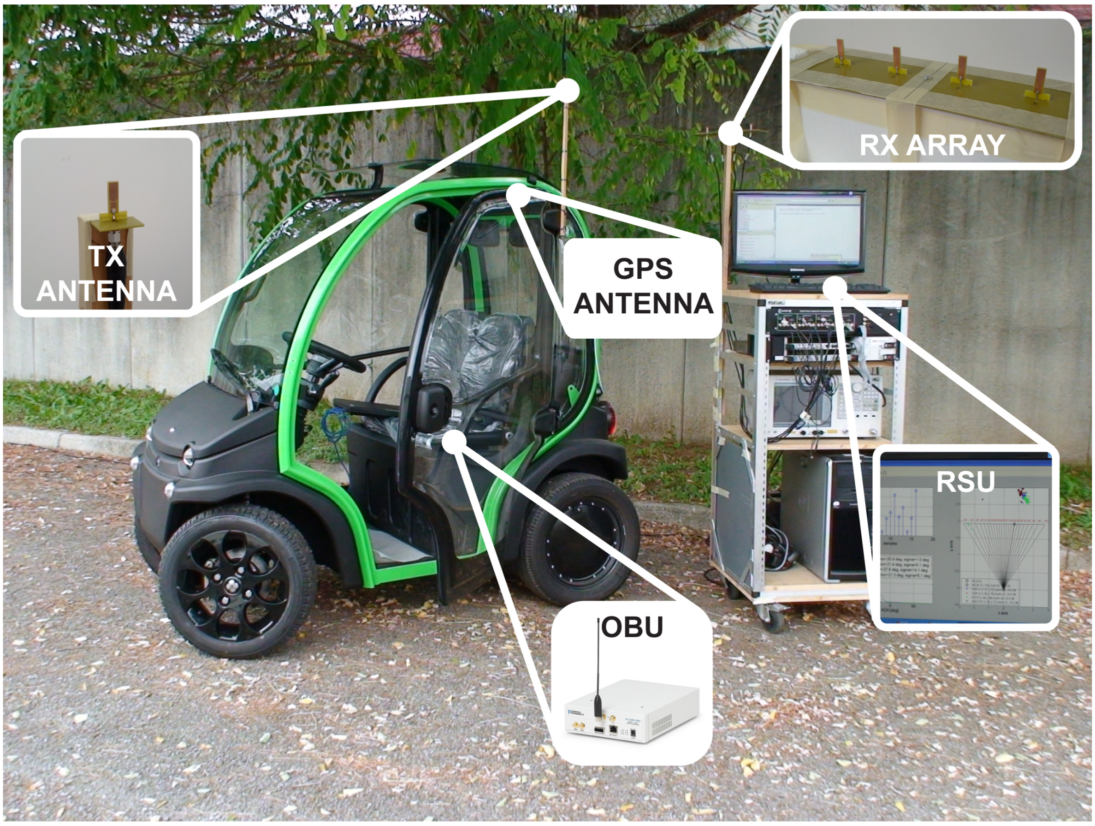

Figure 6.1: Experimental set-up.

AoA Opportunistic Estimation Model

The system herein considered comprises a receiving unit equipped with a D-spaced ($D = \lambda_0$) N_a-elements receiving ULA of antennas ($N_a = 4$). The vehicle to be tracked deploys a transmission unit with a single antenna operating a carrier frequency $f_0 = 1/\lambda_0$. The receiving array is placed along the positive x-axis and the coordinates $[x_i, y_i]$ of the i-th antenna are chosen so that the first one is placed in the center of the axis and the others in $x > 0$:

$$\begin{aligned} y_i &= 0 \qquad & i \in 1, 2, \ldots, N_a, \\ x_i &= (i-1)\lambda_0 \qquad & i \in 1, 2, \ldots, N_a. \end{aligned} \tag{6.1}$$

The moving source antenna is placed in $[x_{src}(t), y_{src}(t)]$ in the $y > 0$ cartesian area. The distance between the source and the i-th antenna is $d_i(t)$. The ToA $\tau_i(t)$ is defined as the time that the transmitted signal takes to go from the source antenna to the i-th receiving antenna. The angle $\alpha_i(t)$ is defined as the phase of the narrowband f_0 frequency signal sent from the source antenna and impinging into the i-th receiving array antenna:

$$d_i(t) = \sqrt{(x_i - x_{src}(t))^2 + (y_i - y_{src}(t))^2}, \tag{6.2}$$

$$\tau_i(t) = d_i(t)/c_0, \tag{6.3}$$

$$\alpha_i(t) = 2\pi f_0 \tau_i(t). \tag{6.4}$$

A set of polar coordinates $[r(t), \theta(t)]$ is defined to locate the source, where $r(t)$ is the distance from the center of the axis and $\theta(t)$ is the angle from the positive y axes. Under the far field approximation $r(t) >> L_{array} = (N_a - 1)\lambda_0$, it is possible to obtain for each pair of antennas an estimation of the AoA $\theta(t)$. With these assumptions and without impairments and noise, each pair of antennas obtains the same estimation of the AoA $\tilde{\theta}(t)$:

$$\begin{aligned} \tilde{\theta}(t) &= \arccos\left\{\frac{\Delta\alpha(t)}{K}\right\}, \\ \Delta\alpha(t) &= \alpha_i(t) - \alpha_{i+1}(t), \end{aligned} \tag{6.5}$$

where $\Delta\alpha_i(t)$, $\forall i \in \{1, 2, \ldots, N_a - 1\}$, is the differential phase shift introduced in (6.4) between the signals received from the i-th and the $(i+1)$-th antenna of the ULA. K is defined as the constant $K = \frac{2\pi f_0 D}{c_0} = 2\pi$. Differential phase shift informations need to be extracted from the received demodulated signals in the application scenario described by the model in (6.5). The transmitted signal $s(t)$ representing the signal transmitted in the V2V and V2I (V2X) communication by the moving vehicle is

$$s(t) = a(t)e^{j(2\pi f_0 t + \phi_0)}, \tag{6.6}$$

where ϕ_0 is the phase of the source signal and $a(t)$ is the complex envelope of the data signal. The demodulated and sampled signal received at the i-th antenna is

$$z_i(kT) = A_i(kT)a(kT)e^{j(\phi_0 + \alpha_i(kT))} + w_i(kT), \tag{6.7}$$

where $A_i(kT)$ is the channel PL and $\alpha_i(kT)$ is the phase shift defined in (6.4) caused by the distance $d_i(kT)$ between the signal source and the i-th antenna of the ULA. $w_i(kT)$ is the sampled AWGN process at the i-th receiver. The expression in (6.7) is simplified and does not take in account non ideal conditions like multipath effects and other hardware impairments [41]. The received samples are processed to compute an estimation of $\Delta\alpha(kT)$ in order to estimate the AoA $\tilde{\theta}(kT)$ like previously expressed in (6.5):

$$\Delta\alpha(kT) \approx \underline{/\bar{q}(kT)}, \tag{6.8}$$

$$\bar{q}(kT) = \sum_{i=1}^{N_a - 1} \frac{q_i(kT)}{N_a - 1}, \tag{6.9}$$

$$\begin{aligned} q_i(kT) &= z_i(kT)z_{i+1}^*(kT) = \\ &= A_i(kT)A_{i+1}(kT)|a(kT)|^2 e^{j\Delta\alpha_i(kT)} + \eta_i(kT), \end{aligned} \tag{6.10}$$

where the approximation in (6.8) is due to the zero mean $\eta_i(kT)$ component shown in (6.10) that includes $w_i(kT)$ and $w_{i+1}(kT)$ AWGNs and their cross products with the data signals. The $(N_a - 1)$-long average operation in (6.8) reduces the effects of the zero mean noise $\eta_i(kT)$. $A_i(kT)$ and $A_{i+1}(kT)$ are real positive numbers that represent the path loss (PL) factors associated to the pair of antennas.

Using this technique a roadside relative positioning is possible without interacting directly with the vehicle using for example IEEE 802.11p but just opportunistically exploiting the information from the V2X communication. In (6.8), the AWGN is averaged between antenna pairs for better performance.

The effects of hardware impairments and multipath propagation introduce a performance loss [41]. Although not explicitly modelled in (6.7) they are taken into account in the performance results section. Their compensation is performed at a higher level with the PF algorithm described in Sec. 6.1.3 and 6.1.4.

Particle Filtering Algorithm

In this section, we discuss how PF is applied to the localization problem introduced in Sec. 6.1.2. The algorithm target is to track the hidden state of the system, the real angular position of the signal source $\theta_k = \theta(kT)$, from the noisy measure of the system represented by $\tilde{\theta}_k = \tilde{\theta}(kT)$. This system can be represented by two discrete time expressions, one that shows the evolution of the hidden state θ_k and another that shows how the system outputs, the measures $\tilde{\theta}_k$, are generated:

$$\theta_k = g(\theta_{[k-N_{mm} \div k-1]}, u_{k-1}), \tag{6.11}$$

$$\tilde{\theta}_k = h(\theta_k, v_k), \tag{6.12}$$

where the index k denotes the signal at time kT. In (6.11) is shown how the current state θ_k evolves only thanks to its N_{mm} previous values and a random uncertain variable u_{k-1} through the motion model function g. Equation (6.12) shows how the generated measure $\tilde{\theta}_k$ depends only on the real state θ_k and a random uncertain variable v_k through the measure model function h. This Monte Carlo based type of Markov chain hidden state estimation algorithm has been chosen because of its relative simplicity of application an its versatility achievable by appropriately setting the parameters and procedures. PF algorithms are a numeric implementation of Bayesian estimation, a statistical approach to increase iteratively the knowledge of θ_k by narrowing $f_{\theta_k|\tilde{\theta}_k}[a]$, its pdf conditioned by the sequential acquisition of new informations during time. The pdf of θ_k defined as $f_{\theta_k}[a]$ is approximated with a set of M particles $\{\theta_k^{(m)}\}_{m=1,\dots,M}$ and a set of related weights $\{w_k^{(m)}\}_{m=1,\dots,M}$:

$$\{\theta_k^{(m)}, w_k^{(m)}\}_{m=1,\dots,M} \leftrightarrow f_{\theta_k}[a], \tag{6.13}$$

where the rule that leads to the particles set generation is

$$E[\theta_k] = \int_{-\pi/2}^{\pi/2} a f_{\theta_k}[a]\, da = \sum_{m=1}^{M} \theta_k^{(m)} w_k^{(m)}. \tag{6.14}$$

The particles $\theta_k^{(m)}$ and the weights $w_k^{(m)}$ are generated from the partial knowledge of the measure model h and the state evolution model g, this knowledge is more and more corrected by the sequential time acquisition of the values of the measures $\tilde{\theta}_k$. Furthermore the signal source is moving so that its AoA changes over time with its measures.

Random Particle Initialization

The particles initialization is the first step of the procedure. In this stage the knowledge of the hidden state is shallow. At first it is only known that θ_k is between $-\pi/2$ and $+\pi/2$, so the first M particles are uniformly randomly generated in this interval:

$$\theta_{k=1}^{(m)} \sim U\left(-\frac{\pi}{2}, +\frac{\pi}{2}\right). \tag{6.15}$$

Particle Measures Generation

Particle measures $\tilde{\theta}_k^{(m)}$ are calculated in every iteration after the generation of the corresponding particles $\theta_k^{(m)}$. An hypothesized measure model $\tilde{h}$ is created to approximate the real one introduced in (6.12).

$$\begin{aligned} &\tilde{\theta}_k^{(m)} = \tilde{h}(\theta_k^{(m)}, v_k^{(m)}) = \theta_k^{(m)} + v_k^{(m)}, \\ &v_k^{(m)} \sim N\left(m_v = 0, \sigma_v\right), \end{aligned} \tag{6.16}$$

where σ_v is the standard deviation of the normal distribution of $v_k^{(m)}$ that defines how wide the measurement error is.

Weight Calculus

An Euclidean distance metric is used, after the generation of the particle measures $\tilde{\theta}_k^{(m)}$, to calculate their weights $w_k^{(m)}$:

$$\begin{aligned} &d_k^{(m)} = |\tilde{\theta}_k^{(m)} - \tilde{\theta}_k|, \\ &w_k^{(m)} = \exp\left\{-d_k^{(m)}\right\}, \end{aligned} \tag{6.17}$$

where $\tilde{\theta}_k^{(m)}$ are the statistically generated particle measures introduced in (6.16), $\tilde{\theta}_k$ is the real acquired measure at time k introduced in (6.10) and $d_k^{(m)}$ is defined as the weight parameter.

Estimation

After that the set of weights $\{w_k^{(m)}\}_{m=1,\dots,M}$ and particles $\{\theta_k^{(m)}\}_{m=1,\dots,M}$ at time kT is generated, it is possible to process $\hat{\theta}_k$, i.e., the PF estimation of the AoA θ_k:

$$\hat{\theta}_k = \sum_{m=1}^{M} \theta_k^{(m)} w_k^{(m)}. \tag{6.18}$$

The method in (6.18) calculates the weighted average of the discrete set of particles.

Resampling

During the processing of the weights, depending on the weighting function used, it is possible that a subset P_{small} of particles assumes a non significant weight $w_{small} \approx 0$ that makes them useless in their contribution to the the estimation calculus. On the other hand a complementary subset P_{big} is generated. It includes particles with the highest weights $w_{big} \approx 1/|P_{big}|$ and concentrated in a single point θ_{big}. This particle cloud degeneration makes the discrete particle approximated pdf turn into an impulse centred in θ_{big}. That phenomenon carried on by the iterations reduce the precision of the algorithm decreasing also its ability to dynamically follow θ_k.

A solution to avoid this phenomenon is to re-sample the set of particles [96]. This new set $\{\theta_{k,res}^{(m)}\}_{m=1,\dots,M}$ is generated choosing the particles from the original set $\{\theta_k^{(m)}\}_{m=1,\dots,M}$ and extracting them proportionally to their weight $w_k^{(m)}$:

$$P[\theta_{k,res}^{(m)} = \theta_k^{(n)}] \propto w_k^{(n)}. \tag{6.19}$$

This technique avoids the degeneration of the particle cloud keeping the consistency.

Motion Model Feedback

After the regularization of the particle cloud shown in Sec. 6.1.3, it is necessary to iterate the algorithm from the step k to the step $k+1$ creating a feedback among the cycles. Depending on the tracked variable it is possible to create a motion model inferring the coordinates of the particles set $\{\theta_{k+1}^{(m)}\}_{m=1,\dots,M}$ from the parameters of the previous iterations. The most simple motion model is to place $\theta_{k+1}^{(m)}$ near the re-sampled value $\theta_{k,res}^{(m)}$ to obtain:

$$\theta_{k+1}^{(m)} = \theta_{res,k}^{(m)} + \gamma, \tag{6.20}$$

where γ is a zero mean random variable distributed as $\gamma \sim N(0, \sigma_s)$.

Proposed Particle Filtering Improvements

In this section, we present two improvements of the basic particle filtering of Sec. 6.1.3.

Weight Reshaping

In Sec. 6.1.3, the positive effects of re-sampling have been discussed. However, the abuse of this technique can make the group of particles to collapse in a single area reducing dramatically the quality of the simulation. To avoid this consequences, [43] shows that it is possible to trigger the re-sampling in every iteration evaluating if the parameter that represents the spread of the particle cloud exceeds a certain degeneration threshold. In this Ch. , an alternative method is proposed. Essentially, the re-sampling is always computed without restrictions but it is preceded by an elaboration block that we call weight reshaping (RESH). The values of the weight parameter $d_k^{(m)}$ introduced (6.17) are processed in a way that their biggest value is associated to a new weight w^{min} and similarly the smallest weight parameter is associated to $w^{max} = rw^{min}$:

$$\begin{aligned} w_{min} &= \mathcal{R}\left(\max\left\{d^{(m)}\right\}\right), \\ w_{max} &= \mathcal{R}\left(\min\left\{d^{(m)}\right\}\right). \end{aligned} \tag{6.21}$$

As shown in Fig. 6.2, the particles' weights that are between this values are calculated using the reshaping function $\mathcal{R}(x)$. Different functions of $\mathcal{R}(x)$ were tested:

$$\begin{aligned} \mathcal{R}(x) &= A\exp(-Bx), \\ \mathcal{R}(x) &= Ax + B, \\ \mathcal{R}(x) &= -Ax^2 + Bx + C, \end{aligned} \tag{6.22}$$

where A,B,C and D are constants calculated applying the boundary expressions in (6.21).

Drift Motion Model (DMM)

The prediction part of the PF algorithm that propagates the feedback from the particle set at step k to the particle set at step $k+1$ is executed by a motion model. A model was introduced in Sec. 6.1.3. Another feedback motion model is herein proposed. It carries on to the next cycle all the informations of the particle cloud using a regression method instead of creating the new set of particles only with the information of $\theta_{res,k}^{(m)}$ like in (6.20). This DMM generates a new set of $\theta_{k+1}^{(m)}$ by shifting all the previous cloud particles with the a regression parameter p:

$$\theta_{k+1}^{(m)} = \theta_{k,res}^{(m)} + \mu T + \gamma, \tag{6.23}$$

where μ is the slope of the linear regression of the N_{mm} previous samples of $\hat{\theta}_k$, and γ is a zero mean random variable like in (6.20). The performance of this method is evaluated in Sec. 6.1.6.

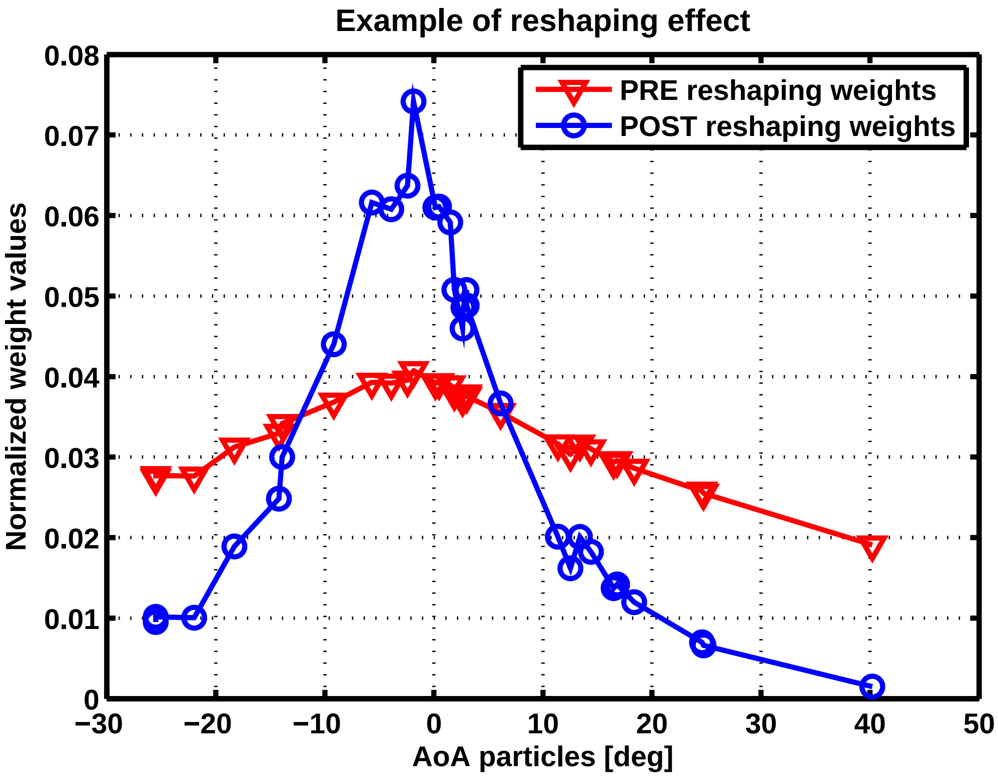

Figure 6.2: Example of weight reshaping.

Experimental Set-Up

To acquire real field measurements, we have exploited the experimental test-bed shown in Fig. 6.1 and described in [97]. The RSU deploys a 4 element ULA and operates at 2.41GHz. The OBU simulating the V2X communication deploys an Universal Software Radio Peripheral (USRP)-2932 Software Defined Radio (SDR). The source node was placed on board of a small electric vehicle for urban mobility. Another SDR was installed on the vehicle to track and save the GPS position. GPS angular informations $\theta_k^{(gps)}$ were extracted from the GPS coordinates to be used as a reference. The relative angular coordinates were obtained from the GPS longitude and latitude linearisation. A comparison with the estimates obtained both with the raw algorithm, $\tilde{\theta}_k$, and with the PF algorithm, $\hat{\theta}_k$, was then made. The electric vehicle followed the oval route shown in Fig. 6.3 to acquire a set of measurements that emulates a real dynamic car tracking scenario.

Validation and Performance Analysis

The performance of the algorithm is evaluated in terms of two parameters. The first one is the absolute value of the Pearson's correlation coefficient $|\rho|$ between the GPS angular data $\theta_k^{(gps)}$ and the AoA obtained with both the raw estimator and PF . This parameter shows intuitively how much the methods provide correlated (similar) results. The second parameter is the RMSE in the AoA estimate w.r.t. the GPS reference values. Different

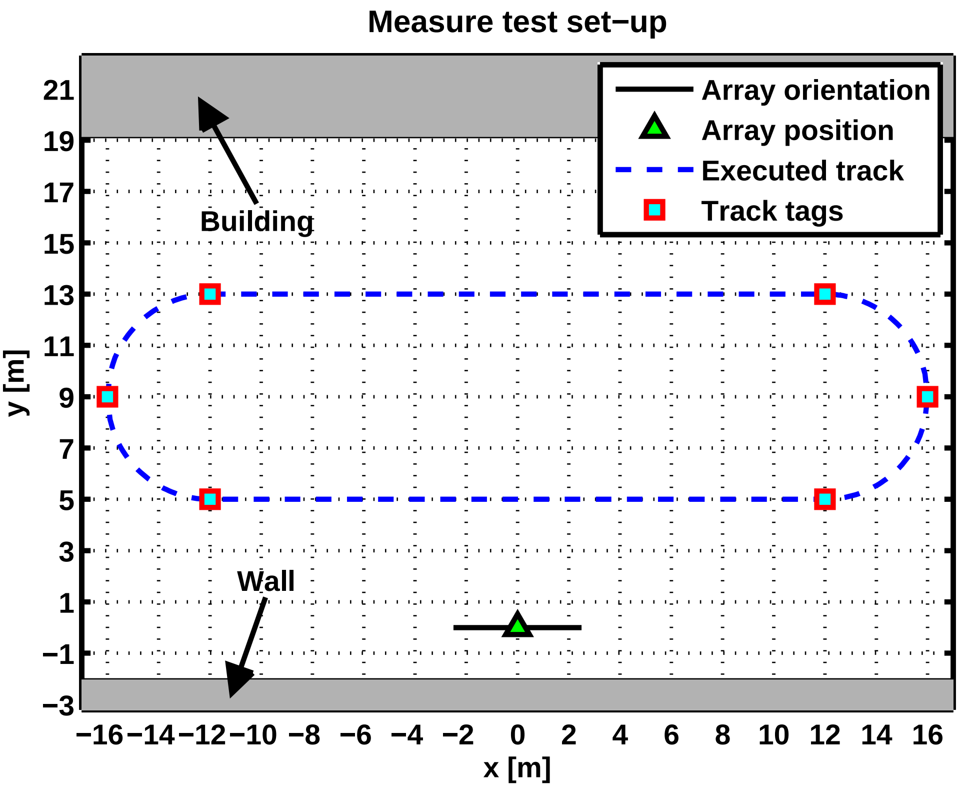

Figure 6.3: Driving path for the measurement test.

parameter configurations were considered as well as the usage of the RESH elaboration and the DMM module. The uses $M = 20$. The standard deviation of the motion model spreading σ_s introduced in (6.20) was tested in a range from 1° to 30°. In Fig. 6.4 and in Table6.1, it is possible to notice that the PF method has a maximum $|\rho|$ for a single value of σ_s. This peak value is always greater than the constant value of $|\rho|$ obtained with the raw AoA estimation ($\rho^{(raw)} = 0.48$). In particular, increasing the complexity of the PF algorithm, adding RESH and DMM , $|\rho|$ increases respectively from 0.78@σ_s=11° to 0.84@σ_s=6° and 0.88@σ_s=7°. It is possible to notice how the progressive introduction of the reshaping module and of the drift motion model increases the performance of the algorithm. A deeper analysis revealed that the introduction of RESH and DMM , especially for $\sigma_s > 10°$, causes an independence of performance from the number of particles M showing almost the same $|\rho|$ values for $M = 20$, $M = 50$ and $M = 150$.

Table 6.1: Performance improvement summary

		PF ($M = 20$, resampling=ON)					
parameter	**AoA data**	**RESH** OFF	**DMM** OFF	**RESH** ON	**DMM** OFF	**RESH** ON	**DMM** ON
$\|\rho\|$	0.48	+63%		+75%		+83%	
$RMSE$	46.9°	−25%		−31%		−42%	

In Fig. 6.5 and in Table6.1, it is possible to see that the PF methods have a minimum

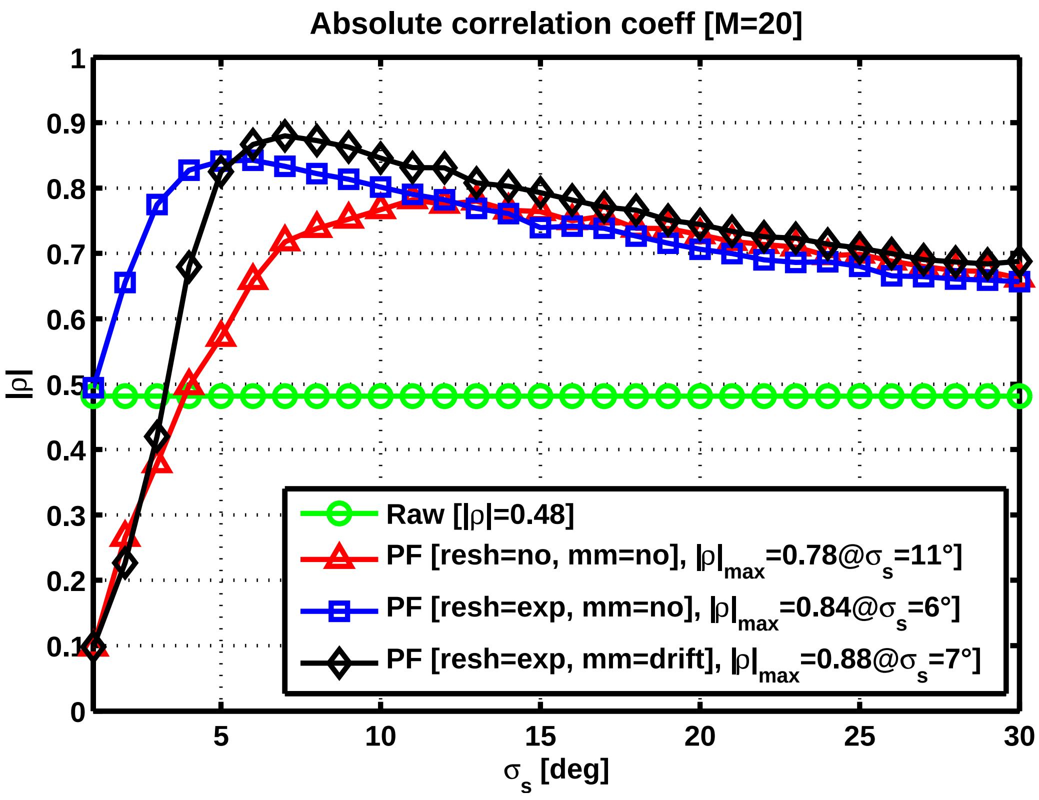

Figure 6.4: $|\rho|$ for raw estimation and for different PF configurations.

RMSE value for a single value of σ_s. This is always smaller than the constant value of RMSE attained with the raw AoA estimation ($\text{RMSE}^{(raw)} = 46.9°$). In particular, increasing the complexity of the PF algorithm, adding RESH and DMM , the RMSE decreases respectively from 35.2°@σ_s=13° to 32.3°@σ_s=6° and 27.1°@σ_s=7°. Again, the RMSE diminishes with the introduction of the reshaping filter and of the drift motion model. RESH and DMM , especially for $\sigma_s > 10°$, cause an independence of performance from the number of particles M showing almost the same $RMSE$ values for $M = 20$, $M = 50$ and $M = 150$.

Conclusions

We have presented the application of particle filtering for the estimation and tracking of the AoA in a vehicular environment by opportunistically listening to the V2X transmission by the vehicle. The conventional PF has been improved by the modification of the motion model and by an ad-hoc weight reshaping. Its performance has been evaluated in the real field and compared to that attainable with a raw AoA estimation w.r.t. the reference estimation obtained with the GPS system. It has been found that the method offers a performance close to that attainable with GPS . The approach can be used to provide full localization if correlated with geometrical street information even in situations where

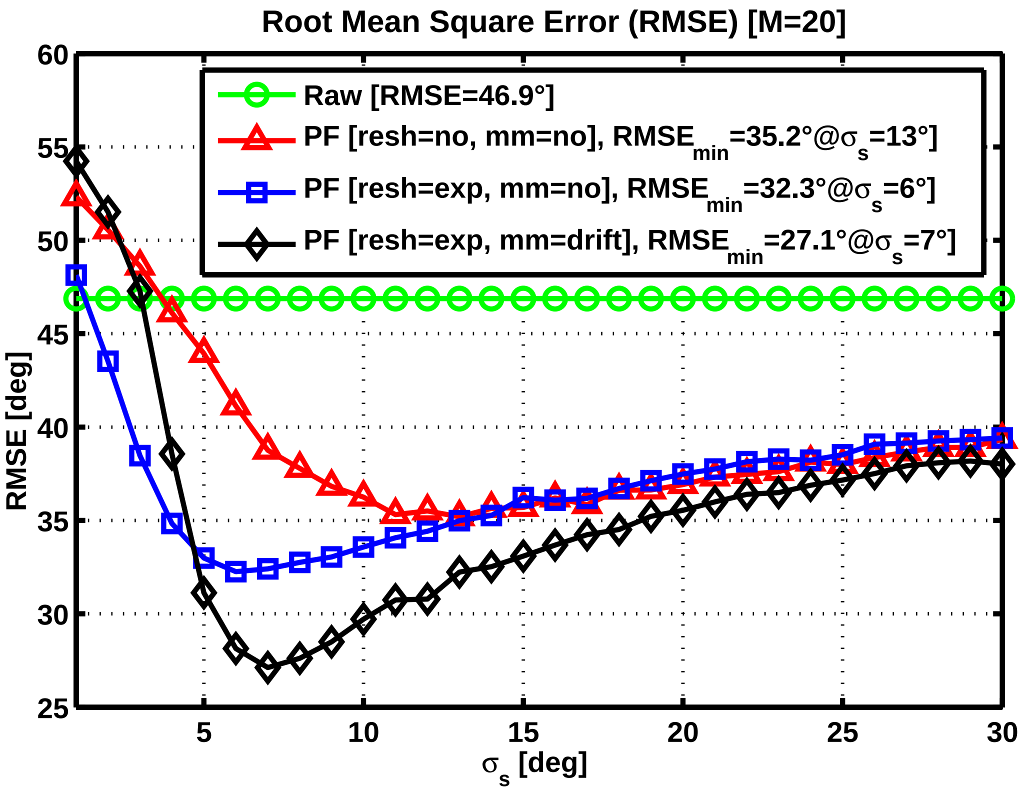

Figure 6.5: RMSE for raw estimation and for different PF configurations.

the GPS is not available. Moreover the PF AoA estimates can be integrated with GPS data to increase the localization precision through data fusion techniques.

Unmanned Aerial Vehicle (UAV) Localization

UAVs localization has become crucial in recent years, mainly for aided or self navigation and for UAV based security monitoring and surveillance. In this Ch. , azimuth and elevation radio positioning of UAVs is considered. The localization is based on multiple differential phase-of-arrival measures exploiting a 3-Axial Uniform Linear Array of antennas. An ad-hoc particle filtering algorithm is applied to improve the positioning performance using a dynamic motion model. A novel adaptive algorithm, namely Particles Swarm Adaptive Scattering (PSAS), is proposed to increment algorithm stability and precision. To assess performance a Confined Area Random Aerial Trajectory Emulator (CARATE) algorithm has been developed to generate actual paths of flying UAVs. The algorithm performance is compared with the baseline method and with the average trajectory Cramér Rao lower bound to show the effectiveness of the proposed algorithm.

Introduction

UAVs are attracting considerable attention since they can be used for a number of consumer, industrial and military applications ranging, for instance, from sport video making to environmental monitoring and parcel delivery [45,46]. A key component is the technology that allows to locate and navigate the UAVs. Presently, GNSS and inertial sensors are used to provide information on position, speed and direction of movement. Reliable localization is very important also in view of new regulations that aim at better controlling the use and the status of the UAVs for higher safety and security [47]. Furthermore recently UAVs technology has started to be under the spotlight of police audits because of possible security threats [48].

In this Ch. , a radio localization approach is considered and it is based on azimuth and elevation positioning using a transmitting source as a reference. Azimuth and elevation are determined by processing with particle filtering (PF) the signals that impinge on a Three-Axial-ULA (3A-ULA). The 3A-ULA can be mounted either on a ground base station or on the UAVs. In the first case, namely Ground Localization Scenario (GL-S), the base station passively eavesdrops the signals emitted by the UAVs to determine their angular coordinates. In the latter case, namely Self Localization Scenario (SL-S), the ground node acts as a radio anchor allowing UAVs self localization. The system can be used in a standalone way or to complement existing GNSS or inertial sensors employing data fusion techniques [49].

In Sec. 6.2.2, the analytical model for the signals received by the 3A-ULA is described. The Baseline Method (BM) coordinates estimates obtained from the 3A-ULA in Sec. 6.2.3 are iteratively processed with an ad-hoc PF algorithm described in Sec. 6.2.4. The PF technique uses a novel dynamic particles swarm management routine, namely PSAS, introduced in Sec. 6.2.5 to improve both convergence and precision performance.

In order to quantify the performance of the proposed tracking algorithm an emulator for the UAV behaviours is specifically developed in Sec. 6.2.6. This ad-hoc numerical model, namely CARATE, randomly generates trajectories in the 3 dimensional space following a well defined set of rules in order to emulate real UAV behaviours.

Finally, in Sec. 6.2.8, numerical results are reported to assess performance as a function of the UAVs motion model, the PF algorithm parameters and external detrimental impairments, such as, Phase Noise (PN) and carrier frequency Doppler Shift (DS). A comparison with the average trajectory Average Trajectory CRLB (AT-CRLB) for the angular estimation of the elevation θ and azimuth ϕ is also provided.

Positioning System Description

A system that determines the position of flying UAVs through the analysis of a signal impinging on the 3 branches of a 3A-ULA is considered.

The GL-S is built as follows: UAVs send narrow band radio signals that are captured by a ground base station equipped with a 3A-ULA. The radio signals are properly frequency/time duplexed to allow multiple UAVs tracking. The ground node can then compute locally the UAVs azimuth and elevation coordinates [21]. By sharing the data collected from more ground nodes, it is possible to achieve a full 3D positioning for the UAVs trajectories.

The SL-S is analogously arranged. Each 3A-ULA is mounted on the UAVs so that the ground device takes the role of a radio beacon anchor [98], allowing the UAVs to be self aware of their position. Using more anchors transmitting at different frequency or in a time division multiplexing fashion, the UAVs can accomplish a full 3D positioning. Clearly this scenario is implementable depending on the size of the array and to the UAVs.

The 3A-ULA is constituted, for each one of the 3 branches, by N_a antennas. Each branch is labelled with $a \in x, y, z$ to indicate along which one of the axes it is displaced. An antenna of the same branch a is indexed with $i \in [1, 2, \ldots, N_a]$ to indicate its position along the branch. Thus, the coordinates of the antennas can be written as

$$\begin{aligned} x^{(a,i)} &= (i-1)D\delta_{xa}\,, \\ y^{(a,i)} &= (i-1)D\delta_{ya}\,, \\ z^{(a,i)} &= (i-1)D\delta_{za}\,, \end{aligned} \tag{6.24}$$

where δ_{ij} is the Kronecker delta that is 1 for $i = j$ and 0 otherwise and D is the constant distance between antennas.

The signal model considered in the following describes for simplicity the scenario with only one UAV, this assumption can be easily extended to a multi UAVs application. Both GL-S and SL-S scenarios, due to symmetry, can be modelled in the same way. So that in general, the down-converted signal received by the i-th antenna of the 3A-ULA branch a, can be written as

$$s_n^{(a,i)} = A_n e^{j\left[\psi_n^{(a,i)} + \gamma_n^{(a,i)} + \varphi_n + \zeta\right]} + w_n^{(a,i)}, \tag{6.25}$$

where n indexes the time, sampled with period T. The quantity $\psi_n^{(a,i)}$ is the phase of the demodulated signal impinging on the i-th sensor of the branch a, namely the PoA, in the ideal case without impairing effects. $\gamma_n^{(a,i)}$ represents the phase DS caused by the non zero speed of the radio source with respect to each receiving array element. φ_n is the PN of the oscillators. It is considered white for this application [73]. The component ζ is the PO between modulating and demodulating oscillators. The phase components of (6.25) are more in detail described below:

$$\begin{aligned} \psi_n^{(a,i)} &= 2\pi f_0 \tau_n^{(a,i)}\,, \\ \gamma_n^{(a,i)} &= 2\pi f_0 C_{DS}(nT - \tau_n^{(a,i)})\tau_n^{(a,i)}\,, \end{aligned} \tag{6.26}$$

where f_0 is the carrier frequency of the received modulated signal and where $\tau_n^{(a,i)}$ is the ToA of the plane wave from the source to the sensor. $C_{DS}(t) = v_r(t)/c_0$ is the DS coefficient due to the movement of the UAV. The parameter $v_r(t)$ is the UAV speed in the direction of the center of the 3A-ULA and c_0 is the speed of light. Finally, $w_n^{(a,i)}$ is circular C-AWGN with standard deviation σ_w. The receiving architecture comprises N_a down-converting branches for each axis of the 3A-ULA all fed by the same oscillator. For this reason PN and PO components are identical for all antennas.

Considering the scenario where the transmitted signals carry also information, the component A_n of (6.26) is representative of the unknown informative part of the signal, specifically the modulated complex data symbols. For the application herein considered A_n is assumed to be an equi-probable symbol of an unknown order PSK modulation scheme. For this reason the symbol is modelled as complex uniform ring shaped noise (RSN) $A_n = |A|e^{j\xi_n}$ where $\xi_n \sim U(0, 2\pi)$ is a random uniform variable between 0 and 2π and $|A|$ is the constant amplitude of the modulated signal.

In this model, the presence of multipath propagation is not considered, a line of sight environment is assumed. This can hold true when the ground and UAV antennas have a wide vertical lobe respectively directed upward and downward.

Azimuth and Elevation Estimation With 3A-ULA

A radio source moving in the 3D cartesian space is considered. Its angular spherical coordinates θ_n and ϕ_n are determined using the same coordinate system of the 3A-ULA defined in (6.24). A trajectory example is visible in Fig. 6.7. The positioning technique used to locate the radio source is based on the estimation of the phase difference of the received signals between different antenna couples belonging to the same 3A-ULA branch a, namely the D-PoA $\hat{\psi}_n^{(a)}$. The D-PoA is defined as $\hat{\psi}_n^{(a)} = \psi_n^{(a,2i-1)} - \psi_n^{(a,2i)}$ $\forall i \in [1, 2, \ldots, N_a/2]$.

In [73] a technique to estimate $\hat{\psi}_n^{(a)}$ in a scenario with impaired signals similar to (6.25) is described. Applying this technique for the model herein considered, it allows to exploit the D-PoAs from the signal model introduced in (6.25). $\hat{\psi}_n^{(a)}$ are estimated as $\underline{/u_n^{(a)}}$, where $\underline{/\cdot}$ stands for the phase operator and where:

$$u_n^{(a)} = \frac{2}{N_a} \sum_{i=1}^{N_a/2} s_n^{(a,2i-1)} s_n^{(a,2i)*} , \qquad (6.27)$$

where an average over the $N_a/2$ distinct antenna pairs is performed to mitigate noise and compensate other zero mean impairments. Using $u_n^{(a)}$, the angular spherical coordinates

θ_n and ϕ_n are estimated respectively with $\tilde{\theta}_n$ and $\tilde{\phi}_n$ as following:

$$\begin{aligned} \tilde{\theta}_n &= \arctan\left(\sqrt{(\underline{/u_n^{(x)}})^2 + (\underline{/u_n^{(y)}})^2}, \underline{/u_n^{(z)}}\right), \\ \tilde{\phi}_n &= \arctan\left(\underline{/u_n^{(y)}}, \underline{/u_n^{(x)}}\right), \end{aligned} \tag{6.28}$$

where $\arctan(\cdot,\cdot)$ is the arctangent function extended to the $[0, 2\pi)$ domain.

The estimations $\tilde{\theta}_n$ and $\tilde{\phi}_n$ made in (6.28) will be denoted in the following as BM estimations to differ from the PF estimations) that will be introduced in Sec. 6.2.4.

PF Algorithm Estimation

In this section, the application of the PF algorithms [43] to the localization problem introduced in Sec. 6.2.3 is briefly described. PF algorithm techniques have been chosen because of their simple, scalable and flexible numerical implementation with respect to other methods like Extended Kalman Filter [44] that approach the problem linearising the system and approximating the probability density functions as Gaussians. PF is specifically designed to fit to complex system models as well as to non linear and non Gaussian configurations. The target of PF methods is to estimate the dynamic evolution of the hidden states in a system, i.e. the coordinates θ_n and ϕ_n of the radio source, using the sequential discrete noisy measures $u_n^{(a)}$ introduced in (6.27). In PF, it is necessary to hypothesize a model for the observations and for the states temporal evolution [43]. The evolution model for the hidden states θ_n and ϕ_n is

$$\begin{aligned} \theta_n &= g_\theta(\theta_{[n-N_{mm} \div n-1]}, p_{\theta,n}), \\ \phi_n &= g_\phi(\phi_{[n-N_{mm} \div n-1]}, p_{\phi,n}), \end{aligned} \tag{6.29}$$

while the model for the observations related to the hidden states introduced in (6.27) is

$$u_n^{(a)} = h([\theta_n, \phi_n], q_n). \tag{6.30}$$

The relations (6.29) show how the current hidden state $[\theta_n, \phi_n]$ evolves thanks to the previous N_{mm} states and the random uncertain variables $p_{\theta,n}$ and $p_{\phi,n}$ through the motion model function g. The relation (6.12) shows how the measurements $u_n^{(a)}$ depend only on the current state $[\theta_n, \phi_n]$ and on a random uncertain variable q_n through the measure model function h.

For notational simplicity, both θ_n and ϕ_n will be denoted with the generic angle α_n. When needed this generalization will be removed.

PF has been chosen because of its simplicity and versatility. PF algorithms are a numeric implementation of Bayesian estimation [44], a statistical approach to iteratively increase the knowledge of the states to be estimated by narrowing their pdf conditioned by the sequential acquisition of new measures during time. The pdf of α_n defined as $f_{\alpha_n}[\alpha]$ is approximated in a discrete way [96] with a set of M particles $\{\alpha_n^{(m)}\}_{m=1,\dots,M}$ and a set of weights $\{w_{\alpha,n}^{(m)}\}_{m=1,\dots,M}$. Particles and weights are generated from the partial knowledge given from the measure model h and the state evolution model g_α. This knowledge is more and more incremented by the continuous time acquisition of the measures $u_n^{(a)}$. Clearly, the UAV moves so that its coordinates change over time n.

As shown in (6.29), in the PF algorithm an assumption about the model that controls the evolution of the hidden state of the system g_α is made. For this purpose the motion model used is the DMM proposed in [93]. The DMM generates the new particles cloud $\{\alpha_n^{(m)}\}$ at step n shifting the previous step re-sampled cloud [43] $\{\alpha_{n-1,RES}^{(m)}\}$ using the regression constant $\mathfrak{m}_{n-1}$:

$$\alpha_n^{(m)} = \alpha_{n-1,RES}^{(m)} + \mathfrak{m}_{n-1} T + \eta \,, \tag{6.31}$$

where $\alpha_{n-1,RES}^{(m)}$ is the m-th particle of the $n-1$ step cloud after the resampling process [96]. $\eta \sim \mathcal{N}(\sigma_s, m_s = 0)$ is a Gaussian random variable that represents the fundamental statistical scattering part of the motion model. The parameter $\mathfrak{m}_{n-1}$ is the slope of the linear regression of the N_{mm} previous values of $\hat{\alpha}_n$, the PF estimates of α_n. It is important to emphasize that in this regression model, due to the periodic nature of α_n, it is necessary to use the previously saved N_{mm} unwrapped values of $\hat{\alpha}_n$. This is necessary to correctly track the azimuthal coordinate ϕ_n during the 2π angular shifts from $-\pi$ to $+\pi$ going from the third to the second Cartesian quadrant.

Particles weights $w_{\alpha,n}^{(m)}$ are calculated by the PF algorithm using in each cycle the temporary estimates $\tilde{\alpha}_n$ obtained from the real acquired measures in (6.28). This temporary estimations are compared with the cloud of generated particles $\alpha_n^{(m)}$ through an exponential weighting function to obtain the set of weights $w_{\alpha,n}^{(m)}$:

$$w_{\alpha,n}^{(m)} = \exp\left(-|\alpha_n^{(m)} - \tilde{\alpha}_n|\right) , \tag{6.32}$$

where, to correct unnecessary 2π offsets of $|\alpha_n^{(m)} - \tilde{\alpha}_n|$ due to the periodicity of α_n, the minimum absolute value of the distance of the two angles $\alpha_n^{(m)}$ and $\tilde{\alpha}_n$ in the 2π-modulo space is computed. A reshaping technique [93] is then applied, before estimation, to regularize the particle cloud weights.

The PF estimation $\hat{\alpha}_n$ of the hidden state α_n is then computed through a weighted average of the reshaped particles swarm:

$$\hat{\alpha}_n = \sum_{m=1}^{M} w_{\alpha,n,RESH}^{(m)} \alpha_n^{(m)} \, . \tag{6.33}$$

where $w_{\alpha,n,RESH}^{(m)}$ is the weight after the reshaping process. Finally, after the estimation stage, the particles cloud is re-sampled, generating the set $\alpha_{n,RES}^{(m)}$, to eliminate spurious particles and avoid fragmentation.

Novel Particles Swarm Adaptive Scattering (PSAS)

The parameter σ_s is the standard deviation of the random variable η introduced in (6.31). In the previous section σ_s, it was considered constant over time. However, depending on the situation of the tracking algorithm, it will be shown that it is better to have a dynamic $\sigma_{s,n}$. It is possible to define two parameters that describe the particle cloud: Ω_n, Particles Cloud Width (PC-W) that describes how much wide the set of particles is, and ε_n, the Particles Cloud Granularity (PC-G) that indicates the inter particle distance:

$$\Omega_n = \max_m\{\alpha_n^{(m)}\} - \min_m\{\alpha_n^{(m)}\} \leq 2\pi \,, \tag{6.34}$$

$$\varepsilon_n = \Omega_n/(M-1) \,. \tag{6.35}$$

The value of Ω_n influences the convergence speed of the algorithm. In fact, if the particles cloud is positioned over the value to be estimated the convergence is fast because the the exponential weighting function introduced in (6.32) gives high weights to the nearest particles and negligible weights to the further ones. However, if the particles cloud is located far from the value to be estimated, convergence is slower because the exponential weighting function algorithm gives almost the same weights to all particles. Thus, it will need more iterations to move the particles swarm, cycle by cycle, near the convergence point. For these reasons a bigger value of Ω_n will lead to wider clouds, encouraging the convergence. On the other hand, smaller values of Ω_n will make the algorithm slower and more unstable to fast state changes.

The value of ε_n influences the precision of convergence. In fact, hypothesising to have reached the convergence point the estimation precision is upper bounded by the average inter particle distance, the PC-G.

Considering the spreading variable η introduced in (6.31) as a Gaussian variable with zero mean and standard deviation σ_s, it is possible to estimate the PC-W using the Tchebysheff's inequality as $\Omega_n \approx 6\sigma_s \propto \sigma_s$. Likewise the PC-G can be estimated as $\varepsilon_n \approx 6\sigma_s/(M-1) \propto \sigma_s$. These relations show that σ_s is directly proportional to PC-W and PC-G. Because of the previous observation it is possible to conclude that, given a swarm of M particles, during the convergence phase a bigger value of σ_s would be more appropriate because it would lead to faster results. On the other hand, after the convergence phase, smaller values of σ_s would be more appropriate to increase the estimation precision.

For these reasons a novel algorithm that manages the dynamic evolution of σ_s across the iterations, namely PSAS, is proposed.

The distance metric $d_n^{(m)}$ is defined as a baseline error cloud for the particles and is used from the PSAS to select the convergence status of the PF algorithm. The error cloud $d_n^{(m)}$ is calculated between the baseline estimation $\tilde{\alpha}_n$ introduced in (6.28) and the re-sampled particle swarm $\alpha_{n,RES}^{(m)}$:

$$\begin{aligned} d_n^+ &= avg(d_n^{(m)}) + std(d_n^{(m)})\,, \\ d_n^- &= avg(d_n^{(m)}) - std(d_n^{(m)})\,, \\ d_n^{(m)} &= |\alpha_{n,RES}^{(m)} - \tilde{\alpha}_n|\,, \end{aligned} \tag{6.36}$$

where the operators *avg* and *std* denote respectively the numeric operations of average and standard deviation and the absolute value operates in the periodic $[-\pi, \pi[$ domain. The parameters d_n^- and d_n^+ represent respectively the lower and higher bounds of the error cloud $d_n^{(m)}$ and are used as thresholds from the PSAS algorithm to trigger the increment or the decrement of $\sigma_{s,n}$ as follows:

$$\sigma_{s,n} = \sigma_{s,n-1}\,(1 \pm \delta\sigma_s)\ , \tag{6.37}$$

where $\delta\sigma_s > 0$ is the proportional feedback parameter of the PSAS. The value of $\delta\sigma_s$, depending on the two feedback parameters d_n^+ and d_n^- and the threshold value γ_{th}, is set positive to iteratively increment $\sigma_{s,n}$, negative to decrement $\sigma_{s,n}$ and is set to zero to keep it constant.

The value of $\sigma_{s,n}$ is incremented w.r.t. its previous value when the condition of non-convergence is detected. This condition holds true when the error cloud $d_n^{(m)}$ is reasonably out of the $[-\gamma_{th}, \gamma_{th}]$ convergence interval, i.e., when $d_n^- > \gamma_{th}$ or $d_n^+ < -\gamma_{th}$. Then, the PC-W is incremented to encourage convergence. If the previous condition is not satisfied, the value of $\sigma_{s,n}$ is decremented w.r.t. its previous value when the convergence state is detected. This condition holds true when the error cloud $d_n^{(m)}$ is on the edges of the $[-\gamma_{th}, \gamma_{th}]$ convergence interval i.e. when $d_n^+ > \gamma_{th}$ or $d_n^- < -\gamma_{th}$. Then, the PC-G is reduced to increment the precision. For the remaining values of d_n^+ and d_n^- the condition of tight-convergence is reached. In this state the value of $\sigma_{s,n}$ is kept the same w.r.t. its previous value. This PSAS case keeps the cloud at the same size to avoid instability conditions due to rapid changes of the convergence point. The values of the feedback parameter $\delta\sigma_s$ and the threshold parameter γ_{th} are related to the dynamic behaviour of the convergence point that is related to the UAV motion model. Optimal values for $\delta\sigma_s$ and γ_{th} were numerically calculated for the trajectories generated by CARATE.

Unmanned Aerial Vehicles (UAVs) Trajectory Emulator

To assess performance of BM and PF algorithms estimations and to evaluate the effects of different parameters on the estimation process, it is necessary to emulate UAVs trajectories using a proper coordinates evolution algorithm. Herein, a possible trajectory generation method is proposed.

The proposed algorithm, named CARATE generates iteratively a 3D path obtained from a variable length previous history of the trajectory and a tunable set of random variables. CARATE is specifically designed to emulate UAVs trajectories inside a limited flight area, in the GL-S, around the receiving array. Thus, the generated trajectories allow to test the tracking algorithms for a broad range of arrival angles. An UAV located far from the receiving array instead, would be localized using a limited range of angles. The Cartesian position $[x_n, y_n, z_n]$ at time n of the UAV evolves as

$$\begin{aligned} x_n &= x_{n-1} + T v_n \cos(\phi'_n) \sin(\theta'_n)\,, \\ y_n &= y_{n-1} + T v_n \sin(\phi'_n) \sin(\theta'_n)\,, \\ z_n &= z_{n-1} + T v_n \cos(\theta'_n)\,. \end{aligned} \tag{6.38}$$

The angle ϕ'_n, depicted in Fig. 6.6, is the local azimuthal angle at time n of the actual trajectory coordinates $[x_n, y_n, z_n]$ seen from the previous path point $[x_{n-1}, y_{n-1}, z_{n-1}]$. The local elevation angle θ'_n can be defined analogously. v_n is the absolute speed of the UAV. At each step, the trajectory increments generated by θ'_n, ϕ'_n and v_n are related to the "seed" components $\theta_{\text{seed},n}$, $\phi_{\text{seed},n}$ and $v_{\text{seed},n}$ and to the random components $\delta\theta_n$, $\delta\phi_n$ and δv_n as follows

$$\begin{aligned} \theta'_n &= \theta_{\text{seed},n} + \delta\theta_n\,, \\ \phi'_n &= \phi_{\text{seed},n} + \delta\phi_n\,, \\ v_n &= v_{\text{seed},n} + \delta v_n\,. \end{aligned} \tag{6.39}$$

The random components are generated following respectively the Normal distributions $\delta\theta \sim N(m_{\delta\theta}, \sigma_{\delta\theta})$, $\delta\phi \sim N(m_{\delta\phi}, \sigma_{\delta\phi})$, $\delta v \sim N(m_{\delta v}, \sigma_{\delta v})$. The parameters of the random component distributions affect the UAV path behaviour. For example for $m_{\delta} v > 0$ the UAV will have an accelerating trend and for $m_{\delta\phi} > 0$ the UAV will tend to turn anti-clockwise. The seed values introduced in (6.39) are the history parameters that express how much the evolution of the path is related to its past:

$$\begin{aligned} \theta_{\text{seed},n} &= \arccos\left[\Delta z_n(N_{\text{ang}}), \Delta r_n(N_{\text{ang}})\right], \\ \phi_{\text{seed},n} &= \arctan\left[\Delta y_n(N_{\text{ang}}), \Delta x_n(N_{\text{ang}})\right], \\ v_{\text{seed},n} &= \sum_{k=1}^{N_{\text{sp}}} \frac{v_{n-k}}{N_{\text{sp}}}\,, \end{aligned} \tag{6.40}$$

where $\arctan(\cdot,\cdot)$ is the arctangent function defined within $[0, 2\pi)$ and where

$$\begin{aligned} \Delta x_n(N_{\text{ang}}) &= x_{n-1} - x_{n-N_{\text{ang}}}\,, \\ \Delta y_n(N_{\text{ang}}) &= y_{n-1} - y_{n-N_{\text{ang}}}\,, \\ \Delta z_n(N_{\text{ang}}) &= z_{n-1} - z_{n-N_{\text{ang}}}\,, \\ \Delta r_n(N_{\text{ang}}) &= \sqrt{\Delta x_n(N_{\text{ang}})^2 + \Delta y_n(N_{\text{ang}})^2 + \Delta z_n(N_{\text{ang}})^2}\,. \end{aligned} \tag{6.41}$$

In Fig. 6.6, the relations among the CARATE components for the variable ϕ_n are represented. As shown in (6.40), the smaller the window width of the seed parameters N_{ang}

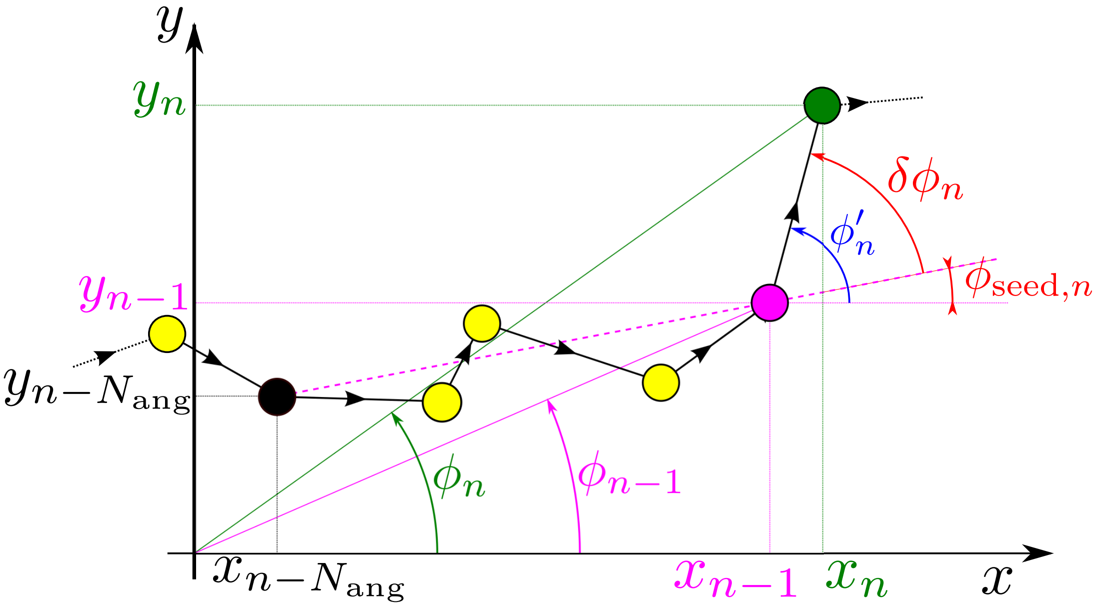

Figure 6.6: Diagram of CARATE components for variable ϕ, example with $N_{\text{ang}} = 5$
.

and N_{sp}, the higher the influence of the path randomization will be w.r.t. the past history of the path itself. The same effect will occur for higher values of the standard deviation $\sigma_{\delta\theta}$, $\sigma_{\delta\phi}$, $\sigma_{\delta v}$ of the random components $\delta\theta$, $\delta\phi$, δv introduced in (6.39).

The CARATE algorithm, as visible in the sample path in Fig. 6.7, generates a 3D trajectory inside a limited flight area, formed by the horizontal bound region S_{xy} and the vertical bound region S_{z}. S_{xy} is defined as $\{|x| < L_{\text{xy}} \cap |y| < L_{\text{xy}}\}$ while S_{z} is defined as $\{z > L_z^{\text{min}} \cap z < L_z^{\text{max}}\}$. A specific routine of the algorithm has been developed to keep the trajectory inside the limited flight area, preserving it smooth and without sharp edges on region bounds. If x_n or y_n exceed S_{xy} the value of $\phi_{\text{seed},n}$ introduced in (6.40) is forced for the subsequent N_{bend} steps to follow a set of equispaced values between $\phi_{\text{seed},n}$ and $\phi_{\text{seed,END}}$. The value of $\phi_{\text{seed,END}}$ is appropriately defined depending on the Cartesian quadrant where the trajectory crosses the surface of S_{xy}. Analogously, if z_n exceeds S_{z} the value of $\theta_{\text{seed},n}$ introduced in (6.40) is forced for the next N_{bend} steps to a set of equally spaced values between $\theta_{\text{seed},n}$ and $\theta_{\text{seed,END}}$. The value of $\theta_{\text{seed,END}}$ is also defined depending on the Cartesian quadrant where the surface of S_{z} has been crossed.

Cramér-Rao Lower Bound (CRLB)

In statistics the CRLB expresses the lowest value of the RMSE of an optimal estimator given a certain set of data [99]. In this Ch. the estimations of the coordinates $[\theta_n, \phi_n]$ is carried out from the information given by the measurements $u_n^{(x)}$, $u_n^{(y)}$, $u_n^{(z)}$.

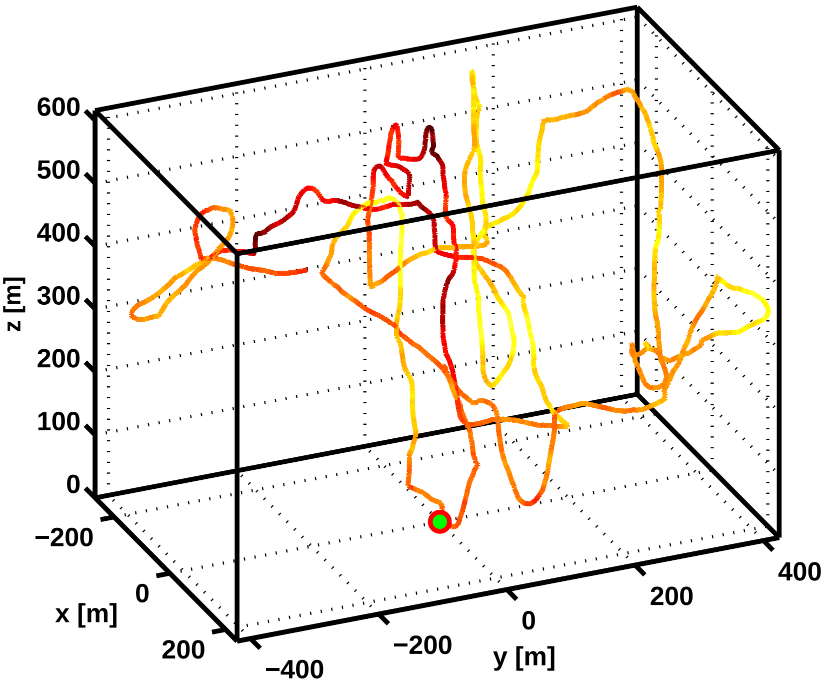

Figure 6.7: Example of UAV 3D trajectory generated with CARATE.

Now, we define $\boldsymbol{b}_n = [b_n^{(a)}]_{n\in[x,y,z]}$ as the vector of ideal measured values, namely $u_n^{(a)}$ in (6.27) but without the detrimental effects due to the impairments introduced in (6.25) such as PN, DS and C-AWGN:

$$b_n^{(a)} = |A|^2 e^{j\hat{\psi}_n^{(a)}} \,, \tag{6.42}$$

where, as introduced in Sec. 6.2.2, $\hat{\psi}_n^{(a)}$ is the D-PoA for the a-th 3A-ULA antenna branch and $|A|$ is the constant amplitude of the complex down-converted constellation. The vector of real measurements $\boldsymbol{u}_n = [u_n^{(x)}, u_n^{(y)}, u_n^{(z)}]$, defined in (6.27), can be written as

$$\begin{aligned} u_n^{(a)} &= \frac{2}{N_a} \sum_{i=1}^{N_a/2} |A|^2 e^{j\hat{\psi}_n^{(a)}} + W_n^{(a,i)} \,, \\ &= \hat{A} e^{j\hat{\psi}_n^{(a)}} + \hat{W}_n^{(a)} \,, \end{aligned} \tag{6.43}$$

where the intermediate signal $|A|^2 e^{j\hat{\psi}_n^{(a)}} + W_n^{(a,i)}$ is averaged through antenna pairs and $\hat{A} = (2/N_a) \sum_{i=1}^{N_a/2} |A|^2 = |A|^2$. The noise components in (6.43) are:

$$\begin{aligned} W_n^{(a,i)} = {} & |A| e^{j\psi_n^{(a,2i-1)}} w_n^{(a,2i)*} + |A|^* e^{-j\psi_n^{(a,2i)}} w_n^{(a,2i-1)} + \\ & + w_n^{(a,2i-1)} w_n^{(a,2i)*} \,, \end{aligned} \tag{6.44}$$

$$\hat{W}_n^{(a)} = \frac{2}{N_a} \sum_{i=1}^{N_a/2} W_n^{(a,i)} \,, \tag{6.45}$$

where the notation $(\cdot)^*$ denotes the conjugate operator. $w_n^{(a,i)}$ is the C-AWGN with zero mean an variance σ_w^2 and $\psi_n^{(a,i)}$ is the PoA, as defined in (6.25). The expectation of the differential noise $W_n^{(a,i)}$ among the antennas of the same branch is $m_W = 0$, while its variance $\sigma_W^2 = 2|A|^2\sigma_w^2 + \sigma_w^4$. Analogously, the average differential noise $\hat{W}_n^{(a)}$ is described by its mean $m_{\hat{W}} = 0$ and its variance $\sigma_{\hat{W}}^2 = (2/N_a)\sigma_W^2$.

To calculate the CRLB it is necessary to evaluate the log-likelihood $L(\phi,\theta) = \ln P[\boldsymbol{u}_n|\boldsymbol{b}_n]$ of the acquired data given the parameters to be estimated. $\ln(\cdot)$ represents the natural logarithm. In this context, for the calculation of CRLB, the measurements vector $\boldsymbol{u}_n$ is considered affected only by C-AWGN noise without the influence of the other impairments introduced in (6.25). This assumption yields to the likelihood gaussianity and is verified via numerical fitting similarly to [100], so that:

$$L(\phi,\theta) = -3\ln\left(\pi\sigma_{\hat{W}}^2\right) - \frac{1}{\sigma_{\hat{W}}^2}\|\boldsymbol{b}-\boldsymbol{u}\|^2\,, \tag{6.46}$$

where the time index n is omitted until the end of the CRLB derivation for notational simplicity. The CRLB of the variable α_r, defined as the r-esimal element of the unknowns vector $\boldsymbol{\alpha} = [\phi,\theta]$, is

$$\mathrm{CRLB}_{\alpha_r}(\phi,\theta) = \left\{F(\phi,\theta)^{-1}\right\}_{(r,r)}\,, \tag{6.47}$$

where $F(\phi,\theta)$ is the Fischer information matrix:

$$F(\phi,\theta) = -E\left\{\left[\frac{\partial^2}{\partial\alpha_h\partial\alpha_k}L(\phi,\theta)\right]_{(h,k)\in[1,2]}\right\}. \tag{6.48}$$

For the log-likelihood function described in (6.46), we obtain

$$\begin{aligned} F(\phi,\theta) &= \begin{bmatrix} \|\frac{\partial\boldsymbol{\beta}}{\partial\phi}\|^2 & \frac{\partial\boldsymbol{\beta}}{\partial\phi}\frac{\partial\boldsymbol{\beta}^{\mathrm{T}}}{\partial\theta} \\ \frac{\partial\boldsymbol{\beta}}{\partial\theta}\frac{\partial\boldsymbol{\beta}^{\mathrm{T}}}{\partial\phi} & \|\frac{\partial\boldsymbol{\beta}}{\partial\theta}\|^2 \end{bmatrix} = \\ &= 2\left(\frac{2\pi|A|^2 D_{\mathrm{norm}}}{\sigma_{\hat{W}}}\right)^2 \begin{bmatrix} (\sin\theta)^2 & 0 \\ 0 & 1 \end{bmatrix}, \end{aligned} \tag{6.49}$$

where $\boldsymbol{\beta} = [\cos\phi\sin\theta, \sin\phi\sin\theta, \cos\theta]$ is the unit direction vector and $D_{\mathrm{norm}} = D/\lambda_0$ is the normalized inter-antenna distance. The notation $(\cdot)^{\mathrm{T}}$ denotes the transpose operator. Finally, the CRLB expressions for ϕ and θ are:

$$\begin{aligned} \mathrm{CRLB}_\phi(\phi,\theta) &= \frac{1}{2}\left(\frac{\sigma_{\hat{W}}}{2\pi|A|^2 D_{\mathrm{norm}}}\right)^2\left(\frac{1}{\sin\theta}\right)^2, \\ \mathrm{CRLB}_\theta(\phi,\theta) &= \frac{1}{2}\left(\frac{\sigma_{\hat{W}}}{2\pi|A|^2 D_{\mathrm{norm}}}\right)^2. \end{aligned} \tag{6.50}$$

The RMSE of every estimator of the unknown α_r from the measurements $\boldsymbol{u}$ is lower bounded by $\sqrt{\mathrm{CRLB}_{\alpha_r}}$. It is important to state again that this C-AWGN-only CRLB calculated in (6.50) takes into account C-AWGN but not the other previously introduced impairments, in particular DS and PN. Given the previous assumptions, the AWGN-only CRLB is lower or equal to the fully-impaired CRLB. Another relevant point is that the computed CRLB doesn't take in account the motion model and the trajectory history differently from the PF algorithm. The CRLB is simply computed from the 3 observations $u_n^{(a)}$ introduced in (6.27) at time nT, as the BM does. Instead, the proposed PF algorithm exploits the motion model jointly with PSAS, using information coming from the trajectory history. For this reason, it may occur that the PF estimation offers better performance than the CRLB.

Performance Analysis

The performance of the PF algorithm are now assessed. A comparison with the BM estimation introduced in Sec. 6.2.3 and the CRLB calculated in Sec. 6.2.7 are also made. Different UAV trajectories are generated with the CARATE to assess performance. Each UAV trajectory is N time samples long. In order to have a common performance evaluation metric, in the following we define the average of the RMSE calculated through every trajectory sample, namely the Average Trajectory RMSE (AT-RMSE).

The n_{traj}-esimal generated trajectory is described with the set $\{\theta_n^{(n_{\mathrm{traj}})}, \phi_n^{(n_{\mathrm{traj}})}\}$, its BM estimation is $\{\tilde{\theta}_n^{(n_{\mathrm{traj}})}, \tilde{\phi}_n^{(n_{\mathrm{traj}})}\}$ and its PF estimation $\{\hat{\theta}_n^{(n_{\mathrm{traj}})}, \hat{\phi}_n^{(n_{\mathrm{traj}})}\}$. Their AT-RMSE are respectively $\overline{\mathrm{RMSE}}_{\alpha,\mathrm{BM}} = (1/N_{\mathrm{traj}}) \sum_{n_{\mathrm{traj}}=1}^{N_{\mathrm{traj}}} \mathrm{RMSE}_{\alpha,\mathrm{BM}}^{(n_{\mathrm{traj}})}$ and $\overline{\mathrm{RMSE}}_{\alpha,\mathrm{PF}} = (1/N_{\mathrm{traj}}) \sum_{n_{\mathrm{traj}}=1}^{N_{\mathrm{traj}}} \mathrm{RMSE}_{\alpha,\mathrm{PF}}^{(n_{\mathrm{traj}})}$ for $\alpha \in [\theta, \phi]$ where

$$\mathrm{RMSE}_{\alpha,\mathrm{BM}}^{(n_{\mathrm{traj}})} = \sqrt{\frac{\sum_{n=1}^{N} (\alpha_n^{(n_{\mathrm{traj}})} - \tilde{\alpha}_n^{(n_{\mathrm{traj}})})^2}{N}}, \tag{6.51}$$

$$\mathrm{RMSE}_{\alpha,\mathrm{PF}}^{(n_{\mathrm{traj}})} = \sqrt{\frac{\sum_{n=1}^{N} (\alpha_n^{(n_{\mathrm{traj}})} - \hat{\alpha}_n^{(n_{\mathrm{traj}})})^2}{N}}, \tag{6.52}$$

are the RMSEs calculated for each trajectory n_{traj}. N_{traj} is the number of generated trajectories.

Analogously, with the purpose to allow a performance comparison with the CRLB, we define the AT-CRLB, as $\overline{\mathrm{CRLB}}_{\alpha} = (1/N_{\mathrm{traj}}) \sum_{n_{\mathrm{traj}}=1}^{N_{\mathrm{traj}}} \mathrm{CRLB}_{\alpha}^{(n_{\mathrm{traj}})}$ for $\alpha \in [\theta, \phi]$ and where

$$\mathrm{CRLB}_{\alpha}^{(n_{\mathrm{traj}})} = \frac{1}{N} \sum_{n=1}^{N} \mathrm{CRLB}_{\alpha}(\phi_n^{(n_{\mathrm{traj}})}, \theta_n^{(n_{\mathrm{traj}})}) . \tag{6.53}$$

The default parameters for the performance evaluation are: a) angles $\sigma_{\delta\theta} = 7°$, $\sigma_{\delta\phi} = 7°$ and $N_{\mathrm{ang}} = 20$; b) speed $v_{\min} = 0.5$Km/h, $v_{\max} = 10$Km/h and $N_{\mathrm{sp}} = 2$. The array parameters are $N_a = 6$ and $D_{\mathrm{norm}} = 1/3$. The PF algorithm basic settings are $M = 20$ and $N_{mm} = 20$. PSAS parameters $\delta\sigma_s = 25\%$ and $\gamma_{th} = 10°$ were numerically optimized for

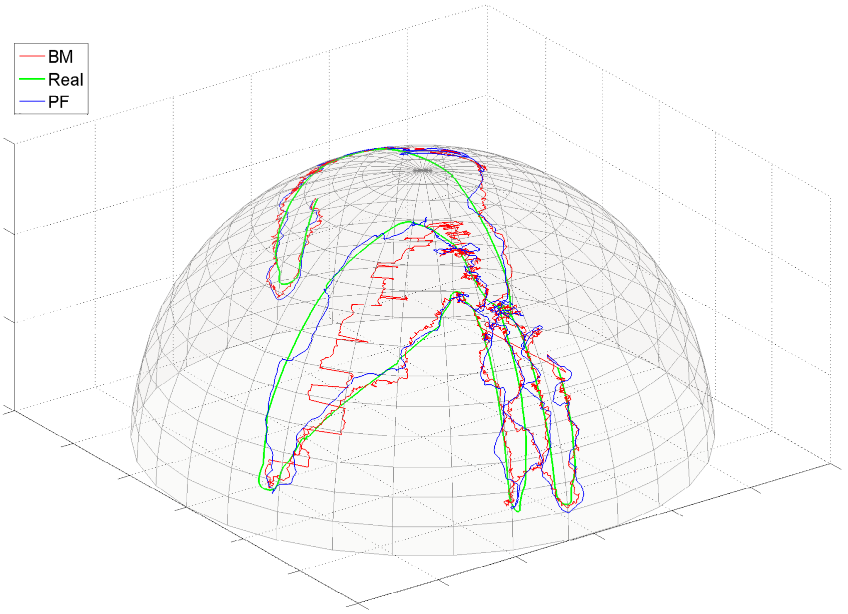

Figure 6.8: Example of UAV angular tracking. Real trajectory and PF and BM estimations are represented. The angular trajectory is traced over a unitary hemisphere.

the CARATE algorithm. In the signal model introduced in (6.25), the PN is considered white with standard deviation $\sigma_{PN} = 1°$, the PO is considered uniform in $[0, 2\pi)$ for each array element and the signal-to-noise-ratio is SNR $= [|A|^2/\sigma_w^2]db = 10dB$. The number of simulated trajectories N_{traj} and their length N have been properly dimensioned to guarantee the statistical confidence of the results.

In Fig. 6.7 an example of 3D-trajectory generated for performance evaluation is shown. In Fig. 6.8 is depicted an example of UAV angular tracking showing the real UAV simulated angular trajectory jointly to PF and BM estimated trajectories The 3A-ULA is positioned in the center of the axis.

Performance with Static and Dynamic σ_s

We now consider the performance as a function of the signal-to-noise-ratio SNR $= |A|^2/\sigma_w^2$. In Fig. 6.9, the AT-RMSE of the azimuthal coordinate ϕ and the inclination coordinate θ for both the PF algorithm and the BM are reported. Furthermore the impact on performance of the PSAS algorithm introduced in Sec. 6.2.5 is analysed. It is possible to observe how, due to the geometrical asymmetry, the performance in terms of AT-RMSE is significantly different between θ and ϕ. Greater SNR values lead to lower AT-RMSE for both PF and BM estimations. It is important to state that for a static value of σ_s, PF performs better than BM in a broad range of SNR values. For example, at $2dB$ of SNR it outperforms the BM algorithm by about 17° for ϕ and 10° for θ. The analysis shows that the introduction of the PSAS algorithm leads to a further improvement of performance. For example, at $2dB$ of SNR the PSAS leads to a performance improvement of 5° for ϕ

and 3° for θ w.r.t. the use of a static σ_s. It is visible in Fig. 6.9 how the introduction of the PF algorithm allows to overcome the AT-CRLB. This is possible thanks to the a priori knowledge of the UAV path extracted by the motion model from the previous steps of the trajectory. For higher SNR the performance improvement of PF with respect to

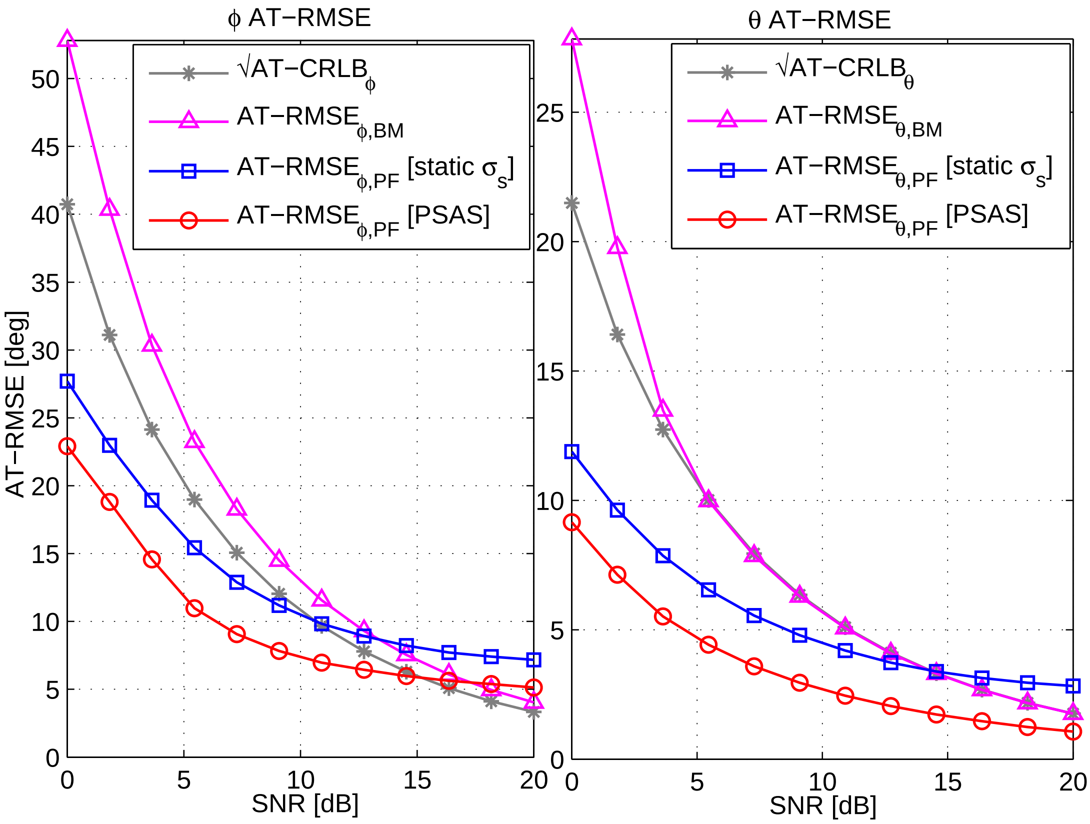

Figure 6.9: AT-RMSE for different SNR_{dB} conditions with dynamic and static σ_s.

the BM algorithm is less prominent than for lower SNR .

Performance for Different Inter-Antenna Distances D_{norm}

Now, the behaviour of the AT-RMSE for the BM and PF algorithms is analysed varying the normalized inter antenna distance D_{norm}. To unambiguously extract the phase from $u_n^{(a)}$ the inter element distance must be less than half of the impinging signal wavelength [101]: $D_{\text{norm}} \leq 0.5$. Furthermore in (6.50) it is visible that for higher values of D_{norm} the CRLBs increase. This leads to $D_{\text{norm}} = 0.5$ as the optimal value for the estimation. However, in lower SNR scenarios and for D_{norm} values near 0.5 the CRLB is found to be overly-optimistic. In fact, high C-AWGN and the other impairments in (6.25) severely impair performance corrupting the value of $\angle u_n^{(x)}$ in (6.27) and making it exceeding 180°. The PF algorithm, thanks to its hypothesised a priori knowledge of the UAV path given by the motion model, attenuates this impairing effect. In Fig. 6.9, we can see that the proposed PF algorithm is less dependent from $D_{\text{norm}} = \frac{Df_0}{c_0}$ than the BM. Thus, the same 3A-ULA is usable for a wider set of carrier frequency f_0 w.r.t. the BM that exhibits its optimal performance for a narrow interval of D_{norm} around 0.4. For this reason, the PF algorithm can offer good performance also in a multiple UAVs scenario where multiplexing is implemented in a frequency division fashion.

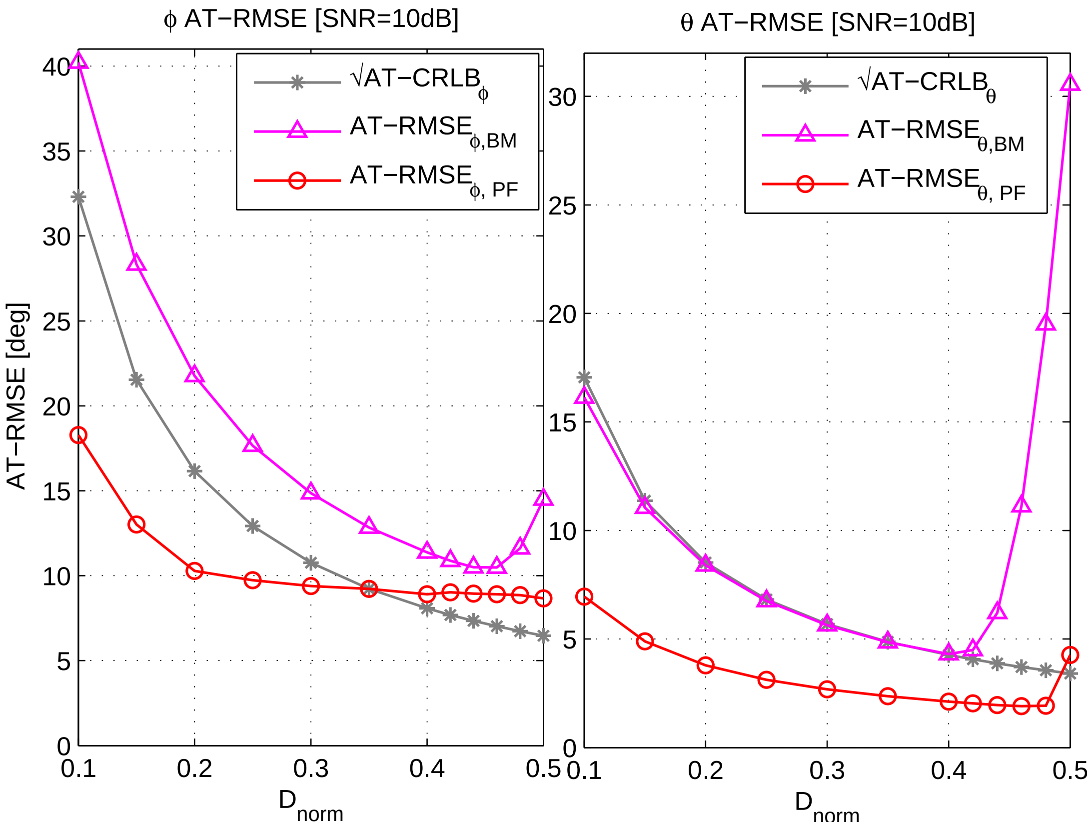

Figure 6.10: AT-RMSE for different normalized 3A-ULA inter-antenna distance $D_{\mathrm{norm}} = D/\lambda_0$.

Conclusions

We have discussed the application of an appropriately designed PF algorithm for self (SL-S) and remote (GL-S) localization of UAVs using a 3A-ULA of antennas, showing an overall increase of performance w.r.t. the baseline BM. A novel algorithm to manage the amplitude of the particle swarm, namely PSAS, has been developed and tested, showing a further increase of precision. A complete, fully adjustable and effective 3D UAVs trajectory emulator, namely CARATE, has been proposed and used to assess performance. Strong impairing effects like Doppler spread, phase offset and phase noise have been considered in the performance evaluation. The effects on the proposed localization algorithm of the PF model parameters as well as the SNR and the 3A-ULA characteristics have been studied. Numerical results show that the proposed PF algorithm is able of dynamically track the UAVs angular position better that the BM. A critical point of this approach is that, similarly to PSAS behaviour, a dynamic calibration procedure has to be implemented to optimize the PF parameters. Future work will also investigate the integration of ranging algorithms like Received Signal Strength Estimation (RSSE) and ToA to PF to provide full 3D localization.

7

Conclusions

This work has been focused on the analysis and the development of AoA radio localization algorithms. The radio positioning systems that have been considered comprise a radio source and a receiving array of antennas.

In Ch. 2 an overview of AoA techniques for radio sources localization has been carried out. In particular, different AoA techniques scenarios have been analysed: AoA collaborative/opportunistic approaches (Sec. 2.2), received signals types (Sec. 2.3), estimation techniques (Sec. 2.4), receiving antenna arrays (Sec. 2.5) and hardware architectures (Sec. 2.6).

In Ch. 3 the effects on received signals statistics of transmitter hardware impairments such as DCO, PO, IQU and IQS have been discussed. The pdfs of the oversampled received signals affected by hardware impairments have been analysed and compared with the ideal counterpart. The hardware impairments of the transmitter have been discovered to generate peculiar statistical effects on received signals. The statistical patterns imposed on the pdfs of received signals by the impaired hardware have been interpreted in Ch. 5 such as hardware fingerprints in AoA discovery.

In Ch. 4 the detrimental consequences of MP on communication systems have been carried out. The US-CIR expression has been discussed as a simplification for real scenarios with continuous CIR expressions. A geometrical interpretation of the positions of the scatterers that produce a determined US-CIR has been carried out in Sec. 4.2. In Sec. 4.2 it has been been verified that the US-CIR is able to represent a real geometric MP scenario. Considering an array of antennas, a method to obtain the CIR for each antenna from a main US-CIR has been developed in Sec. 4.3. A statistical method to generate the array CIRs with a real geometrical meaning has been developed in Sec. 4.4. The effects of the MP on the pdfs of received signals of each sensor have been analysed in Sec. 4.5 providing a graphical fingerprint interpretation.

In Ch. 5 two novel techniques that estimate the AoA exploiting the statistical proprieties of modulated signals impinging on a generic receiving array have been presented. In particular, to estimate the D-PoAs, the pdfs of the received signals have been manipulated to reciprocally overlap their 1D pattern in the CSP-IDO method (Sec. 5.1), and their 2D pattern in the BCID method (Sec. 5.2). The proposed methods are suitable to work with a-simultaneous signal acquisitions from the array sensors, where other methods, such as MUSIC-like algorithms, that acquire signals simultaneously, cannot be applied. The proposed algorithms, applied to a TSA at the receiver, provide a substantial reduction of hardware employment w.r.t. simultaneous approaches. Furthermore, CSP-IDO and BCID are able to improve their performance exploiting the transmitter impaired hardware signature. Since the use of the proposed methods exploits the received signals pdfs, their application is feasible with any type on numerically modulated signal, such as QAM. For this reason CSP-IDO and BCID can also be applied to one or multiple sub-carriers of a multi-carrier modulation system, such as OFDM, to improve the performance. The performance has been evaluated also in scenarios where the estimation process is affected by MP and impaired by hardware at the receiver showing enough robustness. Proposed techniques thanks to their passive/opportunistic approach to AoA localization and thanks to the limited hardware usage are suited to be applied in a eavesdropping scenario with low-end hardware. Part of this work has been published in [33].

In Ch. 6 two possible scenarios of dynamic AoA tracking, where the position of the radio source changes over time, have been discussed, implemented and tested. Dynamic AoA tracking have been implemented using PF algorithms. In Sec. 6.1 the scenario where an electric car position is tracked eavesdropping its V2X signalling with a IEEE802.11p like protocol has been discussed. The electric car tracking has been tested using an experimental test-bed and real measures, compared with the reference estimation provided by a GPS receiver. Part of this work has been published in [93].

In Sec. 6.2 the scenario where the position of an UAV is tracked eavesdropping its communications or radio anchors signals using a 3A-ULA has been considered. The application of an appropriately designed PF algorithm for self (SL-S) and remote (GL-S) localization has been discussed. A novel algorithm to manage the amplitude of the particle swarm, namely PSAS, has been developed and tested, showing a further increase of precision. A complete, fully adjustable and effective 3D UAVs trajectory emulator, namely CARATE, has been proposed and used to assess performance. Part of this work has been published in [6].

Bibliography

[1] R. Zekavat and R. M. Buehrer, *Overview of Global Navigation Satellite Systems.* Wiley-IEEE Press, 2012, pp. 923–974. [Online]. Available: http://ieeexplore.ieee.org/xpl/articleDetails.jsp?arnumber=6047801

[2] ——, *An Introduction to Direction-of-Arrival Estimation Techniques via Antenna Arrays.* Wiley-IEEE Press, 2012, pp. 279–317. [Online]. Available: http://ieeexplore.ieee.org/xpl/articleDetails.jsp?arnumber=6047822

[3] M. Sahmoudi, A. Bourdeau, and J. Y. Tourneret, "Deep fusion of vector tracking GNSS receivers and a 3D city model for robust positioning in urban canyons with NLOS signals," in *2014 7th ESA Workshop on Satellite Navigation Technologies and European Workshop on GNSS Signals and Signal Processing (NAVITEC)*, Dec 2014, pp. 1–7.

[4] J. Foutz, A. Spanias, and M. Banavar, *Narrowband Direction of Arrival Estimation for Antenna Arrays.* Morgan and Claypool, 2008. [Online]. Available: http://ieeexplore.ieee.org/xpl/articleDetails.jsp?arnumber=6813080

[5] P. Q. C. Ly, S. D. Elton, and D. A. Gray, "AOA estimation of two narrowband signals using interferometry," in *Phased Array Systems and Technology (ARRAY), 2010 IEEE International Symposium on*, Oct 2010, pp. 1004–1009.

[6] A. Papaiz and A. M. Tonello, "Azimuth and Elevation Dynamic Tracking of UAVs via 3-Axial ULA and Particle Filtering," *International Journal of Aerospace Engineering*, vol. 2016, may 2016.

[7] N. Iwakiri and T. Kobayashi, "Joint TOA and AOA Estimation of UWB Signal Using Time Domain Smoothing," in *2007 2nd International Symposium on Wireless Pervasive Computing*, Feb 2007.

[8] T. E. Biedka, J. H. Reed, and B. D. Woerner, "Direction finding methods for CDMA systems," in *Signals, Systems and Computers, 1996. Conference Record of the Thirtieth Asilomar Conference on*, vol. 1, Nov 1996, pp. 637–641 vol.1.

[9] L. C. Godara, “Application of antenna arrays to mobile communications. II. Beamforming and direction-of-arrival considerations,” *Proceedings of the IEEE*, vol. 85, no. 8, pp. 1195–1245, Aug 1997.

[10] T. Bui, P. Xu, N. Phan, W. Zhu, and G. Wu, “An accurate and energy-efficient localization algorithm for wireless sensor networks,” in *2016 IEEE 83rd Vehicular Technology Conference (VTC Spring)*, May 2016, pp. 1–5.

[11] M. Z. Win, A. Conti, S. Mazuelas, Y. Shen, W. M. Gifford, D. Dardari, and M. Chiani, “Network localization and navigation via cooperation,” *IEEE Communications Magazine*, vol. 49, no. 5, pp. 56–62, May 2011.

[12] N. Patwari, J. N. Ash, S. Kyperountas, A. O. Hero, R. L. Moses, and N. S. Correal, “Locating the nodes: cooperative localization in wireless sensor networks,” *IEEE Signal Processing Magazine*, vol. 22, no. 4, pp. 54–69, July 2005.

[13] A. Conti, M. Guerra, D. Dardari, N. Decarli, and M. Z. Win, “Network experimentation for cooperative localization,” *IEEE Journal on Selected Areas in Communications*, vol. 30, no. 2, pp. 467–475, February 2012.

[14] R. Niu and P. K. Varshney, “Target location estimation in sensor networks with quantized data,” *IEEE Transactions on Signal Processing*, vol. 54, no. 12, pp. 4519–4528, Dec 2006.

[15] D. Dardari, A. Conti, U. Ferner, A. Giorgetti, and M. Z. Win, “Ranging with ultrawide bandwidth signals in multipath environments,” *Proceedings of the IEEE*, vol. 97, no. 2, pp. 404–426, Feb 2009.

[16] S. Bartoletti, W. Dai, A. Conti, and M. Z. Win, “A mathematical model for wideband ranging,” *IEEE Journal of Selected Topics in Signal Processing*, vol. 9, no. 2, pp. 216–228, March 2015.

[17] Z. Xiao, Y. Hei, Q. Yu, and K. Yi, “A survey on impulse-radio UWB localization,” *Science China Information Sciences*, vol. 53, no. 7, pp. 1322–1335, 2010. [Online]. Available: http://dx.doi.org/10.1007/s11432-010-3102-1

[18] C. Saber, R. Lamberti, and C. Gimenes, *Synchronization Solution for the TDSC-UWB Detection Method*. Dordrecht: Springer Netherlands, 2008, pp. 311–316. [Online]. Available: http://dx.doi.org/10.1007/978-1-4020-8737-0_56

[19] L. Cong and W. Zhuang, “Hybrid TDOA/AOA mobile user location for wideband CDMA cellular systems,” *IEEE Transactions on Wireless Communications*, vol. 1, no. 3, pp. 439–447, Jul 2002.

[20] T. Sanchez, C. Gomez, L. Betancur, A. Garcia, and R. Hincapie, "From theory to practice: Implementations issues for techniques based on aoa and tdoa," in *2016 8th Euro American Conference on Telematics and Information Systems (EATIS)*, April 2016, pp. 1–4.

[21] G. Mao, B. Fidan, and B. D. Anderson, "Wireless sensor network localization techniques," *Computer Networks*, vol. 51, no. 10, pp. 2529 – 2553, 2007.

[22] S. Gezici, Z. Tian, G. B. Giannakis, H. Kobayashi, A. F. Molisch, H. V. Poor, and Z. Sahinoglu, "Localization via ultra-wideband radios: a look at positioning aspects for future sensor networks," *IEEE Signal Processing Magazine*, vol. 22, no. 4, pp. 70–84, July 2005.

[23] J. Liang and D. Liu, "Joint Elevation and Azimuth Direction Finding Using L-Shaped Array," *IEEE Transactions on Antennas and Propagation*, vol. 58, no. 6, pp. 2136–2141, June 2010.

[24] B. Liao, K. M. Tsui, and S. C. Chan, "Frequency invariant uniform concentric circular arrays with directional elements," *IEEE Transactions on Aerospace and Electronic Systems*, vol. 49, no. 2, pp. 871–884, APRIL 2013.

[25] Q. Yuan, Q. Chen, and K. Sawaya, "Accurate DOA estimation using array antenna with arbitrary geometry," *IEEE Transactions on Antennas and Propagation*, vol. 53, no. 4, pp. 1352–1357, April 2005.

[26] S. Xu and K. Doğançay, "Optimal sensor deployment for 3D AOA target localization," in *2015 IEEE International Conference on Acoustics, Speech and Signal Processing (ICASSP)*, April 2015, pp. 2544–2548.

[27] S. C. K. Herath and P. N. Pathirana, "Optimal sensor placement in linear arrays: Part I; AoA based localization," in *2011 Seventh International Conference on Intelligent Sensors, Sensor Networks and Information Processing*, Dec 2011, pp. 277–281.

[28] B. Razavi, *RF Microelectronics*, ser. Prentice Hall Communications Engineering and Emerging Technologies. Prentice Hall, 2012. [Online]. Available: https://books.google.it/books?id=_TccKQEACAAJ

[29] A. Tarighat, R. Bagheri, and A. H. Sayed, "Compensation schemes and performance analysis of IQ imbalances in OFDM receivers," *IEEE Transactions on Signal Processing*, vol. 53, no. 8, pp. 3257–3268, Aug 2005.

[30] B. Razavi, "Design considerations for direct-conversion receivers," *IEEE Transactions on Circuits and Systems II: Analog and Digital Signal Processing*, vol. 44, no. 6, pp. 428–435, Jun 1997.

[31] X. Ken, C. Min, H. Xiaoyong, C. Zhijian, and Z. Weiguo, “An automatic DC-Offset cancellation method and circuit for RF transceivers,” in *2015 IEEE 11th International Conference on ASIC (ASICON)*, Nov 2015, pp. 1–4.

[32] J. Tubbax, B. Come, L. V. der Perre, S. Donnay, M. Engels, M. Moonen, and H. D. Man, “Joint compensation of IQ imbalance and frequency offset in OFDM systems,” in *Radio and Wireless Conference, 2003. RAWCON ’03. Proceedings*, Aug 2003, pp. 39–42.

[33] A. Papaiz and A. M. Tonello, “Single-Receiver switched opportunistic approach to AoA estimation in hardware impaired scenarios,” in *11th International ITG Conference on Systems, Communications and Coding 2017 (SCC’2017)*, Hamburg, Germany, Feb. 2017.

[34] G. Giorgetti, A. Cidronali, S. K. S. Gupta, and G. Manes, “Single-anchor indoor localization using a switched-beam antenna,” *IEEE Communications Letters*, vol. 13, no. 1, pp. 58–60, January 2009.

[35] S. W. Varade and K. D. Kulat, “Robust Algorithms for DOA Estimation and Adaptive Beamforming for Smart Antenna Application,” in *2009 Second International Conference on Emerging Trends in Engineering Technology*, Dec 2009, pp. 1195–1200.

[36] T. B. Lavate, V. K. Kokate, and A. M. Sapkal, “Performance Analysis of MUSIC and ESPRIT DOA Estimation Algorithms for Adaptive Array Smart Antenna in Mobile Communication,” in *Computer and Network Technology (ICCNT), 2010 Second International Conference on*, April 2010, pp. 308–311.

[37] “IEEE Standard for Information technology– Local and metropolitan area networks– Specific requirements– Part 11: Wireless LAN Medium Access Control (MAC) and Physical Layer (PHY) Specifications Amendment 6: Wireless Access in Vehicular Environments,” *IEEE Std 802.11p-2010 (Amendment to IEEE Std 802.11-2007 as amended by IEEE Std 802.11k-2008, IEEE Std 802.11r-2008, IEEE Std 802.11y-2008, IEEE Std 802.11n-2009, and IEEE Std 802.11w-2009)*, pp. 1–51, July 2010.

[38] Y. Morgan, “Notes on DSRC amp; WAVE Standards Suite: Its Architecture, Design, and Characteristics,” *Communications Surveys Tutorials, IEEE*, vol. 12, no. 4, pp. 504–518, Fourth 2010.

[39] Y. Wang, M. Papageorgiou, and A. Messmer, “A real-time freeway network traffic surveillance tool,” *Control Systems Technology, IEEE Transactions on*, vol. 14, no. 1, pp. 18–32, Jan 2006.

[40] J. Lee and A. Bovik, "Estimation and analysis of urban traffic flow," in *Image Processing (ICIP), 2009 16th IEEE International Conference on*, Nov 2009, pp. 1157–1160.

[41] D. Inserra and A. M. Tonello, "Performance analysis of a novel antenna array calibration approach for direction finding systems," *Trans. Emerging Telecommunications Technologies*, vol. 23, no. 8, pp. 777–788, 2012.

[42] W. Xu and M. Kaveh, "Theoretical comparison for biases of MUSIC-like DoA estimators," in *Acoustics, Speech, and Signal Processing, 1995. ICASSP-95., 1995 International Conference on*, vol. 3, May 1995, pp. 1653–1656 vol.3.

[43] M. Arulampalam, S. Maskell, N. Gordon, and T. Clapp, "A tutorial on particle filters for online nonlinear/non-Gaussian Bayesian tracking," *Signal Processing, IEEE Transactions on*, vol. 50, no. 2, pp. 174–188, Feb 2002.

[44] S. Maskell and N. Gordon, "A tutorial on particle filters for on-line nonlinear/non-Gaussian Bayesian tracking," in *Target Tracking: Algorithms and Applications (Ref. No. 2001/174), IEE*, vol. Workshop, Oct 2001, pp. 2/1–2/15 vol.2.

[45] P. Quater, F. Grimaccia, S. Leva, M. Mussetta, and M. Aghaei, "Light Unmanned Aerial Vehicles (UAVs) for Cooperative Inspection of PV Plants," *Photovoltaics, IEEE Journal of*, vol. 4, no. 4, pp. 1107–1113, July 2014.

[46] M. Haque, M. Muhammad, D. Swarnaker, and M. Arifuzzaman, "Autonomous quadcopter for product home delivery," in *Electrical Engineering and Information Communication Technology (ICEEICT), 2014 International Conference on*, April 2014, pp. 1–5.

[47] (2015, february) FAA unveils drone rules: Autonomy is in, drone delivery is out. IEEE Spectrum. [Online]. Available: http://spectrum.ieee.org/automaton/robotics/drones/faa-proposed-commercial-drone-rules/

[48] M. Peacock and M. N. Johnstone, "Towards detection and control of civilian unmanned aerial vehicles," in *Australian Information Warfare Conference, 2013. WCICA 2013.* SRI Security Research Institute, Edith Cowan University, Perth, Western Australia, 2013.

[49] S. Panzieri, F. Pascucci, and G. Ulivi, "An outdoor navigation system using GPS and inertial platform," *IEEE/ASME Transactions on Mechatronics*, vol. 7, no. 2, pp. 134–142, Jun 2002.

[50] J. s. Lim, J. Song, and K. M. Sung, "Forward-backward time varying forgetting factor Kalman filter based DOA estimation algorithm for UAV (Unmanned Aerial

Vehicle) autolanding," in *2002 IEEE International Conference on Acoustics, Speech, and Signal Processing*, vol. 4, May 2002, pp. IV–3964–IV–3967.

[51] M. Rzymowski, D. Duraj, L. Kulas, K. Nyka, and P. Woznica, "UHF ESPAR antenna for simple Angle of Arrival estimation in UHF RFID applications," in *2016 21st International Conference on Microwave, Radar and Wireless Communications (MIKON)*, May 2016, pp. 1–4.

[52] K. VonEhr, S. Hilaski, B. E. Dunne, and J. Ward, "Software Defined Radio for direction-finding in UAV wildlife tracking," in *2016 IEEE International Conference on Electro Information Technology (EIT)*, May 2016, pp. 0464–0469.

[53] Y. Shen, S. Mazuelas, and M. Z. Win, "Network navigation: Theory and interpretation," *IEEE Journal on Selected Areas in Communications*, vol. 30, no. 9, pp. 1823–1834, October 2012.

[54] A. Zanellaza, "Best practice in RSS measurements and ranging," *IEEE Communications Surveys Tutorials*, vol. 18, no. 4, pp. 2662–2686, Fourthquarter 2016.

[55] Y. Wang and K. C. Ho, "An Asymptotically Efficient Estimator in Closed-Form for 3-D AOA Localization Using a Sensor Network," *IEEE Transactions on Wireless Communications*, vol. 14, no. 12, pp. 6524–6535, Dec 2015.

[56] Y. Han, H. Meng, Y. Shen, and Y. Liu, "Fundamental localization accuracy in narrowband array-based systems," in *2014 IEEE International Conference on Acoustics, Speech and Signal Processing (ICASSP)*, May 2014, pp. 4668–4672.

[57] Y. Shen and M. Z. Win, "Fundamental Limits of Wideband Localization, Part I: A General Framework," *IEEE Transactions on Information Theory*, vol. 56, no. 10, pp. 4956–4980, Oct 2010.

[58] Y. Shen, H. Wymeersch, and M. Z. Win, "Fundamental Limits of Wideband Localization, Part II: Cooperative Networks," *IEEE Transactions on Information Theory*, vol. 56, no. 10, pp. 4981–5000, Oct 2010.

[59] D. Inserra and A. M. Tonello, "Training symbol exploitation in CP-OFDM for DoA estimation in multipath channels," in *21st European Signal Processing Conference (EUSIPCO 2013)*, Sept 2013, pp. 1–5.

[60] J. Li, B. Halder, P. Stoica, and M. Viberg, "Computationally efficient angle estimation for signals with known waveforms," *IEEE Transactions on Signal Processing*, vol. 43, no. 9, pp. 2154–2163, Sep 1995.

[61] G. Han, J. Jiang, C. Zhang, T. Q. Duong, M. Guizani, and G. K. Karagiannidis, "A survey on mobile anchor node assisted localization in wireless sensor networks," *IEEE Communications Surveys Tutorials*, vol. 18, no. 3, pp. 2220–2243, thirdquarter 2016.

[62] P. Deng and P. Z. Fan, "An AOA assisted TOA positioning system," in *WCC 2000 - ICCT 2000. 2000 International Conference on Communication Technology Proceedings (Cat. No.00EX420)*, vol. 2, 2000, pp. 1501–1504 vol.2.

[63] S. Bartoletti, A. Giorgetti, M. Z. Win, and A. Conti, "Blind selection of representative observations for sensor radar networks," *IEEE Transactions on Vehicular Technology*, vol. 64, no. 4, pp. 1388–1400, April 2015.

[64] S. Sesia, I. Toufik, and M. Baker, *LTE - The UMTS Long Term Evolution: From Theory to Practice.* Wiley, 2011.

[65] M. M. Hyder and K. Mahata, "Zadoff-Chu sequence design for random access initial uplink synchronization in LTE-like systems," *IEEE Transactions on Wireless Communications*, vol. PP, no. 99, pp. 1–1, 2016.

[66] B. Walke, P. Seidenberg, and M. Althoff, *UMTS: The Fundamentals.* Wiley, 2003. [Online]. Available: https://books.google.it/books?id=KRlUvPWeTYQC

[67] C.-T. Chiang and A. C. Chang, "DOA estimation in the asynchronous DS-CDMA system," *IEEE Transactions on Antennas and Propagation*, vol. 51, no. 1, pp. 40–47, Jan 2003.

[68] H. Fu and P. Y. Kam, "Symbol sequence detection with joint channel estimation and carrier synchronization," in *2016 IEEE International Conference on Communications (ICC)*, May 2016, pp. 1–5.

[69] P. Stuckmann, *The GSM Evolution: Mobile Packet Data Services.* Wiley, 2003. [Online]. Available: https://books.google.it/books?id=bQKOse85OHkC

[70] S. Tomic, M. Beko, and R. Dinis, "3-D Target Localization in Wireless Sensor Network Using RSS and AoA Measurements," *IEEE Transactions on Vehicular Technology*, vol. PP, no. 99, pp. 1–1, 2016.

[71] L. Stoica, A. Rabbachin, and I. Oppermann, "A low-complexity noncoherent IR-UWB transceiver architecture with TOA estimation," *IEEE Transactions on Microwave Theory and Techniques*, vol. 54, no. 4, pp. 1637–1646, June 2006.

[72] G. Bekefi and A. Barrett, *Electromagnetic Vibrations, Waves, and Radiation.* MIT Press, 1977. [Online]. Available: https://books.google.it/books?id=zRfTq6iMdNEC

[73] D. Inserra and A. M. Tonello, “Characterization of Hardware Impairments in Multiple Antenna Systems for DoA Estimation,” *J. Electrical and Computer Engineering*, 2011.

[74] A. Tonello and D. Inserra, “Radio positioning based on DoA estimation: An implementation perspective,” in *Communications Workshops (ICC), 2013 IEEE International Conference on*, June 2013, pp. 27–31.

[75] J. Harris and H. Stocker, *Handbook of Mathematics and Computational Science*, ser. Environmental Intelligence Unit. Springer New York, 1998.

[76] B. Razavi, “Design considerations for direct-conversion receivers,” *IEEE Transactions on Circuits and Systems II: Analog and Digital Signal Processing*, vol. 44, no. 6, pp. 428–435, Jun 1997.

[77] A. A. Abidi, “Direct-conversion radio transceivers for digital communications,” *IEEE Journal of Solid-State Circuits*, vol. 30, no. 12, pp. 1399–1410, Dec 1995.

[78] W. T. Webb and R. Steele, “Variable rate qam for mobile radio,” *IEEE Transactions on Communications*, vol. 43, no. 7, pp. 2223–2230, Jul 1995.

[79] C. Thomas, M. Weidner, and S. Durrani, “Digital Amplitude-Phase Keying with M-Ary Alphabets,” *IEEE Transactions on Communications*, vol. 22, no. 2, pp. 168–180, Feb 1974.

[80] P. Kenington, *RF and Baseband Techniques for Software Defined Radio*, ser. Artech House mobile communications series. Artech House, 2005. [Online]. Available: https://books.google.it/books?id=nfFSAAAAMAAJ

[81] B. Lindoff and P. Malm, “BER performance analysis of a direct conversion receiver,” *IEEE Transactions on Communications*, vol. 50, no. 5, pp. 856–865, May 2002.

[82] D. Tse and P. Viswanath, *Fundamentals of Wireless Communication*, ser. Wiley series in telecommunications. Cambridge University Press, 2005. [Online]. Available: https://books.google.it/books?id=66XBb5tZX6EC

[83] P. Shankar, *Fading and Shadowing in Wireless Systems*, ser. SpringerLink : Bücher. Springer New York, 2011. [Online]. Available: https://books.google.it/books?id=WduXAQLomAoC

[84] A. Molisch, *Wireless Communications*, ser. Wiley - IEEE. Wiley, 2012. [Online]. Available: https://books.google.it/books?id=877tFGeQo5oC

[85] J. Fuhl, A. F. Molisch, and E. Bonek, “Unified channel model for mobile radio systems with smart antennas,” *IEEE Proceedings - Radar, Sonar and Navigation*, vol. 145, no. 1, pp. 32–41, Feb 1998.

[86] R. B. Ertel and J. H. Reed, “Angle and time of arrival statistics for circular and elliptical scattering models,” *IEEE Journal on Selected Areas in Communications*, vol. 17, no. 11, pp. 1829–1840, Nov 1999.

[87] P. Petrus, J. H. Reed, and T. S. Rappaport, “Geometrical-based statistical macrocell channel model for mobile environments,” *IEEE Transactions on Communications*, vol. 50, no. 3, pp. 495–502, Mar 2002.

[88] N. M. Khan, M. T. Simsim, and P. B. Rapajic, “A Generalized Model for the Spatial Characteristics of the Cellular Mobile Channel,” *IEEE Transactions on Vehicular Technology*, vol. 57, no. 1, pp. 22–37, Jan 2008.

[89] V. Erceg, L. J. Greenstein, S. Y. Tjandra, S. R. Parkoff, A. Gupta, B. Kulic, A. A. Julius, and R. Bianchi, “An empirically based path loss model for wireless channels in suburban environments,” *IEEE Journal on Selected Areas in Communications*, vol. 17, no. 7, pp. 1205–1211, Jul 1999.

[90] R. H. Clarke, “A statistical theory of mobile-radio reception,” *The Bell System Technical Journal*, vol. 47, no. 6, pp. 957–1000, July 1968.

[91] J. Proakis, *Digital Communications*, ser. Electrical engineering series. McGraw-Hill, 2001. [Online]. Available: https://books.google.it/books?id=sbr8QwAACAAJ

[92] S. Appadwedula and C. M. Keller, “Direction-Finding Results for a Vector Sensor Antenna on a Small UAV,” in *Fourth IEEE Workshop on Sensor Array and Multichannel Processing, 2006.*, July 2006, pp. 74–78.

[93] A. Papaiz and A. M. Tonello, “Particle filtering with weight reshaping for opportunistic angle of arrival estimation in a vehicular scenario,” in *2015 IEEE ICCE-Berlin*, Berlin, Germany, Sep. 2015, pp. 145–149.

[94] S. F. Chuang, W. R. Wu, and Y. T. Liu, “High-Resolution AoA Estimation for Hybrid Antenna Arrays,” *IEEE Transactions on Antennas and Propagation*, vol. 63, no. 7, pp. 2955–2968, July 2015.

[95] IEEE, “802.11 Standard: Wireless LAN Medium Access Control and Physical Layer Specification,” 2007.

[96] Y. Liu, B. Wang, W. He, J. Zhao, and Z. Ding, “Fundamental principles and applications of particle filters,” in *Intelligent Control and Automation, 2006. WCICA 2006. The Sixth World Congress on*, vol. 2, 2006, pp. 5327–5331.

[97] D. Inserra and A. M. Tonello, “A multiple antenna wireless testbed for the validation of DoA estimation algorithms,” *{AEU} - International Journal of Electronics and Communications*, vol. 68, no. 1, pp. 10 – 18, 2014.

[98] K. Dogancay, "UAV Path Planning for Passive Emitter Localization," *Aerospace and Electronic Systems, IEEE Transactions on*, vol. 48, no. 2, pp. 1150–1166, APRIL 2012.

[99] S. Kay, *Fundamentals of Statistical Signal Processing: Estimation Theory.* Prentice Hall, 1993.

[100] D. Inserra and A. M. Tonello, "DoA Estimation with Compensation of Hardware Impairments," in *Vehicular Technology Conference Fall (VTC 2010-Fall), 2010 IEEE 72nd*, Sept 2010, pp. 1–5.

[101] Z. M. Liu and F. C. Guo, "Azimuth and elevation estimation with rotating long-baseline interferometers," *IEEE Transactions on Signal Processing*, vol. 63, no. 9, pp. 2405–2419, May 2015.